

Budker Institute of Nuclear Physics
Siberian Branch Russian Academy of Sciences
(BINP SB RAS)

Super Charm – Tau Factory

CONCEPTUAL DESIGN REPORT
PART ONE
(physics program, detector)

[very preliminary draft]

Novosibirsk – 2018

This document is focused on a project of the Super Charm – Tau factory in the Budker Institute of Nuclear Physics (Novosibirsk, Russia). An electron-positron collider will operate in the range of center-of-mass energies from 2 to 5 GeV with unprecedented peak luminosity of about $10^{35} \text{ cm}^{-2}\text{s}^{-1}$ and longitudinally polarized electrons at interaction point.

V.V. Anashin, A.V. Anisenkov, V.M. Aulchenko, E.M. Baldin, A.K. Barladyan, A.Yu. Barnyakov, I.Yu. Basok, E.A. Bekhtenev, O.L. Beloborodova, D.E. Berkaev, A.E. Blinov, V.E. Blinov, A.V. Bobrov, V.S. Bobrovnikov, A.G. Bogdanchikov, A.V. Bogomyagkov, A.E. Bondar, A.A. Borodenko, A.V. Bragin, A.R. Buzykaev, V.L. Chernyak, V.Ya. Chudaev, I.N. Churkin, N.S. Dikansky, T.V. Dimova, A.M. Dolgov, V.P. Druzhinin, F.A. Emanov, S.I. Eidelman, Yu.I. Eidelman, D.A. Epifanov, L.B. Epshteyn, E.S. Ershov, V.S. Fadin, N.I. Gabyshev, A.Yu. Garmash, S.A. Glukhov, V.B. Golubev, D.N. Grigoriev, V.R. Groshev, G.I. Gusev, S.E. Karnaev, G.V. Karpov, S.V. Karpov, P.V. Kasyanenko, V.F. Kazanin, E.K. Kengebulatov, **B.I. Khazin**, S.V. Khrushchev, V.A. Kiselev, V.I. Kokoulin, V.V. Kolmogorov, S.A. Kononov, I.A. Koop, A.A. Korol, E.A. Kravchenko, A.A. Krasnov, P.P. Krokovny, V.N. Kudryavtsev, A.S. Kuzmin, V.S. Kuzminykh, V.F. Kulikov, G.N. Kulipanov, E.A. Kuper, G.Ya. Kurkin, A.E. Levichev, E.B. Levichev, R.N. Li, P.V. Logachev, P.V. Martyshkin, D.V. Matvienko, A.S. Medvedko, O.I. Meshkov, N.A. Mezentsev, A.I. Milstein, A.A. Morozov, N.Yu. Muchnoi, S.A. Nikitin, I.B. Nikolaev, I.N. Okunev, A.P. Onuchin, S.B. Oreshkin, A.A. Osipov, A.S. Osipov, A.V. Otboev, A.V. Petrenko, M.V. Petrichenkov, V.M. Petrov, V.V. Petrov, P.A. Piminov, A.O. Poluektov, A.V. Polyanski, V.G. Prisekin, Yu.A. Pupkov, V.A. Rodiakin, G.A. Savinov, Yu.M. Schatunov, S.I. Serednyakov, D.N. Shatilov, V.E. Shebalin, L.I. Shekhtman, S.V. Shiyankov, V.A. Shkaruba, S.N. Shmakov, D.A. Shtol, A.I. Shusharo, B.A. Shwartz, I.V. Sidorov, S.V. Sinyatkin, K.Yu. Skovpen, A.N. Skrinsky, V.V. Smaluk, A.V. Sokolov, E.V. Starostina, A.M. Sukharev, A.A. Talyshev, V.I. Telnov, Yu.A. Tikhonov, V.M. Titov, A.G. Tribendis, Yu.V. Usov, A.N. Vinokurova, P.D. Vobly, G.V. Vodnev, A.I. Vorobiov, V.S. Vorobiev, Yu.V. Yudin, A.N. Yushkov, A.S. Zaytsev, V.N. Zhilich, V.V. Zhulanov, A.N. Zhuravlev, K.V. Zolotarev

Budker Institute of Nuclear Physics, *pr. Lavrentieva 11, Novosibirsk 630090, Russia*

A.F. Danilyuk

Boreskov Institute of Catalysis, *pr. Lavrentieva 5, Novosibirsk 630090, Russia*

N.N. Achasov, I.F. Ginzburg, G.N. Shestakov

Sobolev Institute of Mathematic, *av. Acad. Koptyug 4, Novosibirsk 630090, Russia*

A.G. Kharlamov, G.L. Kotkin, I.B. Logashenko, D.A. Maksimov, O.I. Meshkov, I.O. Orlov, V.G. Serbo, Yu.I. Skovpen

Novosibirsk State University, *st. Pirogova 2, Novosibirsk 630090, Russia*

M.Yu. Barnyakov, S.G. Pivovarov

Novosibirsk State Technical University, *pr. K.Marksa 20, Novosibirsk 630090, Russia*

A.V. Arefiev, T.A. Aushev, K.A. Chilikin, R.N. Chistov, M.V. Danilov, D.R. Liventsev, R.V. Mizuk, G.V. Pakhlova, P.N. Pakhlov, V.Yu. Rusinov, E.I. Solovyeva, E.I. Tarkovsky, I.N. Tikhomirov, T.V. Uglov

State Scientific Center of the Russian Federation – Institute for Theoretical and Experimental Physics, *st. Bolshaya Cheremushkinskaya 25, Moscow 117218, Russia*

I.R. Boyko, D.V. Dedovich, Yu.A. Nefedov, A.S. Zhemchugov

Joint Institute for Nuclear Research, *st. Joliot-Curie 6, Dubna, Moscow region 141980, Russia*

V.A. Chtchegelsky, V.L. Golovtsov, N.V. Gruzinsky, V.I. Iatsura, V.A. Nikonov, A.V. Sarantsev,
L.N. Uvarov
Petersburg Nuclear Physics Institute, Gatchina, Leningrad district 188300, Russia

A.Yu. Loginov, V.N. Stibunov
Tomsk Polytechnic National Research University of Resource-Efficient Technology,
av. Lenin 30, Tomsk 634050, Russia

D.A. Finogeev, T.L. Karavicheva, E.V. Karpechev, A.B. Kurepin, A.N. Kurepin, V.I. Razin,
A.I. Reshetin, N.S. Topilskaya, E.A. Usenko
Institute for Nuclear Research, pr. 60th October Anniversary prospect 70, Moscow 117312,
Russia

V. Smakhtin
Weizmann Institute of Science, PO Box 26, Rehovot 76100, Israel

M. Bracko, S. Korpar
University of Maribor, Smetanova 17, SI-2000 Maribor, Slovenia

B. Golob, R. Pestotnik, M. Staric
Jozef Stefan Institute, P.O.B. 3000, SI-1001, Ljubljana, Slovenia

P. Krizan
University of Ljubljana, Jadranska 19, SI-1000, Ljubljana, Slovenia

D. Babusci, G. Venanzoni, M. Zobov
Lab. Nazionali di Frascati dell'INFN, CP 13, via E. Fermi 40, I-00044, Frascati Roma,
Italy

A. Lusiani
Scuola Normale Superiore e INFN, Piazza dei Cavalieri 7, I-56126, Pisa, Italy

M. Mascolo, D. Moricciani
University of Rome Tor Vergata, via della Ricerca Scientifica, 1, I-00133, Roma, Italy

H. Czyż
Institute of Physics, University of Silesia in Katowice, Uniwersytecka 4, PL-40-007
Katowice, Poland

F. Jegerlehner
A.Humboldt University, DESY, Platanenallee 6, D-15738, Zeuthen, Germany

Contents

Introduction	7
1 Physics	10
1.1 Introduction	10
1.2 Charmonium	11
1.2.1 Charmonium states below the $D\bar{D}$ threshold	11
1.2.2 Study of exotic charmonium-like states	14
1.3 Spectroscopy of states of light quarks	16
1.4 Physics of D -mesons	18
1.4.1 Spectroscopy of D mesons	18
1.4.2 Charmed-meson decays	21
1.4.3 $D^0-\bar{D}^0$ Mixing	23
1.4.4 Search for CP violation	25
1.4.5 D and D_s meson rare decays	29
1.5 Charmed baryons	31
1.6 τ lepton physics	34
1.7 Measurement of $e^+e^- \rightarrow$ hadrons below 5 GeV	36
1.8 Two-photon physics	39
1.9 Conclusions	40
2 Detector	50
2.1 Overview	50
2.2 Vacuum chamber	51
2.3 Vertex detector	51
2.3.1 Time projection chamber	51
2.4 Drift chamber	55
2.4.1 Introduction	55
2.4.2 Drift chamber design	55
2.4.3 Drift cells	56
2.5 FARICH system	60
2.5.1 Introduction	60
2.5.2 FARICH concept	62
2.5.3 Design	62
2.5.4 MC performance	64
2.5.5 First FARICH prototype tests	66
2.6 Electromagnetic calorimeter	66
2.6.1 Calorimeter elements	69
2.6.2 Photodetectors	70

2.6.3	Calorimeter electronics	74
2.6.4	Pure CsI radiation resistance	74
2.6.5	Measurements with calorimeter prototype	77
2.6.6	Summary	80
2.7	Muon system	80
2.8	Superconducting solenoid	81
2.8.1	Main requirements	81
2.8.2	Original approach	81
2.8.3	Cryogenics	83
2.9	Trigger	83
2.10	Electronics	86
2.10.1	FrontEnd electronics	88
2.10.2	Readout processor	90
2.10.3	Drift chamber electronics	91
2.11	Networking and computing systems	91
2.11.1	Introduction	91
2.11.2	Requirements to the computing infrastructure	92
2.11.3	Brief Overview of TDAQ and Offline Data Processing Systems	92
2.11.4	Architecture of the Data Processing and Storage Systems	93
2.11.5	Roadmap for Building the Offline Computing and Storage Systems	105

Introduction

Several laboratories engaged in the research on high-energy physics discussed projects of $c\tau$ factories in the nineties of the last century. Those installations were planned for a beam energy of $1 \div 3$ GeV and a peak luminosity of about $10^{33} \text{ cm}^{-2}\text{s}^{-1}$ [1, 2, 3, 4, 5, 6, 7]. In connection with study of narrow resonances, various options of monochromatization of the particle collision energy were considered, as well as the possibility of obtaining transversely polarized particles (for accurate energy calibration). The only implemented project from the “family” of the $c\tau$ factories of the 90s is the BEPC-II collider, which was commissioned at the IHEP laboratory in Beijing in 2009 [8]. BEPC-II reached the projected peak luminosity of $1 \cdot 10^{33} \text{ cm}^{-2}\text{s}^{-1}$ at a beam energy of 1.89 GeV in 2016.

The revival of interest in the subject under consideration and commencement of work on the project of the Super Charm–Tau factory at Budker INP SB RAS is due to, first, the outstanding results that were obtained at B-factories at the laboratories of KEK (Japan) and SLAC (USA). These works culminated in the awarding of the 2008 Nobel Prize in Physics to Y. Nambu, M. Kobayashi, and T. Maskawa. Although the high luminosity of the B-factories and the initial radiation state method (proposed and developed at BINP) yielded interesting results in the low-energy region, the creation of a collider factory specialized on studying the physics of charmed particles and tau lepton is still an extremely topical issue.

Secondly, the growing interest in creating a next-generation Super Charm–Tau factory was caused by the appearance of a fundamentally new scheme of beam collision in electron-positron colliders. This scheme (*Crab Waist*, CW) allows raising the luminosity by one or two orders of magnitude without significant increase in the intensity of the beams or the dimensions of the installation or decrease in the bunch length. The idea was offered by the Italian physicist Pantaleo Raimondi in 2006 in connection with the study of the possibility of creating a B-factory with high luminosity [9]. Later, the method was rigorously substantiated in the joint works by P. Raimondi, M. Zobov (INFN LNF, Frascati), and D. Shatilov (BINP, Novosibirsk) [10, 11]. Since 2008, the CW scheme has been successfully applied at the Φ -factory DAΦNE (INFN LNF, Frascati); the results of the experiments show the method to be promising and are in good agreement with the theory [12, 13]. In addition to the Super Charm–Tau factory in Novosibirsk, the projects of the e^+e^- colliders for ultra-high energy FCC-ee (CERN) and CEPC (IHEP, China) are also based on the new approach.

Based on the tasks discussed in detail in the section devoted to the physical program of the Super Charm–Tau factory, the following basic requirements to the accelerator complex were formulated.

- The beam energy must vary from 1 GeV to 2.5 GeV, which will enable conduction of experiments from the threshold of production of nucleons and antinucleons to the region of the family of ψ mesons and charmed baryons. In addition, due to such a wide energy range it will be possible to use the results obtained on the VEPP-2000 and VEPP-4 colliders at BINP.
- The luminosity of the factory must be not less than $10^{35} \text{ cm}^{-2}\text{s}^{-1}$ in the high-energy region

and not less than $10^{34} \text{ cm}^{-2} \text{ s}^{-1}$ in the low-energy region.

- The electron beam must be longitudinally polarized at the interaction point [14, 15].
- No asymmetry of the energies of the colliding beams is required.
- The known methods of monochromatization of the beam collision energy reduce the luminosity, and thus it was decided to abandon monochromatization. The high luminosity in the CW collision scheme makes it possible to effectively study narrow resonance states without monochromatization.
- The energy calibration will be carried out using the reverse Compton scattering of laser radiation on the particles of the circulating beam. This technique was implemented in recent years at VEPP-4M [16] and demonstrated a relative measurement accuracy of better than 10^{-4} , which seems sufficient for the objectives of the new Super Charm–Tau factory. Transversely polarized beams are not required.

So, the main features of the new electron-positron collider in Novosibirsk, that make it a unique world-class facility are the wide range of energies, high luminosity, and the possibility of conducting experiments with a longitudinally polarized electron beam.

In addition to experiments on particle physics and fundamental interactions, the creation of such an advanced facility will result in substantial progress in technologies for application of charged particle beams (including high-field superconducting magnetic systems, high-power and efficient RF generators, precision beam diagnostic devices, control systems, data collection and processing, etc.). These technologies can be successfully used for development and creation of particle accelerators for applied tasks, including sources of synchrotron radiation, installations for therapy of cancer with proton and ion beams, and other types of accelerators for industrial and medical applications.

Bibliography

- [1] A. N. Skrinsky, “Studies for a Tau-Charm Factory”, SLAC-Report-451, October, 1994.
- [2] “C-Tau in Novosibirsk: Conceptual Design Report”, BINP, Novosibirsk, 1995.
- [3] E. Perelshtein et al, Proc. of the 3rd Workshop on the TC Factory, Marbella, Spain, 1-6 Jun 1993, 557-570.
- [4] M. V. Danilov et al, Int. J. Mod. Phys. A, Proc. Suppl. 2A (1993) 455-457.
- [5] E. Berger et al, ANL-HEP-TR-94-12, Feb 1994.
- [6] Yu. Aleksahin, A. Dubrovin, A. Zholents, in EPAC-90 Proc., vol. 1, 398-400.
- [7] He-Sheng Chen, Nucl. Phys. Proc. Suppl. 59: 316-323, 1997.
- [8] J. Q. Wang, L. Ma, Q. Qin, C. Zhang, “Status and performance of BEPC II”, Proceedings of IPAC-10, Kyoto, Japan, 2010, WEXMH01, p. 2359.
- [9] P. Raimondi, “Status of the SuperB Effort”, presentation at the 2nd Workshop on SuperB Factory, LNF-INFN, Frascati, March 2006.
- [10] P. Raimondi, D. Shatilov, M. Zobov, “Beam-Beam Issues for Colliding Schemes with Large Piwinski Angle and Crabbed Waist”, LNF-07-003-IR, 2007, e-Print: physics/0702033.
- [11] P. Raimondi, D. Shatilov, M. Zobov, “Suppression of beam-beam resonances in Crab Waist collisions”, EPAC08-WEPP045, Proc. of EPAC-2008, Genoa, Italy, 23–27 June 2008.
- [12] M. Zobov for DAFNE Collaboration Team, “DAFNE Operation Experience with Crab Waist Collision”, arXiv:0810.2211v1.
- [13] M. Zobov et al., “Test of crab-waist collisions at DAFNE Phi factory”, Phys.Rev.Lett.104:174801, 2010.
- [14] Ya. S. Derbenev, A. M. Kondratenko, A. N. Skrinsky, “On the spin motion of particles in storage rings with arbitrary field”, BINP preprint 2-70, 1970.
- [15] Ya. S. Derbenev, A. M. Kondratenko, A. N. Skrinsky, Soviet Doklady (Physics) vol. 192, 6, pp. 1255-1258, 1970 (in Russian). Soviet Physics “Doklady”, 15, pp 583-586, 1970 (translation).
- [16] V. E. Blinov et al., “Beam energy and energy spread measurement by Compton backscattering of laser radiation at the VEPP-4M collider”, ICFA Beam Dyn. Newslett., vol. 48, pp. 195–207, 2009.

Chapter 1

Physics

1.1 Introduction

A Super Charm–Tau factory (SCTF) is an electron-positron collider operating in the range of center-of-mass (c.m.) energies from 2 to $5 \div 6$ GeV with a high luminosity of about $10^{35} \text{ cm}^{-2}\text{c}^{-1}$. In this energy range practically all states with charm can be produced including charmonium mesons, bound states of c and \bar{c} quarks, charmed mesons and baryons comprising one c (\bar{c}) quark. In addition, at the c.m. energy above $2m_\tau \approx 3.6$ GeV τ -lepton pairs can be produced. Because of its extremely high luminosity such a collider will be a copious source of charmed particles and τ leptons.

The main goal of experiments at SCTF is a study of the processes with c quarks or τ leptons in the final state using data samples that are at least two orders of magnitude higher than those collected in the CLEOc and BESIII experiments. In Table 1.1 we show a list of energies, at which most of SCTF factory data will be collected, and a possible distribution of an integrated luminosity of 1 ab^{-1} over these energies. At SCTF with a luminosity of $10^{35} \text{ cm}^{-2}\text{c}^{-1}$ such an integrated luminosity can be collected during half a year (10^7 s). The luminosities listed in Table 1.1 correspond to approximately 10^9 τ leptons, 10^9 D mesons and a fantastic number (10^{12}) of J/ψ mesons. The total integrated luminosity planned to be collected at the SCTF factory is 10 ab^{-1} . These data samples will allow a systematic study of all states of quarks of the two first generations (u , d , s and c) as well as searches for states of exotic nature.

A theory of strong interactions, quantum chromodynamics (QCD), in addition to standard mesons and baryons consisting of two and three quarks, respectively, cannot rule out the existence of four- and five-quark states as well as bound states of gluons, carriers of strong interactions [1]. Some of the four- and five-quark states have already been observed but we are very far from understanding their properties. Such states are possible because gluons, in contrast to a photon, an electrically neutral carrier of electromagnetic interactions, possess a strong or color charge. QCD predicts both hybrid quark-gluon states and states consisting of gluons only, glueballs. Hybrids and glueballs are a completely new form of matter that can be formed by strong interactions only. One of the tasks of SCTF is to discover exotic states and study their properties.

Huge data samples of D mesons, charmed baryons and τ leptons will allow a search for principally new phenomena, such as CP violation in the D meson system and in τ leptons as well as lepton flavor violation with high sensitivity.

A physics program for SCTF can be subdivided into the following subsections, which are discussed in more detail below:

1. charmonium,

Table 1.1. Energies, at which most of Super Charm–Tau factory data will be collected, and approximate distribution of an integrated luminosity collected during one experimental run (10^7 s, 1 ab^{-1}) over these energies.

E , GeV	L , fb^{-1}		
3.097	300	J/ψ	Light meson spectroscopy, rare decays
3.554	50	$e^+e^- \rightarrow \tau^+\tau^-$ threshold	Precision measurements of τ decays
3.686	150	$\psi(2S)$	Light meson spectroscopy, Charmonium spectroscopy
3.770	300	$\psi(3770)$	D -meson study
4.170	100	$\psi(4160)$	D_s -meson study
4.650	100	maximum of $\sigma(e^+e^- \rightarrow \Lambda_c^+\Lambda_c^-)$	Λ_c study

2. spectroscopy of states of light quarks,
3. physics of D mesons,
4. physics of charmed baryons,
5. τ lepton physics,
6. measurement of the cross section of $e^+e^- \rightarrow$ hadrons,
7. two-photon physics.

1.2 Charmonium

A scheme of charmonium levels is shown in Fig. 1.1. All states lying below the threshold of D meson production and therefore decaying into hadrons consisting of the light u , d and s quarks (or into a lower mass charmonium) have been discovered. Vector mesons ($J^{PC} = 1^{--}$), i.e., J/ψ , $\psi(2S)$, $\psi(3770)$, etc. are directly produced in e^+e^- collisions. In Table 1.2 we list the numbers of 1^{--} mesons that can be produced at SCTF during one experimental season.

1.2.1 Charmonium states below the $D\bar{D}$ threshold

About 10^{12} J/ψ and 10^{11} $\psi(2S)$ can be produced during one experimental season. In radiative decays of J/ψ and $\psi(2S)$ mesons [2] about 10^{10} χ_{cJ} and η_c mesons each can be obtained. About 10^8 h_c mesons can be produced in the $\psi(2S) \rightarrow h_c\pi^0$ decay, which has a branching fraction of $(8.6 \pm 1.3) \times 10^{-4}$ [2]. For observing $\eta_c(2S)$ one can use a rare, radiative transition $\psi(2S) \rightarrow \eta_c(2S)\gamma$ with a branching fraction of $(7 \pm 5) \times 10^{-4}$ [2] or two-photon production (see Sec. 1.8). Such a data sample allows a systematic study of $c\bar{c}$ -meson properties. The following items should be mentioned:

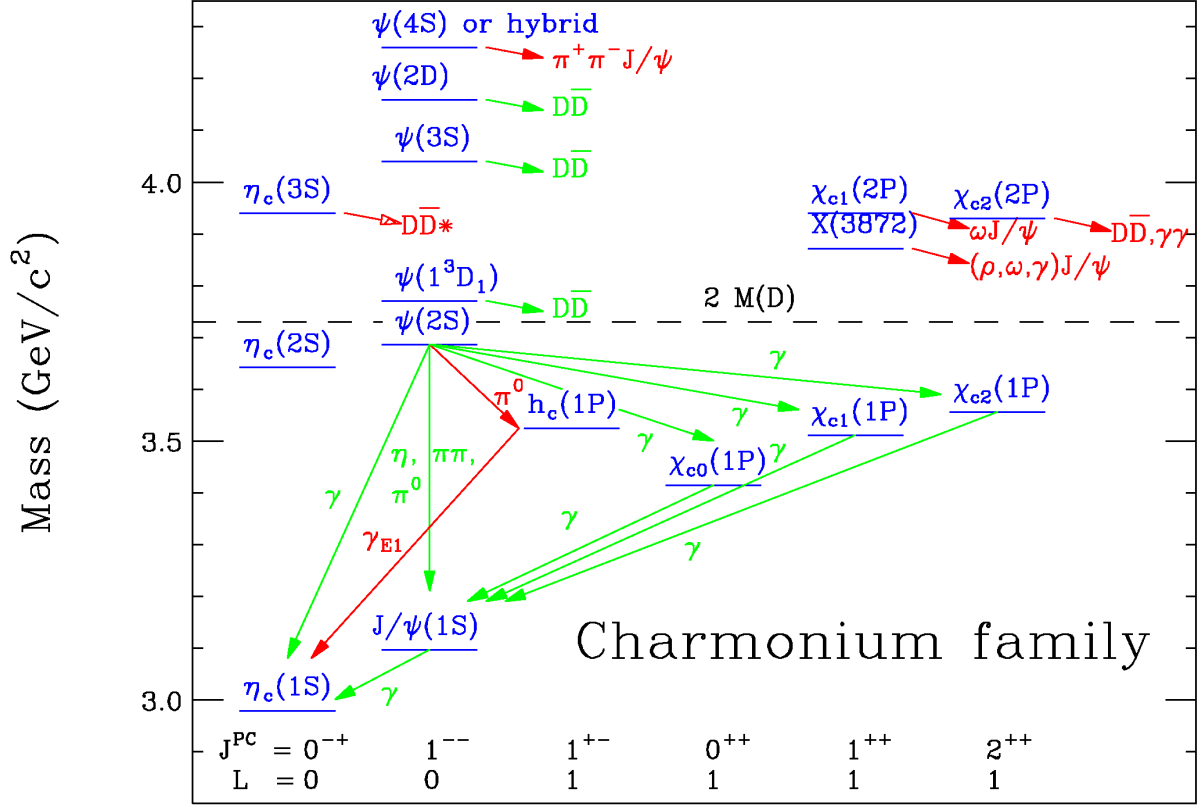


Figure 1.1. Charmonium system and transitions. Red (dark) arrows indicate recently discovered decays and transitions between the levels. The dashed line shows a production threshold for a pair of charmed mesons.

Table 1.2. The number of $c\bar{c}$ mesons that can be produced at SCTF during half a year. Estimates of physical cross sections are based on Refs. [2, 3, 4].

	J/ψ	$\psi(2S)$	$\psi(3770)$	$\psi(4040)$	$\psi(4160)$	$\psi(4415)$
M , GeV	3.097	3.686	3.773	4.039	4.191	4.421
Γ , MeV	0.093	0.286	27.2	80	70	62
σ , nb	~ 3400	~ 640	~ 6	~ 10	~ 6	~ 4
L , fb $^{-1}$	300	150	300	10	100	25
N	10^{12}	10^{11}	2×10^9	10^8	6×10^8	10^8

1. Precision measurement of probabilities for transitions between low-lying levels of charmonium, their masses, total and leptonic or two-photon widths. These parameters are calculated in potential quark models and can also be obtained within lattice QCD. In close future the accuracy of lattice calculations will reach a level of about 1% or better. At SCTF one will be able to measure probabilities of rare, not yet discovered electric $\eta_c(2S) \rightarrow h_c \gamma$ (2.5×10^{-3}), $\psi(3770) \rightarrow \chi_{c0} \gamma$ (2×10^{-4}) and magnetic $\eta_c(2S) \rightarrow J/\psi \gamma$ (3×10^{-5}), $h_c \rightarrow \chi_{c0} \gamma$ ($\sim 10^{-6}$) dipole transitions. Shown in parentheses are transition probabilities expected in the quark model [1]. From the analysis of angular distributions of photons in the $\chi_{cJ} \rightarrow J/\psi \gamma$ and $\psi(2S) \rightarrow \chi_{cJ} \gamma$ decays one can extract the amplitudes of $M2$ and $E3$ transitions interfering with the dominating $E1$ transition and determine an admixture of the D wave state in $\psi(2S)$ (see a review in [5] and references therein).
2. Information about decays of low-lying states of charmonium is very incomplete. For the best-studied J/ψ meson about 45% of hadronic decays only have been measured. For other states the situation is even worse. One of the tasks for SCTF is a systematic study of all low-lying charmonium states. This program, in particular, includes a precision measurement of hadronic transitions between charmonium states with emission of one or two π mesons, η meson, $\psi, h_c \rightarrow 3\gamma$ decays, a photon spectrum in the reaction $\psi \rightarrow \gamma X$, where X is a hadronic state of light quarks, and direct measurement of the probabilities of $\eta_c, \chi_{c0}, \chi_{c1} \rightarrow 2\gamma$ decays.
3. A relatively small width of the J/ψ resonance and a huge data sample provided by SCTF allow an observation of weak J/ψ decays. The total probability of weak decays of J/ψ via a $c \rightarrow sW^+$ transition is $(2-4) \times 10^{-8}$ [6]. Semileptonic $J/\psi \rightarrow D_s^* l \nu$, $D_s l \nu$ and hadronic $J/\psi \rightarrow D_s^+ \rho^-$, $D_s^{*+} \pi^-$ modes have branching fractions of $(3-4) \cdot 10^{-9}$ [6, 7] and can be measured at SCTF. In Standard Model (SM) decays with $\Delta S = 0$ are suppressed. For example, the branching fractions of $J/\psi \rightarrow D^0 \rho^0$ and $J/\psi \rightarrow D^0 \pi^0$ decays are predicted at the level of 2×10^{-11} and 0.6×10^{-11} [7], respectively. This makes such decays sensitive to effects of new physics not described by SM, in particular, to the existence of a flavor-changing neutral current (a $c \rightarrow u$ transition) [8].

Another type of weak processes ($c\bar{c} \rightarrow s\bar{s}$ with W boson exchange) results in decays violating C parity, such as, e.g., $J/\psi \rightarrow \phi\phi$. The expected branching fraction of this decay is sufficiently high ($\sim 10^{-8}$ [9]) for its observation at SCTF.

4. A large sample of ψ meson decays allows a search for phenomena not described by SM, such as violation of CP parity and lepton flavor conservation. Lepton flavor violation can be observed in $J/\psi \rightarrow l\bar{l}'$ decays, where $l, l' = e, \mu, \tau$. Branching fractions of such decays can be related in a model-independent way to branching fractions of μ and τ decays to three leptons [10]. From the limits $B(\mu \rightarrow ee^+e^-) < 10^{-12}$ [2] and $B(\tau \rightarrow \mu e^+e^-) < 2.7 \times 10^{-8}$ [11] one obtains $B(J/\psi \rightarrow \mu e) < 2 \times 10^{-13}$ and $B(J/\psi \rightarrow \tau l) < 6 \times 10^{-9}$. A limit on the decay $\tau \rightarrow \mu e^+e^-$ has been set with a data sample of 5×10^8 τ lepton pairs. Thus, at SCTF J/ψ decays can be more sensitive to lepton flavor violation than those of τ leptons.

One of physical effects beyond SM is the existence of the non-zero electric dipole moment (EDM) of quarks or leptons leading, in particular, to CP violation. J/ψ decays provide the best opportunity to obtain information about the c -quark EDM. To search for CP violation one can use three-body decays, e.g., $J/\psi \rightarrow \gamma\phi\phi$. In this case, one can compose a CP -odd combination of momenta of final particles and an initial electron and determine a parameter describing CP asymmetry which is proportional to EDM. With 10^{12} J/ψ mesons, using the $J/\psi \rightarrow \gamma\phi\phi$ decay one can obtain a sensitivity to the c -quark EDM at the 10^{-15} e·cm

Table 1.3. Exotic vector states in e^+e^- annihilation.

State	M , MeV	Γ , MeV	Production process	
$Y(4260)$	4251 ± 9	120 ± 12	$e^+e^- \rightarrow J/\psi\pi^+\pi^-$	[16, 17]
$Y(4360)$	4346 ± 6	102 ± 10	$e^+e^- \rightarrow \psi(2S)\pi^+\pi^-$	[18, 19]
$Y(4660)$	4643 ± 9	72 ± 11	$e^+e^- \rightarrow \psi(2S)\pi^+\pi^-$	[20, 21]
$Y(4008)$	3891 ± 42	255 ± 42	$e^+e^- \rightarrow J/\psi\pi^+\pi^-$	[17]

level [12]. A two-body $J/\psi \rightarrow \Lambda\bar{\Lambda}$ decay, in which polarizations of final baryons can be measured from the $\Lambda \rightarrow p\pi^-$ decay, can be also used for a search for CP violation. With 10^{12} J/ψ mesons, this decay can be used to set a limit on the Λ -hyperon EDM at the 5×10^{-19} e-cm level [13], two orders of magnitude more stringent than the existing limit.

1.2.2 Study of exotic charmonium-like states

Over the past decade Belle, BABAR, CLEO-c, CDF, D0, BESIII and LHCb experiments have discovered dozens of charmonium states with masses above the open charm threshold [14]. Only a few of them could be identified as excited $c\bar{c}$ mesons. Many of the found states have nonzero electric charge demonstrating their exotic nature. The nature of the new states remains unclear. While trying to explain the properties of the new states, the theory has to admit the existence of molecular states, four-quark states or hydrocharmonium [15].

Vector charmonium-like states, which can be produced at SCTF in the reaction $e^+e^- \rightarrow Y$, are represented in Table 1.3. Masses, widths [2], the processes in which they are produced, as well as references to BABAR and Belle experiments that discovered Y states via radiation return. Existence of three states, the $Y(4260)$, $Y(4360)$ and $Y(4660)$, is reliably established as they were confirmed by at least two experiments. The mass and width of the $Y(4660)$ resonance are consistent within errors with the parameters of the $X(4630)$ state observed by Belle in the process $e^+e^- \rightarrow \Lambda_c^+\Lambda_c^-$ [23]. The existence of a broad peak called $Y(4008)$ found by Belle [17] (7.4σ), but not confirmed by BABAR [22] remains an open question.

Interpretation of the vector Y states as a standard charmonium faces a number of problems: the charmonium spectrum with $J^{PC} = 1^{--}$ quantum numbers is populated with the standard charmonium state and there is no room to accommodate newly observed Y states; the Y states with masses above open charm threshold do not decay to charm mesons unlike expectations; the partial width of the $Y \rightarrow J/\psi\pi^+\pi^-$ decays (> 1 MeV) exceeds by two orders of magnitude the analogous values for the standard charmonium $\psi(3770)(\psi(2S)) \rightarrow J/\psi\pi^+\pi^-$.

The Y states were discovered in $e^+e^- \rightarrow J/\psi\pi^+\pi^-$ and $e^+e^- \rightarrow \psi(2S)\pi^+\pi^-$ processes. Later other processes were studied: $e^+e^- \rightarrow J/\psi\pi^0\pi^0$ [24], $e^+e^- \rightarrow J/\psi K^+K^-$ и $e^+e^- \rightarrow J/\psi K_S K_S$ [25], $e^+e^- \rightarrow J/\psi\eta$ [26, 27], $e^+e^- \rightarrow J/\psi\eta'$ [28], $e^+e^- \rightarrow J/\psi\eta\pi^0$ [29], $e^+e^- \rightarrow h_c\pi^+\pi^-$ [30], $e^+e^- \rightarrow \omega\pi^+\pi^-$ [30]. As expected the $Y(4260)$ signal was observed in the $e^+e^- \rightarrow J/\psi\pi^0\pi^0$ process. Clear evidence of the Y resonances is not seen in other channels.

Relatively large cross sections (50–100 pb), comparable in magnitude with the $e^+e^- \rightarrow J/\psi\pi^+\pi^-$ cross section, were observed in the reactions $e^+e^- \rightarrow J/\psi\eta$ and $e^+e^- \rightarrow h_c\pi^+\pi^-$. In Ref. [26] the $e^+e^- \rightarrow J/\psi\eta$ cross section was fitted by a sum of the $\psi(4040)$ and $\psi(4160)$ resonance contributions. A wide structure was found in the cross section of $e^+e^- \rightarrow h_c\pi^+\pi^-$ in 4.2–4.5 GeV energy

Table 1.4. Charged charmonium-like states.

State	M , MeV	Γ , MeV	Reaction	
$Z(3885)^+$	3883.9 ± 4.5	25 ± 12	$Y(4260) \rightarrow \pi^-(\bar{D}^{*0}D^+)$ $Y(4260) \rightarrow \pi^-(D^{*+}\bar{D}^0)$	[32]
$Z(3885)^0$	3885.7 ± 9.8	35 ± 19	$e^+e^- \rightarrow (D\bar{D}^*)^0$	[33]
$Z(3900)^+$	3891.2 ± 3.3	40 ± 8	$Y(4260) \rightarrow \pi^-(J/\psi\pi^+)$	[34, 35, 36]
$Z(3900)^0$	3894.8 ± 3.5	29 ± 12	$Y(4260) \rightarrow \pi^0(J/\psi\pi^0)$	[37]
$Z(4020)^+$	4022.9 ± 2.8	7.9 ± 3.7	$Y(4260, 4360) \rightarrow \pi^-(h_c\pi^+)$	[38]
$Z(4020)^0$	4023.9 ± 4.3	7.9 ± 3.7	$Y(4260, 4360) \rightarrow \pi^0(h_c\pi^0)$	[39]
$Z(4025)^+$	4026.3 ± 4.5	24.8 ± 9.5	$Y(4260) \rightarrow \pi^-(\bar{D}^{*0}D^{*+})$	[40]
$Z(4025)^0$	4025.5 ± 4.6	23.0 ± 6.1	$e^+e^- \rightarrow (D\bar{D}^*)^0$	[41]
$Z(4055)^+$	4032.1 ± 2.4	26.1 ± 5.3	$Y(4360) \rightarrow \pi^-(\psi(2S)\pi^+)$	[42, 43]
$Z(4050)^+$	4051_{-43}^{+24}	82_{-55}^{+51}	$\bar{B}^0 \rightarrow K^-(\chi_{c1}\pi^+)$	[44]
$Z(4200)^+$	4196_{-38}^{+35}	370_{-110}^{+99}	$\bar{B}^0 \rightarrow K^-(J/\psi\pi^+)$	[45]
$Z(4250)^+$	4248_{-45}^{+185}	177_{-72}^{+321}	$\bar{B}^0 \rightarrow K^-(\chi_{c1}\pi^+)$	[44]
$Z(4430)^+$	4458 ± 15	166_{-38}^{+37}	$\bar{B}^0 \rightarrow K^-(\psi(2S)\pi^+)$	[47, 48]
				[46]
			$\bar{B}^0 \rightarrow K^-(J/\psi\pi^+)$	[45]

range [30]. It was fitted in Ref. [30] by a sum of two resonances with masses about 4.22 and 4.39 GeV and widths of about 70 and 140 MeV, respectively. These values differ from the parameters of the Y resonances listed in Table 1.3.

In 2017 BESIII has measured the cross section of $e^+e^- \rightarrow J/\psi\pi^+\pi^-$ with a high statistical accuracy (19 points with an integrated luminosity of 8.2 fb^{-1}) [31]. This measurement showed that the structure called by $Y(4260)$ cannot be described by a single resonance. Two close resonances with masses $(4222 \pm 3) \text{ GeV}$ and $(4320 \pm 13) \text{ GeV}$ and widths (44 ± 5) and (101 ± 27) , respectively, are needed to describe the cross section data. The first resonance was found to be in good agreement with the resonance near 4.22 GeV detected in $e^+e^- \rightarrow h_c\pi^+\pi^-$ and also with the structure near 4.2 GeV in the cross section of $e^+e^- \rightarrow J/\psi\eta$ [26, 27].

Another class of exotic charmonium-like states, so called Z states, is presented in Table 1.4. The families of charged charmonium-like states $Z(3885)$, $Z(3900)$, $Z(4020)$, $Z(4025)$ were discovered in e^+e^- collisions in the reaction $e^+e^- \rightarrow Z\pi$ near the maximum of the $Y(4260)$ resonance. The triplets $Z(3900)$ и $Z(3885)$ decaying to $J/\psi\pi$ и $\bar{D}D^*$, respectively, have close masses and widths and therefore are considered as the same state.

The parameters of the isotopic triplet $Z(4020)$ decaying into the $h_c\pi$ final states are consistent with the parameters of the states $Z(4025)$ decaying into open-charm final states \bar{D}^*D^* . It is assumed that these two triplets are also one state.

An indication for the existence of a charged state $Z(4055)^+$ decaying into $\psi(2S)\pi^+$ was found

in the $Y(4360)$ decays in the Belle experiment [43]. A study of the $Z(4055)^+$ with much larger statistics were performed recently by BESIII [42]. The $Z(4055)^+$ parameters obtained by BESIII and presented in Table 1.4 are in agreement within errors with the parameters of the $Z(4025)^+$. BESIII has shown [42] that the dynamics of the $e^+e^- \rightarrow \psi(2S)\pi^+\pi^-$ process strongly depends on energy near the $Y(4360)$ peak and that a model with one resonance decaying into $\psi(2S)\pi^+$ is insufficient for a complete description of the Dalitz distribution.

All the Z states discussed above, observed in the process $e^+e^- \rightarrow Z\pi$, have $J^{PC} = 1^{+-}$. The states $Z(4200)$ and $Z(4430)$, observed in B -meson decays, have the same quantum numbers and can be searched for in $Y(4660)$ decays.

Neutral charmonium-like states with positive C-parity, such as $X(3872)$, $X(3915)$, $Y(4140)$, $Y(4274)$, and $X(4500)$ [2, 14] can be observed at SCTF in the processes $e^+e^- \rightarrow X(Y)\gamma$. Recently one of such processes $e^+e^- \rightarrow X(3872)\gamma$ was observed in the BESIII experiment [49].

At SCTF one could study the exotic charmonium-like states with statistics 10-100 times higher than the data accumulated by the BESIII experiment. The energy scan in the range of 3.8-5.0 GeV with integrated luminosity of 100-1000 fb⁻¹ provides the detailed measurement of the processes $e^+e^- \rightarrow J/\psi\pi\pi$, $\psi(2S)\pi\pi$, $J/\psi KK$, $J/\psi\eta$, $J/\psi\eta'$, $h_c\pi\pi$, $\chi_{c\omega}$, etc.

1.3 Spectroscopy of states of light quarks

Charmonium states with a mass smaller than two D -meson masses decay into hadrons consisting of light u , d and s quarks. Selecting special decay modes of $c\bar{c}$ mesons one can select and study states with practically any quantum numbers. Therefore, SCTF is a unique laboratory to study properties of mesons with mass lighter than 3 GeV consisting of u , d , and s quarks.

Of special interest is a search for bound states of two gluons (glueballs), and hybrid states ($q\bar{q}g$). With a $\sim 9\%$ probability the J/ψ meson decays into γgg followed by hadronization of two gluons. Thus, the J/ψ radiative decays are the best sources of glueball production. Lattice QCD calculations [50, 51] predict that the lightest glueballs with the quantum numbers $J^{PC} = 0^{++}$, 2^{++} , and 0^{-+} have masses smaller than 3 GeV. The glueball spectrum obtained in Ref. [50] is shown in Fig. 1.2.

One of the characteristic features allowing to distinguish a glueball from a regular two-quark meson is its anomalously small two-photon width. Therefore, a search for glueballs in J/ψ decays should be complemented by a study of two-photon meson production. (see section 1.8). Previous searches for glueballs failed to give an unambiguous result. Most probably, glueballs are mixed with two-quark mesons. To determine a glueball fraction in a meson, one should study in detail meson properties in different processes and decay modes. For example, for a family of scalars (f_0 , a_0 , K_0^*), one should measure with high precision the processes $J/\psi \rightarrow f_0\gamma$, $f_0\phi$, $f_0\omega$, $a_0\rho$, $K^*(892)K_0^*$, and $\gamma\gamma \rightarrow f_0$, a_0 in different scalar decay modes $f_0, a_0, K_0^* \rightarrow PP, VP, VV, V\gamma$, where V and P are vector and pseudoscalar mesons, respectively. A gluon component will reveal itself as a ratio of decay probabilities unusual for two-quark mesons and appearance of an extra f_0 meson not fitting the scheme of two-quark states. It is worth noting that in addition to gluonic and two-quark states, QCD predicts existence of exotic four-quark mesons and molecular states of two mesons. Existence of such states and their mixing with two-quark states makes even more complicated the pattern of levels of scalar mesons. Detailed systematization of mesons requires very large data samples of J/ψ decays and two-photon events that can be accumulated at SCTF only.

A search for hybrid states is facilitated by the fact that such a state with a smallest mass of 1.3–2.2 GeV/ c^2 should have exotic quantum numbers $J^{PC} = 1^{-+}$, impossible in the quark model (see review [52] and references therein). At the present time there are two candidates for the

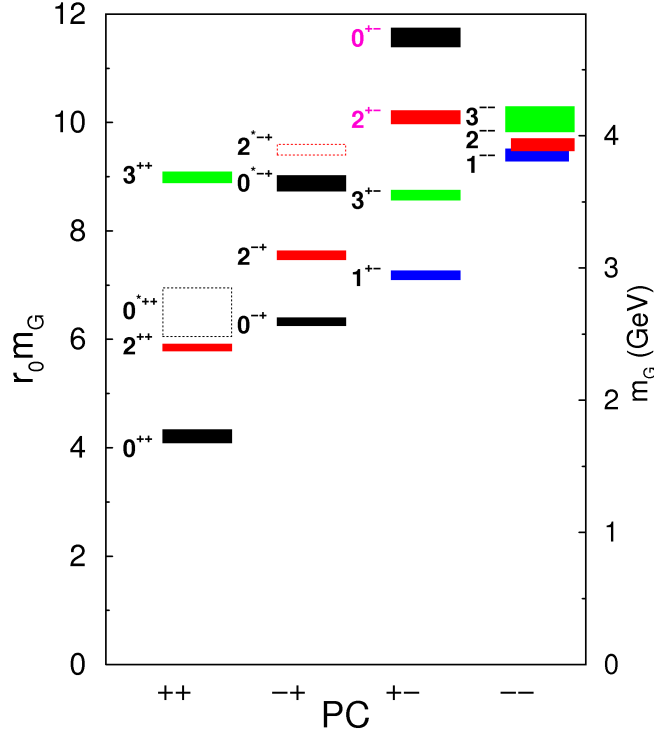


Figure 1.2. Spectrum of glueball masses [50].

light-quark hybrid: $\pi_1(1400)$ and $\pi_1(1600)$. Properties of these states are badly investigated and even their existence should be confirmed. The π_1 states were observed primarily in diffractive experiments $\pi^- N \rightarrow \pi_1^- N$. SCTF allows a study of completely different production mechanisms: S -wave decay $\chi_{c1} \rightarrow \pi\pi_1$ and P -wave decay $J/\psi \rightarrow \rho\pi_1$. One should study main decay modes expected for a hybrid: $\rho\pi$, $b_1\pi$, $f_1\pi$, $\eta\pi$, and $\eta'\pi$. It is expected that the lightest state of a hybrid with non-exotic quantum numbers 0^{-+} is also in the mass region around 2 GeV. This state can be searched for in the decay $\chi_{c0} \rightarrow \pi\pi_1$ as well as in ψ meson decays.

The BESII collaboration observed an anomalously strong near-threshold excess in the $p\bar{p}$ mass spectrum in the $J/\psi \rightarrow \gamma p\bar{p}$ radiative decay. The structure ($X(p\bar{p})$) was fitted with an S -wave Breit-Wigner resonance function with mass about 1860 MeV and width less than 30 MeV [53]. This result was confirmed by the CLEO-c [54]. The observed structure can be manifestation of a hypothetical $p\bar{p}$ bound state, baryonium [55].

The study of the structure $X(p\bar{p})$ was continued in the BESIII experiment [56, 57]. The partial-wave analysis of the $J/\psi \rightarrow \gamma p\bar{p}$ and $\psi' \rightarrow \gamma p\bar{p}$ decays in the $p\bar{p}$ invariant mass region below 2.2 GeV shows that the mass of the $X(p\bar{p})$ is 1832 ± 20 MeV, its width is less than 76 MeV, and its $J^{PC} = 0^{-+}$ [57].

In the $J/\psi \rightarrow \gamma\eta'\pi^+\pi^-$ decay, the expected contributions of the $f_1(1510)$ and η_c resonances together with the new structures $X(1835)$, $X(2120)$, $X(2370)$, and $X(2600)$ were observed in the the $\eta'\pi^+\pi^-$ invariant mass spectrum [58, 59]. The resonance $X(1835)$ has the width about 200 MeV. The photon angular distribution in $J/\psi \rightarrow \gamma X(1835)$ decay corresponds to the $X(1835)$ quantum numbers $J^P = 0^-$. The slope of the $X(1835)$ resonance line-shape has a significant abrupt change at the $p\bar{p}$ mass threshold. This may be due to opening the $X(1835) \rightarrow p\bar{p}$ decay. So, the $X(1835)$ and $X(p\bar{p})$ may be the same resonance.

The $X(1835)$ signal is seen in the other decay modes. For example, the decay $J/\psi \rightarrow$

Table 1.5. The maximum values of the $e^+e^- \rightarrow D\bar{D}^{(*)}$ and $e^+e^- \rightarrow D_s\bar{D}_s^{(*)}$ cross sections [61, 62] and the energies where the cross sections are maximal.

	D^+D^-	$D^0\bar{D}^0$	$D\bar{D}^*$	$D_s^+D_s^-$	$D_s^+D_s^{*-}$
E , GeV	3.77	3.77	4.02	4.01	4.17
σ , nb	2.88 ± 0.05	3.61 ± 0.06	7.5 ± 0.4	0.27 ± 0.03	0.92 ± 0.05

$\gamma X(1835) \rightarrow \gamma K_S K_S \eta (\gamma f_0(980) \eta)$ was observed [60]. The resonance mass, width, and quantum numbers in this decay are in agreement with those in the $J/\psi \rightarrow \gamma \eta' \pi^+ \pi^-$ decay.

Experiments with the BESIII detector at the tau-charm factory BEPCII indicate the rich resonance physics in the mass region below 3 GeV. Statistics of the BESIII experiment is not enough for unambiguous interpretation of the observed structures. The studies of these states will be an important part of the physical program of SCTF factory.

1.4 Physics of D -mesons

The values of the D -meson production cross sections are listed in Table 1.5. With the luminosity distribution given in Table 1.1, about 10^9 pairs of charged and neutral D mesons, and about 2×10^7 pairs of D_s mesons can be produced at CTF.

These numbers do not exceed the numbers of D mesons produced at existing B -factories at the e^+e^- c.m. energy of 10.58 GeV. There is, however, crucial difference between D -meson events at 10.58 and 3.77 GeV, which makes low energy measurements preferable and allows more precise results to be obtained with lower statistics:

- The multiplicity of charged and neutral particles is about two times lower at $\psi(3770)$ than at $\Upsilon(4S)$.
- In contrast to $\Upsilon(4S)$, where D meson production is accompanied by many other particles, at the threshold pure $D\bar{D}$ events are produced. This allows to use additional kinematic constraints for the event reconstruction. In particular, in events with leptonic or semileptonic decay of one of the D mesons, the neutrino is reconstructed with the additional constraint of zero missing mass. Use of the double-tag method, when one of the D mesons is fully reconstructed, while the other is studied, strongly reduces background and allows to perform precise measurements of absolute decay probabilities.
- D and \bar{D} mesons are produced in a quantum-coherent state, for example, with $J^{PC} = 1^{--}$ in the reaction $e^+e^- \rightarrow D\bar{D}$ or $J^{PC} = 0^{++}$ in the reaction $e^+e^- \rightarrow D\bar{D}\gamma$. The coherence allows to use simple techniques for a study of $D\bar{D}$ mixing, search for CP violation, measurement of strong phases, and probabilities of decays to CP states.

At SCTF a systematic study of D -meson properties will be performed.

1.4.1 Spectroscopy of D mesons

There are three types of charmed mesons: charged D^\pm mesons with the quark structure of (cd) , neutral D^0 and \bar{D}^0 mesons with the structure of (cu) , and D_s^\pm mesons with the structure of (cs) .

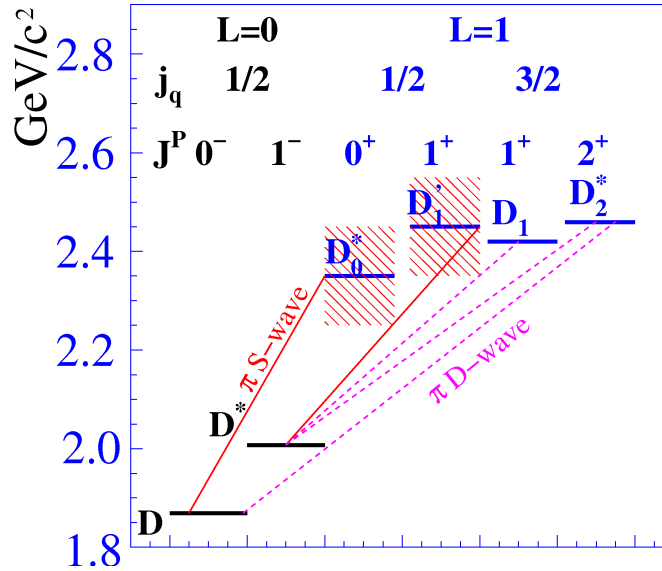


Figure 1.3. The scheme of the D -meson levels.

Let us consider the orbital-excited states of the D -meson. Since this meson consists of the heavy c -quark and the light antiquark, the heavy quark effective theory could be used to describe this system. In limit of accurate symmetry by flavor and spin \vec{s}_Q of the heavy quark, the total angular momentum of the light quark $\vec{j}_q = \vec{L} + \vec{s}_q$ commutes with the Hamiltonian of the system and conserves its value. In such a case, we can classify the states by the total angular momentum of the light quark \vec{j}_q and spin of the meson $\vec{J} = \vec{j}_q + \vec{s}_Q$. The classification scheme of low-lying levels of D mesons is shown in Fig. 1.3. From the six states shown, the two lowest have $L = 0$, while the four others have $L = 1$. The moment j_q coincides with the spin of the light quark s_q in the case of the zero relative angular momentum L between the light and heavy quarks. The total spin J can be equal to 0 or 1. In the first case, we have the ground state of the D meson with the $J_{j_q}^P = 0_{1/2}^-$, and the second case corresponds to the vector state with the $J_{j_q}^P = 1_{1/2}^-$, which is called the D^* meson.

States with the relative angular momentum L equal to 1 are called the D^{**} mesons. The D^{**} states include two doublets with $j_q = 1/2$ ($J_{j_q}^P = 0_{1/2}^+, 1_{1/2}^+$) and $j_q = 3/2$ ($J_{j_q}^P = 1_{3/2}^+, 2_{3/2}^+$). Such a classification is applicable to all three types of D mesons.

Conservation of a P-parity and angular momentum in strong interactions imposes constraints on decays of the D^{**} states to the $D^{(*)}\pi$. Two states with $j_q = 1/2$ decay to the $D^{(*)}\pi$ system in S wave and two other states with $j_q = 3/2$ decay in D wave. Since the decay width is proportional to the nonrelativistic momentum of the final particles to the power of $2l + 1$, where l is a relative angular momentum between $D^{(*)}$ and π , the states with $j_q = 3/2$ have small decay widths of order of tens of MeV and are expected to be narrow, but the states with $j_q = 1/2$ are expected to be broad with widths of hundreds of MeV. The spin-flavor symmetry of the heavy quark is not accurate. Therefore, if the powers of $1/m_Q$ are taken into account, the total angular momentum is not a "good" quantum number any longer. It leads to the fact that physical $D_1'(2430)^0$ and $D_1(2420)^0$ states are linear combinations of the pure states with $j_q = 1/2$ and $j_q = 3/2$. We use the following nomenclature of the D^{**} states: $D_0^*(2400)$ with $J_{j_q}^P = 0_{1/2}^+$, $D_1'(2430)$ with $J_{j_q}^P = 1_{1/2}^+$, $D_1(2420)$ with $J_{j_q}^P = 1_{3/2}^+$ and $D_2^*(2460)$ with $J_{j_q}^P = 2_{3/2}^+$ (see Fig. 1.3).

The spectrum of neutral D mesons obtained in the relativistic quark model is shown in Fig. 1.4. The mass spectrum of the $c\bar{u}$ system is shown for the ground states with $nL = 1S$, where n is the radial quantum number, as well as for the orbital excitations with angular momenta $L = 1, 2, 3$

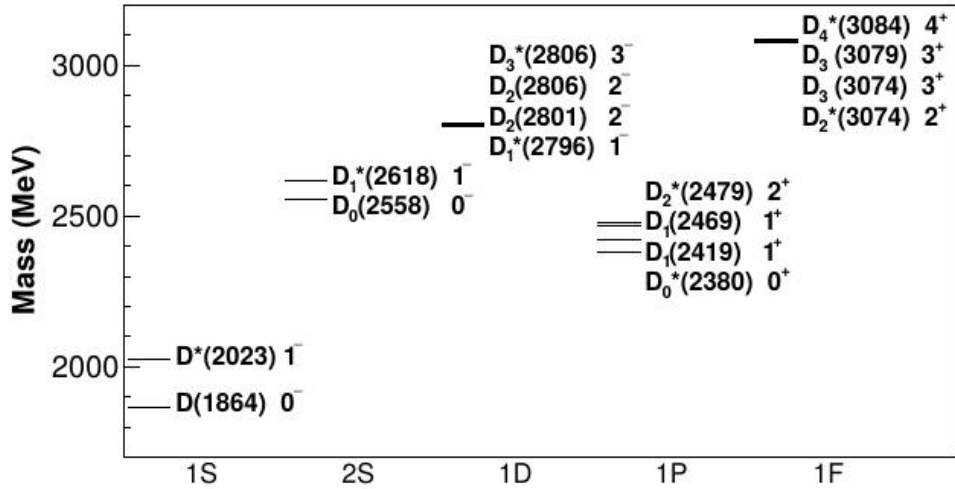


Figure 1.4. The mass spectrum for neutral D mesons in the relativistic quark model [63]. Masses are scaled such that mass of the ground state coincides with mass of the D^0 meson.

Table 1.6. The parameters of D and D_s mesons. The masses and widths are given in MeV.

charge		D	D^*	D_0^*	D_1'	D_1	D_2^*
\pm	M	1869.58 ± 0.09	2010.26 ± 0.05	2351 ± 7		2423.2 ± 2.4	2465.4 ± 1.3
	Γ	1040 ± 7 fs	0.083 ± 0.002	230 ± 17		25 ± 6	46.7 ± 1.2
0	M	1864.83 ± 0.05	2006.85 ± 0.05	2318 ± 29	2427 ± 36	2420.8 ± 0.5	2460.6 ± 0.2
	Γ	410.1 ± 1.5 fs	< 2.1	267 ± 40	384 ± 120	31.7 ± 2.5	47.7 ± 1.3
charge		D_s	D_s^*	D_{s0}^*	D_{s1}'	D_{s1}	D_{s2}^*
\pm	M	1968.27 ± 0.10	2112.1 ± 0.4	2317.7 ± 0.6	2459.5 ± 0.6	2535.10 ± 0.06	2569.1 ± 0.8
	Γ	500 ± 7 fs	< 1.9	< 3.8	< 3.5	$< 0.92 \pm 0.05$	16.9 ± 0.8

($1P$, $1D$ and $1F$) and also for the first radial excitation ($2S$). Predictions for the $1S$ and $1P$ states with $J^P = 1^+$ and $J^P = 2^+$ are in good agreement with measurements (within 20 – 30 MeV). Agreement for the $1P$ states with $J^P = 0^+$ is about 100 MeV. Recently BABAR [64] and LHCb [65] collaborations found excited $2S$ and $1D$ states of D_J mesons as well as the possible superposition of the different $1F$ states.

The known low-lying states of D and D_s mesons [2] are listed in Table 1.6. Study of properties of the excited D_J and D_{sJ} states requires further theoretical and experimental work. Presently, experimental information about the D_J and D_{sJ} mesons is not complete. In the frame of the naive quark model the P -wave D_{sJ} states with $j_q = 1/2$ are expected to be broad and should decay to the DK and D^*K systems [66]. However, the measured masses of the D_{s0}^* (2317) and D_{s1}' (2460) states lie by about 40 MeV below the DK and D^*K thresholds. Therefore, they are narrow. To explain this discrepancy, the hypotheses that these $c\bar{s}$ states are not conventional mesons, but have, for example, four-quark or DK molecular structure are suggested.

Precise knowledge of the spectroscopic properties of the D_J and D_{sJ} states is important to determine the CKM matrix elements $|V_{cb}|$ and $|V_{ub}|$, to study semileptonic $b \rightarrow c$ decays and to search for "new physics" evidence. The properties of the D_J and D_{sJ} systems can

Table 1.7. Most precise measurements of the branching fractions of D and D_s meson leptonic decays.

	D^+	D_s^+
$e^+\nu$	$< 8.8 \times 10^{-6}$ [74]	$< 8.3 \times 10^{-5}$ [76]
$\mu^+\nu$	$(3.71 \pm 0.19 \pm 0.06) \times 10^{-4}$ [75]	$(5.31 \pm 0.28 \pm 0.20) \times 10^{-3}$ [76]
$\tau^+\nu$	$< 1.2 \times 10^{-3}$ [74]	$(5.70 \pm 0.21_{-0.30}^{+0.31}) \times 10^{-2}$ [76]

be studied in detail at SCTF, where D_J and D_{sJ} mesons can be produced in the reactions $e^+e^- \rightarrow D_0^*\bar{D}^*$, $D_1^{(\prime)}\bar{D}^{(*)}$, $D_2^*\bar{D}^{(*)}$, which have thresholds in the energy range of 4.3 – 4.7 GeV and the cross sections of about 1 nb [67, 68]. The integrated luminosity of about 50 fb^{-1} , collected in the 4.3–5.0 GeV energy range, will be sufficient to perform a careful study of D_J and D_{sJ} properties. A detailed measurement of exclusive charm-production cross sections up to the 5–6 GeV will allow to observe production of the known higher excited D and D_s states ($D_{sJ}(2632)$ [69], $D_{sJ}(2708)$ [70], and $D_{sJ}(2860)$ [71]), and find new states of this family.

1.4.2 Charmed-meson decays

Charmed-meson decays are a unique source for studying the dynamics of strong interactions. SCTF allows to perform a detailed study of D and D_s meson decays including high-precision measurements of decay probabilities, Dalitz plot analyses for three-body decays, and dynamics study of four-body decay distributions. It is expected that in the near future many parameters extracted from D and D_s decays, such as the decay constants, f_D and f_{D_s} , and form factors of semileptonic decays, will be calculated with high accuracy in the framework of the lattice QCD (LQCD). Precision measurements of D decays will allow to control these calculations and extrapolate them to the B meson region. As a result, a significant decrease of the theoretical uncertainties in the extraction of the CKM matrix elements V_{cd} , V_{cs} , V_{td} , V_{ts} , V_{ub} and V_{cb} from the precision measurements of various B meson decays is expected. For a precise measurement of the angles β (ϕ_1) and γ (ϕ_3) of the unitarity triangle at a super- B factory, neutral D -meson data are required, such as $D^0 - \bar{D}^0$ mixing parameters, the amplitude ratio of the D^0 and \bar{D}^0 decays into $K^+\pi^-$, the strong phase difference between these amplitudes, Dalitz distributions for the three-body hadronic decays, for example, into the $K_S^0\pi^+\pi^-$ final state [72, 73]. All these data can be obtained at SCTF. Below, the current status of leptonic and semileptonic D decays and CTF possibilities for their measurements are discussed in more detail.

In SM the width of a leptonic D^+ decay is given by

$$\Gamma(D^+ \rightarrow l^+\nu) = \frac{G_F^2}{8\pi} f_D^2 m_l^2 M_D \left(1 - \frac{m_l^2}{M_D^2}\right)^2 |V_{cd}|^2,$$

where M_D and m_l are the D -meson and lepton masses, and G_F is the Fermi constant. A similar formula with the substitution of V_{cs} for V_{cd} is used for a D_s leptonic decay. The most precise experimental data on leptonic decays of the D and D_s mesons obtained in the CLEO [74], BESIII [75] and Belle [76] experiments, are listed in Table 1.7. The $D^+(D_s^+) \rightarrow e^+\nu$ branching fractions are expected to be about $10^{-8}(10^{-7})$ and can hardly be measured even at SCTF. The expected branching fraction for the $D^+ \rightarrow \tau^+\nu$ (about 1.2×10^{-3}) is at the level of the CLEO upper limit.

Table 1.8. The experimental values of the D and D_s decay constants [75, 76] in comparison with the LQCD calculation [78].

	Experiment	Theory
f_D , MeV	$203.2 \pm 5.3 \pm 1.8$	$202.3 \pm 2.2 \pm 2.6$
f_{D_s} , MeV	$255.5 \pm 4.2 \pm 5.1$	$258.7 \pm 1.1 \pm 2.9$
f_{D_s}/f_D	$1.26 \pm 0.05 \pm 0.03$	1.2788 ± 0.0264

In SM the unitarity constraints allow to determine the CKM matrix elements V_{cd} and V_{cs} from experimental data with high precision: $|V_{cd}| = 0.2249(3)$, $|V_{cs}| = 0.97347(7)$ [77]. Therefore, the measured leptonic decay branching fractions can be used to extract the decay constants and their ratio shown in Table 1.8.

In the last column of Table 1.8 the results of the most accurate-to-date LQCD calculation [78] are listed. It is seen that, firstly, experimental measurements and theoretical predictions are consistent, and secondly, the claimed accuracy of the predictions has already reached the level of 1–2 % and is better than the experimental accuracy. An additional test of the Standard Model in this case may be checking the lepton universality, i.e., comparing the D_s decay widths into the $\tau\nu$ and $\mu\nu$ final states. The current experimental value of this ratio $10.73 \pm 0.69 \pm_{-0.53}^{+0.56}$ [76] is consistent with the theoretical value 9.762 ± 0.031 , but has a noticeably lower accuracy. Thus, to confirm the SM predictions confidently, new more accurate experimental data are required.

The total branching fractions of the semileptonic D decays measured by CLEO are $B(D^0 \rightarrow Xe^+\nu_e) = (6.46 \pm 0.17 \pm 0.13)\%$, $B(D^+ \rightarrow Xe^+\nu_e) = (16.13 \pm 0.20 \pm 0.33)\%$ [79]. For D_s the same branching fraction is $B(D_s^+ \rightarrow Xe^+\nu) = (6.52 \pm 0.39 \pm 0.15)\%$. One of the goals of SCTF is a high-statistics study of different exclusive decay modes, including Dalitz plot analyses and extraction of the form factors describing the hadronization of the primary quarks produced in D decays.

The best studied are semileptonic D decays into pseudoscalar π and K mesons. These decays are described well with a single form factor. For example, the width for the $D \rightarrow K\ell\nu$ decay is proportional to

$$\frac{d\Gamma(q^2)}{dq^2} \propto |f_+(q^2)|^2 |V_{cs}|^2,$$

where q is the difference of the D and K four-momenta and $f_+(q^2)$ is π and K meson form factor. From measurements, the q^2 dependence of the form factor and the product $f_+(0)|V_{cs}|$ are extracted. The value of the form factor $f_+(0)$ can be calculated theoretically, for example, in the framework of LQCD. The current accuracy of these calculations is about 10%. The theoretical values of the form factors, $f_+^\pi(0) = 0.64(3)(6)$ and $f_+^K(0) = 0.73(3)(7)$ [80], are consistent with experimental values. The most precise measurement of the form factors was performed by the BESIII Collaboration [81]: $f_+^\pi(0) = 0.6372 \pm 0.0008 \pm 0.0044$, $f_+^K(0) = 0.7368 \pm 0.0026 \pm 0.0036$. To obtain these experimental values, the elements of the CKM matrix satisfying the unitarity condition [2] are used. It is expected that the accuracy of theoretical calculations of the form factors will improve to a 1% level. In this case the semileptonic decays can be used for measurements of V_{cs} and V_{cd} and to test the unitarity relation.

Other semileptonic D and D_s decay modes, excluding $D \rightarrow K^*\ell\nu$, are measured with low accuracy. For their detailed study, large statistics are needed which can be collected only at

SCTF. For example, an integrated luminosity of 100 fb^{-1} is required to measure the $D \rightarrow \rho e \nu$ branching fraction with a 0.5% accuracy, and ten times more statistics are needed for the precise measurement of three form factors describing this decay.

1.4.3 $D^0-\bar{D}^0$ Mixing

One of the main goals of the SCTF is a study of $D^0-\bar{D}^0$ mixing. The transitions $D^0 \Leftrightarrow \bar{D}^0$ are a result of the interaction which changes the internal quantum number charm by $\Delta C = 2$. Due to these transitions of D mesons, the eigenstates of the mass matrix are the following:

$$|D_1\rangle = \frac{1}{\sqrt{|p|^2 + |q|^2}}(p|D^0\rangle + q|\bar{D}^0\rangle),$$

$$|D_2\rangle = \frac{1}{\sqrt{|p|^2 + |q|^2}}(p|D^0\rangle - q|\bar{D}^0\rangle).$$

In case of the CP -invariant interaction $p = q$ and the eigenstates $|D_1\rangle$ and $|D_2\rangle$ have a definite internal CP -parity. As a rule, two non-dimensional parameters are used for a description of mixing:

$$x \equiv \frac{\Delta m}{\Gamma}, \quad y \equiv \frac{\Delta \Gamma}{2\Gamma},$$

where Δm and $\Delta \Gamma$ are the differences of masses and widths of the $|D_2\rangle$ and $|D_1\rangle$ states and Γ is the average width of a D^0 meson. In SM the values of these parameters result from long-distance interactions (due to intermediate-meson transitions) and, therefore, predictions for their values have poor precision [82]. It is predicted that x and y can reach the values of ~ 0.01 . The most precise data for D -meson mixing were obtained in B factory and the LHCb experiments. Averaging the current data, which was done by HFAG [83] under the assumption of CP -invariance, gives the following results:

$$x = (4.64^{+1.40}_{-1.51}) \times 10^{-3}, \quad y = (6.25 \pm 0.77) \times 10^{-3}. \quad (1.1)$$

In SCTF experiments, D^0 and \bar{D}^0 mesons will be produced in a coherent state with the odd C -parity in the process $e^+e^- \rightarrow D^0\bar{D}^0(n\pi^0)$ and the even one in the process $e^+e^- \rightarrow D^0\bar{D}^0\gamma(n\pi^0)$. This can be used for a measurement of mixing. In case of a symmetric SCTF (the energies of colliding electrons and positrons are equal), a study of time evolution of the $D^0\bar{D}^0$ system is not possible due to a small lifetime of the D -mesons. Therefore, time integrated values will be analyzed below. The decays to the following final states will be considered as suggested in Ref. [84]:

- Hadron final states f and \bar{f} which do not have a definite CP -parity, for example, $K^-\pi^+$, which is a Cabibbo-favored (CF) decay of D^0 , or doubly Cabibbo suppressed (DCF) decay of \bar{D}^0 ;
- Semileptonic and leptonic final states, l^+ and l^- , which, without mixing, uniquely determine the flavor of a D^0 -meson;
- The states which are eigenstates of CP parity, S_+ and S_- .

Under the assumption of CP invariance, the probability of producing two D^0 mesons in various combinations in the final state depends on the following parameters: x , y , the amplitudes

$$A_f = \langle f|D^0\rangle, \quad A_l = \langle l^+|D^0\rangle, \quad A_{S_{\pm}} = \langle S_{\pm}|D^0\rangle, \quad (1.2)$$

Table 1.9. The ratios of decay probabilities of the $D^0\bar{D}^0$ state to various final states. Only leading-order terms in a power series expansion in r_f^2 , x and y are given.

	$C = -1$	$C = +1$
$(1/4) \cdot (\Gamma_{lS_+}\Gamma_{S_-}/\Gamma_{lS_-}\Gamma_{S_+} - \Gamma_{lS_-}\Gamma_{S_+}/\Gamma_{lS_+}\Gamma_{S_-})$	y	$-y$
$(\Gamma_{fl-}/4\Gamma_f) \cdot (\Gamma_{S_-}/\Gamma_{lS_-} - \Gamma_{S_+}/\Gamma_{lS_+})$	y	$-y$
$(\Gamma_{f\bar{f}}/4\Gamma_f) \cdot (\Gamma_{S_-}/\Gamma_{\bar{f}S_-} - \Gamma_{S_+}/\Gamma_{\bar{f}S_+})$	$y + r_f z_f$	$-(y + r_f z_f)$
$(\Gamma_f\Gamma_{S_+S_-}/4) \cdot (1/\Gamma_{fS_-}\Gamma_{S_+} - 1/\Gamma_{fS_+}\Gamma_{S_-})$	$y + r_f z_f$	0
$(\Gamma_{\bar{f}}/2) \cdot (\Gamma_{S_+S_+}/\Gamma_{\bar{f}S_+}\Gamma_{S_+} - \Gamma_{S_-S_-}/\Gamma_{\bar{f}S_-}\Gamma_{S_-})$	0	$y + r_f z_f$
$\Gamma_{ff}/\Gamma_{f\bar{f}}$	R_M	$2r_f^2 + r_f(z_f y - w_f x)$
$\Gamma_{fl+}/\Gamma_{fl-}$	r_f^2	$r_f^2 + r_f(z_f y - w_f x)$
$\Gamma_{l\pm l\pm}/\Gamma_{l+l-}$	R_M	$3R_M$

the absolute value and phase of the ratio for the DCF and CF amplitudes

$$r_f e^{-\delta_f} = -\langle f|\bar{D}^0\rangle/\langle f|D^0\rangle. \quad (1.3)$$

One can also determine the following parameters:

$$R_M \equiv (x^2 + y^2)/2, \quad z_f \equiv 2 \cos \delta_f, \quad w_f \equiv 2 \sin \delta_f. \quad (1.4)$$

The ratios of decay probabilities of the $D^0\bar{D}^0$ system to various final states are shown in Table 1.9. Γ_{jk} means D^0 decay to the j state and \bar{D}^0 to the k state. Γ_j means D^0 decay to the j state and \bar{D}^0 to any final state.

As shown in the Table 1.9, evidence for events $D^0\bar{D}^0 \rightarrow (K^-\pi^+)(K^-\pi^+)$ and $D^0\bar{D}^0 \rightarrow (K^-e^+\nu_e)(K^-e^+\nu_e)$ in $\psi(3770)$ decays is possible via mixing only. For 10^9 $D^0\bar{D}^0$ events and for $R_M = 3 \times 10^{-5}$ obtained using the measured x and y values, it is expected to detect about 60 of these events. Results of Ref. [84] were used for estimation of the detection efficiency, which corresponds to CLEO performance. Thus, a statistical sensitivity for a measurement of R_M using these two decays only is about 4×10^{-6} . A systematic uncertainty will mainly depend on the quality of particle identification.

The probabilities of inclusive $D^0\bar{D}^0$ decays to the $S_{\pm}X$ final states are proportional to $(1 \mp y)$ [84]. This allows to measure a y parameter. For double ratios shown in the first and second rows of Table 1.9, the substantial part of systematic errors, which originates from data-MC simulation difference in track reconstruction and particle identification, cancels. A statistical precision of y determined from the ratio $(1/4) \cdot (\Gamma_{lS_+}\Gamma_{S_-}/\Gamma_{lS_-}\Gamma_{S_+} - \Gamma_{lS_-}\Gamma_{S_+}/\Gamma_{lS_+}\Gamma_{S_-})$ was estimated in [85] to be $26/\sqrt{N_{DD}}$, where N_{DD} is the number of produced $D^0\bar{D}^0$ pairs. For $N_{DD} = 10^9$ it equals 0.0008, i.e., 2.5 times better than the current experimental precision.

The value of the strong phase δ_f in the $K^-\pi^+$ final state, which is important, for example, for a measurement of $D^0\bar{D}^0$ mixing at B -factories, can be measured using the relations listed in the third and fourth rows of Table 1.9. The expected statistical precision for a measurement of $\cos \delta_f$ is estimated as $444/\sqrt{N_{DD}} = 0.014$ [85], that corresponds to a precision of 0.05 for δ_f . At the present time the average value of this parameter is $0.14_{-0.20}^{+0.17}$.

Measurements, which can be performed with the $D^0\bar{D}^0$ system in the \mathcal{C} -even state, have the best sensitivity for y . For a measurement of y with a precision of 8×10^{-4} from the ratio

$\Gamma_{f_l^+}/\Gamma_{f_l^-}$, 3×10^8 $D^0\bar{D}^0$ pairs are required. This number of \mathcal{C} -even $D^0\bar{D}^0$ pairs can be produced in the process $e^+e^- \rightarrow D^0\bar{D}^{*0} \rightarrow D^0\bar{D}^0\gamma$ with an integrated luminosity of 250 fb^{-1} collected at an energy of 4.02 GeV. This measurement is also sensitive to the parameter x . However, as it is shown in Table 1.9, a sensitivity to x is worse than for y due to δ_f infinitesimality. As it was shown in a recent paper [86], this problem can be successfully solved in case of a three-particle decay of D^0 , for example, to $K_S^0\pi^+\pi^-$ or $K^+\pi^-\pi^0$. An important feature of the suggested method is that for the \mathcal{C} -odd $D^0\bar{D}^0$ state all effects of mixing, which have impact on the density of events on the Dalitz plot, cancel in the first order of x and y . In the case of the \mathcal{C} -even one, the effects of mixing are doubled compared to a non-coherent D^0 decay. Thus, in this experiment there is a possibility to measure x and y by a direct comparison of the distribution of events on the Dalitz plot for the \mathcal{C} -even and -odd $D^0\bar{D}^0$ states. As it was shown in Ref. [86], statistical errors for x and y are approximately equal. It is expected that many systematic errors in this measurement will cancel because the states with opposite charge parity will be produced simultaneously and in similar kinematic states during data taking. Furthermore, unlike other methods described above, this method does not require measuring absolute probabilities of D^0 decays. It can be estimated that for an integrated luminosity of about 1 ab^{-1} , a precision of measuring mixing parameters will be not worse than at the Super B factory for an integrated luminosity of 10 ab^{-1} [87].

1.4.4 Search for CP violation

A search for CP violation in $D_{(s)}$ decays is one of the most interesting experiments to be performed at SCTF. The Standard Model predicts a very small CP asymmetry in reactions with charmed particles. The maximum effect of about 10^{-3} is expected in the Cabibbo-suppressed (CS) D decays [82]. An observation of a CP asymmetry in CF and DCS decays at any level or an asymmetry higher than 10^{-3} in CS decays will clearly indicate the presence of new BSM physics. The exceptions are the decays to the final states containing K_S^0 or K_L , for example, $D \rightarrow K_S^0\pi$, in which the CP asymmetry arises from the fact that a K_S^0 meson is not a CP eigenstate. For the decay $D^\pm \rightarrow K_S^0\pi^\pm$, a CP asymmetry is predicted with a relatively high accuracy, $(3.32 \pm 0.06) \times 10^{-3}$ [82].

We can distinguish three types of CP violation:

- The direct CP violation in $\Delta\mathcal{C} = 1$ transitions reveals itself as an inequality of the amplitude of $D_{(s)}$ meson decay (A_f) and the corresponding CP -conjugate amplitude ($\bar{A}_{\bar{f}}$). CP violation can be observed when the decay amplitude is a sum of two amplitudes with different weak and strong phases:

$$A_f = |A_1|e^{i(\delta_1+\phi_1)} + |A_2|e^{i(\delta_2+\phi_2)}. \quad (1.5)$$

The weak phase changes its sign under the CP transformation ($\phi_i \rightarrow -\phi_i$), while the strong phase δ_i does not.

- CP violation in $D^0-\bar{D}^0$ mixing due to $\Delta\mathcal{C} = 2$ transitions reveals itself in a deviation of the ratio $R_m = |p/q|$ from unity.
- In decays of neutral D mesons CP violation can be observed in the interference of decays with mixing ($D^0 \rightarrow \bar{D}^0 \rightarrow f$) and without it ($D^0 \rightarrow f$). This type of CP violation is described by the parameter

$$\varphi = \arg \lambda_f = \arg \left(\frac{q}{p} \frac{\bar{A}_f}{A_f} \right). \quad (1.6)$$

CP violation in mixing leads to the difference between the widths of semileptonic decays with a wrong sign of the decay lepton $\Gamma(\bar{D}^0 \rightarrow l^+ X) \neq \Gamma(D^0 \rightarrow l^- X)$. For example, in $\psi(3770)$ decays the following asymmetry can be measured

$$A_{SL} = \frac{\Gamma_{l^+l^+} - \Gamma_{l^-l^-}}{\Gamma_{l^+l^+} + \Gamma_{l^-l^-}} = \frac{1 - |q/p|^4}{1 + |q/p|^4}.$$

For 10^9 $D^0\bar{D}^0$ pairs, about 20 $(K^\pm e^\mp \nu)(K^\pm e^\mp \nu)$ events are expected to be produced. With these statistics, the $|q/p|$ ratio will be determined with about 6% accuracy. The current value of the parameter $|q/p|$ is $0.89_{-0.07}^{+0.08}$.

Direct CP violation can be observed as a difference between the decay widths for charged D mesons:

$$A_{\pm}^{CP} = \frac{\Gamma(D^- \rightarrow f^-) - \Gamma(D^+ \rightarrow f^+)}{\Gamma(D^- \rightarrow f^-) + \Gamma(D^+ \rightarrow f^+)}.$$

For neutral D mesons, all three types of CP violation contribute to the same asymmetry parameter. The current values of the CP asymmetry measured in D and D_s meson decays are listed in Table 1.10 and Table 1.11, respectively.

In Ref. [61] the CP asymmetries were measured by the CLEO detector using a data sample of 3.0×10^6 $D^0\bar{D}^0$ pairs and 2.4×10^6 D^+D^- pairs. At SCTF, for many decays the statistical error of asymmetry can be decreased to a level of 10^{-3} - 10^{-4} . The systematic error is dominated by uncertainties in track reconstruction and particle identification. The reconstruction and identification efficiencies are different for pions and kaons of different charges and are usually not reproduced in simulation with sufficient accuracy. At SCTF a level of 10^{-3} for the systematic uncertainty seems achievable. For example, in the BaBar and Belle measurements of the asymmetries for the decays $D^0/\bar{D}^0 \rightarrow K^+K^-$, $\pi^+\pi^-$ [100, 101], the systematic uncertainty due to a difference in the detection efficiency for π^+ and π^- mesons used for D tagging was decreased to the 10^{-3} level. The thickness of material before and inside the tracking system of the SCTF detector should be minimized to reduce the systematic uncertainty for charge asymmetry measurements.

The CP asymmetry in decays of neutral D mesons can be represented as a sum of three terms. For example, for the decay into the CP eigenstate $\eta_f^{CP} = \pm 1$ [104]

$$\begin{aligned} A_f^{CP} &= a_f^d + a_f^m + a_f^i, \\ a_f^m &= -\eta_f^{CP} \frac{y}{2} (R_m - R_m^{-1}) \cos \varphi, \\ a_f^i &= \eta_f^{CP} \frac{x}{2} (R_m + R_m^{-1}) \sin \varphi, \end{aligned}$$

where a_f^d is a CP asymmetry in the decay, φ is a relative weak phase between the amplitudes for the decays $D^0 \rightarrow f$ and $\bar{D}^0 \rightarrow f$. The magnitude of the second term a_f^m is determined mainly by CP violation in mixing. The third term a_f^i is dominated by CP violation in the interference. The mixing leads to a difference in the time dependencies of the D^0 and \bar{D}^0 decay probabilities. This allows to localize and measure the contribution of the second and third terms. In experiments at B -factories [105, 106] the value

$$\delta Y = a_f^m + a_f^i = (-0.12 \pm 0.25) \times 10^{-2}$$

was obtained for the final states K^+K^- and $\pi^+\pi^-$. The formula given above is valid for incoherent production of D^0 and \bar{D}^0 mesons. At SCTF such an asymmetry will be studied for decays of D^0 mesons produced in the reaction $e^+e^- \rightarrow D^{*-}D^+ \rightarrow \pi^-D^0D^+$. For coherent $D^0\bar{D}^0$ production,

Table 1.10. The current values of the CP asymmetry measured in D^0 and D^+ meson decays. The designations f_{D^0} and f_{D^+} denote D^0 and D^+ meson final state, respectively.

f_{D^0}	A_{CP} (%)	f_{D^+}	A_{CP} (%)
		$\mu^+\bar{\nu}_\mu$	8 ± 8 [96]
$K^-\pi^+$	$+0.3 \pm 0.3 \pm 0.6$ [61]	$K^+\pi^0$	$-3.5 \pm 10.7 \pm 0.9$ [93]
$K_S^0\pi^0$	-0.20 ± 0.17 [88]	$K_S^0\pi^+$	-0.41 ± 0.09 [83]
$K_S^0\eta$	$+0.54 \pm 0.51 \pm 0.16$ [89]		
$K_S^0\eta'$	$+0.98 \pm 0.67 \pm 0.14$ [89]		
K^+K^-	-0.16 ± 0.12 [83]		
$K_S^0K_S^0$	$-2.9 \pm 5.2 \pm 2.2$ [90]	$K_S^0K^+$	-0.11 ± 0.25 [83]
		K^0K^+	$+0.11 \pm 0.17$ [83]
$\pi^+\pi^-$	$+0.00 \pm 0.15$ [83]	$\pi^+\pi^0$	$+2.9 \pm 2.9 \pm 0.3$ [93]
		$\pi^+\eta$	$+1.0 \pm 1.0$ [83]
		$\pi^+\eta'$	-0.5 ± 1.1 [83]
$\pi^0\pi^0$	-0.03 ± 0.64 [88]		
$K^-\pi^+\pi^0$	$+0.1 \pm 0.3 \pm 0.4$ [61]	$K^-\pi^+\pi^+$	-0.18 ± 0.16 [83]
$K^+\pi^-\pi^0$	-0.6 ± 5.3 [91]		
$K_S^0\pi^+\pi^-$	$-0.05 \pm 0.57 \pm 0.54$ [92]	$K_S^0\pi^+\pi^0$	$-0.1 \pm 0.7 \pm 0.2$ [61]
$K^+K^-\pi^0$	$-1.00 \pm 1.67 \pm 0.25$ [95]	$K^+K^-\pi^+$	$+0.32 \pm 0.31$ [83]
$\pi^+\pi^-\pi^0$	$+0.32 \pm 0.42$ [83]	$\pi^+\pi^-\pi^+$	-1.7 ± 4.2 [97]
$K^-\pi^+\pi^+\pi^-$	$+0.2 \pm 0.3 \pm 0.4$ [61]	$K^-\pi^+\pi^+\pi^0$	$-0.3 \pm 0.6 \pm 0.4$ [61]
$K^+\pi^-\pi^+\pi^-$	-1.8 ± 4.4 [98]	$K_S^0\pi^+\pi^+\pi^-$	$+0.0 \pm 1.2 \pm 0.3$ [61]
$K^+K^-\pi^+\pi^-$	$-8.2 \pm 5.6 \pm 4.7$ [99]	$K_S^0K^+\pi^+\pi^-$	$-4.2 \pm 6.4 \pm 2.2$ [99]

Table 1.11. The current values of the CP asymmetry measured in D_s meson decays. The designation f_{D_s} denotes D_s meson final state.

f_{D_s}	A_{CP} (%)
$\mu^+\bar{\nu}_\mu$	$+4.8 \pm 6.1$ [102]
$\pi^+\eta$	$+1.1 \pm 3.0 \pm 0.8$ [103]
$\pi^+\eta'$	$-2.2 \pm 2.2 \pm 0.6$ [103]
$K_S^0\pi^+$	$+3.11 \pm 1.54$ [83]
$K^0\pi^+$	$+0.38 \pm 0.48$ [83]
$K_S^0K^+$	$+0.08 \pm 0.26$ [83]
$K^+\pi^0$	$-26.6 \pm 23.8 \pm 0.9$ [93]
$K^+\eta$	$+9.3 \pm 15.2 \pm 0.9$ [93]
$K^+\eta'$	$+6.0 \pm 18.9 \pm 0.9$ [93]
$\pi^+\pi^+\pi^-$	$-0.7 \pm 3.0 \pm 0.6$ [103]
$\pi^+\pi^0\eta$	$-0.5 \pm 3.9 \pm 2.0$ [103]
$\pi^+\pi^0\eta'$	$-0.4 \pm 7.4 \pm 1.9$ [103]
$K_S^0K^+\pi^0$	$-1.6 \pm 6.0 \pm 1.1$ [103]
$K_S^0K_S^0\pi^+$	$+3.1 \pm 5.2 \pm 0.6$ [103]
$K^+\pi^+\pi^-$	$+4.5 \pm 4.8 \pm 0.6$ [103]
$K^+K^-\pi^+$	$-0.5 \pm 0.8 \pm 0.4$ [103]
$K_S^0K^-\pi^+\pi^+$	$+4.1 \pm 2.7 \pm 0.9$ [103]
$K_S^0K^+\pi^+\pi^-$	$-5.7 \pm 5.3 \pm 0.9$ [103]
$K^+K^-\pi^+\pi^0$	$+0.0 \pm 2.7 \pm 1.2$ [103]

the formula for A^{CP} is modified and becomes dependent on the decay used for tagging. This makes it possible to separate various contributions to the CP asymmetry without studying their time dependence. For example, the reaction $D^0\bar{D}^0 \rightarrow f_1 f_2$, where f_1 and f_2 are the states with the same CP parity, is forbidden at the $\psi(3770)$ resonance if CP is conserved. The probability of the decay is described by the following formula [107]:

$$\Gamma_{f_1 f_2} = \frac{1}{2R_m^2} [(2 + x^2 - y^2)|\lambda_{f_1} - \lambda_{f_2}|^2 + (x^2 + y^2)|1 - \lambda_{f_1}\lambda_{f_2}|^2] \Gamma_{f_1}\Gamma_{f_2}.$$

Since the terms corresponding to the contribution of mixing are proportional to the squares of x and y , the difference between direct CP violation for decays $D^0 \rightarrow f_1$ and $D^0 \rightarrow f_2$ is measured in this reaction.

At SCTF with 10^9 $D^0\bar{D}^0$ pairs the sensitivity level of 10^{-3} can be reached for the asymmetry difference between, for example, the K^+K^- and $\pi^+\pi^-$ final states. A similar measurement can be performed using the reaction $e^+e^- \rightarrow D^{*0}\bar{D}^0 \rightarrow \gamma D^0\bar{D}^0$. In this case the difference between CP asymmetries for states with opposite CP parities is measured.

Another example is a measurement of the asymmetry

$$A_{fl}^{CP} = \frac{\Gamma(l^- X, f) - \Gamma(l^+ X, f)}{\Gamma(l^- X, f) + \Gamma(l^+ X, f)}.$$

Here one D meson decays semileptonically, while the other to a CP eigenstate. Neglecting direct CP violation [108]

$$A_{fl}^{CP} = (1 + \eta)(a_f^m + a_f^i),$$

where η is the \mathcal{C} parity of the $D^0\bar{D}^0$ pair. It is seen that at $\eta = -1$, i.e., in $\psi(3770)$ decays, mixing does not contribute to the measured asymmetry, while for $\eta = 1$, i.e., in the reaction $e^+e^- \rightarrow D^{*0}\bar{D}^0 \rightarrow \gamma D^0\bar{D}^0$ the mixing contribution to the asymmetry is two times larger than that for D^0 mesons produced incoherently. Measurements performed in these two reactions allow to separate the contributions of direct and indirect mixing.

There are other powerful methods to search for CP violation. In Ref. [109] it is proposed to use the difference between the probabilities of decays of untagged D^0 mesons to the charge-conjugate states, for example, $K^-\pi^+$ and $K^+\pi^-$, to extract the parameter $\sin\varphi$. The Dalitz analysis of three-body decays allows to measure CP asymmetries for different resonant intermediate states (see, for example, the results of Ref. [110]). An interference between the CP -conserving and CP violating amplitudes in the Dalitz-plot distributions can increase the sensitivity of a search for CP violation. In the four-body decays, a search for CP violation can use T -odd moments [111] or triple products of momenta [112]. Using these methods at SCTF, one can measure the CP asymmetry in D decays with an accuracy of about 10^{-3} for both direct and indirect mechanisms of CP violation.

1.4.5 D and D_s meson rare decays

Rare decays of D and D_s mesons are a tool to search for new physics beyond the Standard Model. There are three types of decays of charmed mesons, suitable for this purpose:

1. flavor-changing neutral current (FCNC) decays via the weak neutral current, providing the transition between c and u quarks,
2. lepton-flavor-violating (LFV) decays,

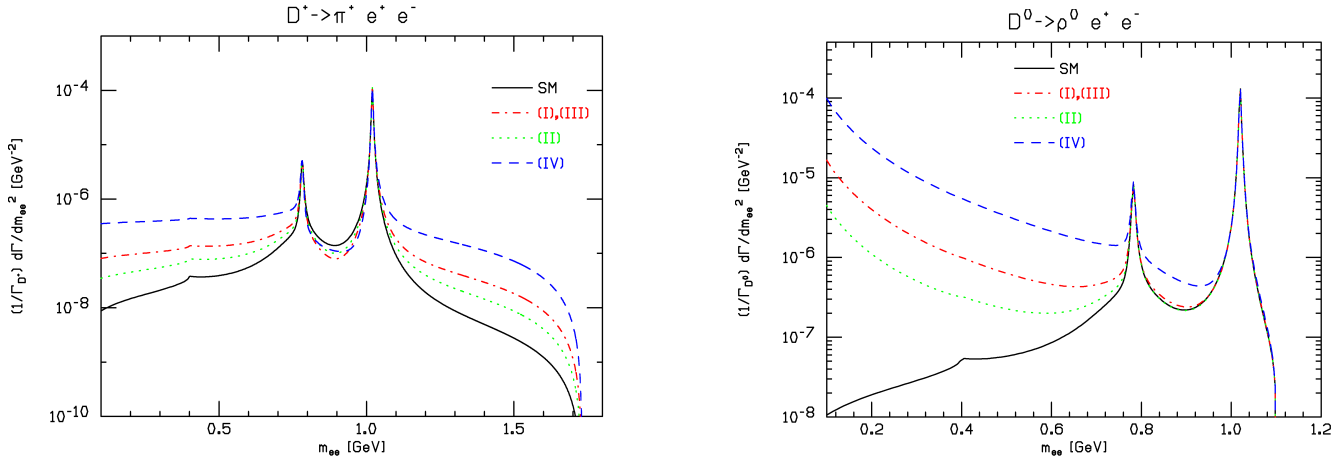


Figure 1.5. The spectra of the lepton-pair invariant mass for the decays $D^+ \rightarrow \pi^+ e^+ e^-$ (left) and $D^0 \rightarrow \rho^0 e^+ e^-$ (right). The solid curve represents the SM prediction, while the dashed curves indicate the MSSM predictions for different sets of model parameters.

3. lepton-number-violating (LV) decays.

Two latter types of decays are forbidden in the Standard Model. In SM decays via a $c \rightarrow u$ transition are described by loop diagrams and are strongly suppressed. For example, the probabilities for the $c \rightarrow ul^+l^-$ and $c \rightarrow u\gamma$ transitions are estimated to be of the order 10^{-8} . For specific exclusive $D_{(s)}$ decays, however, the contributions of large-distance dynamics should be taken into account. For example, the dominant contribution to the decay $D_{(s)}^+ \rightarrow \pi^+ l^+ l^-$ comes from the transition via the intermediate $\pi^+ \phi$ state followed by the decay $\phi \rightarrow l^+ l^-$. As a result, the $D_{(s)} \rightarrow X\gamma$ and $D_{(s)} \rightarrow Xl^+l^-$ branching fractions, where X is a hadronic state, increase up to 10^{-5} – 10^{-6} . For the D mesons, the three decays of these types are measured and have branching fractions consistent with the estimates in SM: $B(D^0 \rightarrow \phi\gamma) = (2.78 \pm 0.30 \pm 0.27) \times 10^{-5}$ [114], $B(D^+ \rightarrow \pi^+ \phi \rightarrow \pi^+ e^+ e^-) = (1.7_{-0.9}^{+1.4} \pm 0.1) \times 10^{-6}$ [115] и $B(D^+ \rightarrow \pi^+ \phi \rightarrow \pi^+ \mu^+ \mu^-) = (1.8 \pm 0.5 \pm 0.6) \times 10^{-6}$ [116]. In case of D_s meson the following branching fraction is measured: $B(D_s^+ \rightarrow \pi^+ \phi \rightarrow \pi^+ e^+ e^-) = ((0.6_{-0.4}^{+0.8} \pm 0.1) \times 10^{-5}$ [115].

Due to the large-distance contributions, which are difficult to calculate accurately in the framework of SM, decays like $D \rightarrow X\gamma$ become weakly sensitive to New Physics effects. But even for these decays, observables having some “New Physics” sensitivity can be found. For example, in Ref. [117] it is proposed to measure the difference $R = B(D^0 \rightarrow \rho^0 \gamma)/B(D^0 \rightarrow \omega \gamma) - 1$, which is estimated to be $(6 \pm 15)\%$ in SM. In the Minimal Supersymmetric Standard Model (MSSM), with some choice of model parameters the probability of the transition $c \rightarrow u\gamma$ can reach 6×10^{-6} and the value of R can be of the order 1 [117].

In decays $D_{(s)} \rightarrow Xl^+l^-$ one can analyze the spectrum of the lepton-pair invariant mass and select mass regions sensitive to the small-distance contributions. In Fig.1.5 taken from Ref. [118] the lepton invariant mass spectra are shown for the decays $D^+ \rightarrow \pi^+ e^+ e^-$ and $D^0 \rightarrow \rho^0 e^+ e^-$ in SM and MSSM. Restrictions on the MSSM parameters can be obtained with a sensitivity to the decay at the level of 10^{-6} . The predictions for decays $D \rightarrow Xl^+l^-$ obtained in different SM extensions can be found in Refs. [113, 118, 119].

Another type of decays with the $c \rightarrow u$ transition includes decays of a neutral D meson into the lepton or photon pair. SM predicts $B(D^0 \rightarrow \gamma\gamma) \simeq 3.5 \times 10^{-8}$ and $B(D^0 \rightarrow \mu^+ \mu^-) \sim 10^{-12}$ [118]. The $D^0 \rightarrow \mu^+ \mu^-$ branching fraction can reach 3.5×10^{-6} in supersymmetric models with R -parity violation. These models also give large values for the branching fractions of the following LFV decays: $B(D^0 \rightarrow \mu^+ e^-) < 10^{-6}$, $B(D^+ \rightarrow \pi^+ \mu^+ e^-) < 3 \times 10^{-5}$, $B(D^0 \rightarrow \rho^0 \mu^+ e^-) < 1.4 \times 10^{-5}$.

Table 1.12. The experimental upper limits on the rare D and D_s decays in units of 10^{-6} .

$D^0 \rightarrow \gamma\gamma$	2.2 [120]	$D^+ \rightarrow \pi^+ e^+ e^-$	1.1 [124]
$D^0 \rightarrow e^+ e^-$	0.079 [121]	$D^+ \rightarrow \pi^+ \mu^+ \mu^-$	0.073 [125]
$D^0 \rightarrow \mu^+ \mu^-$	0.006 [122]	$D^+ \rightarrow \pi^+ e^+ \mu^-$	2.9 [124]
$D^0 \rightarrow \mu^\pm + e^\mp$	0.26 [121]	$D^+ \rightarrow \rho^+ \mu^+ \mu^-$	560 [127]
$D^0 \rightarrow \pi^0 e^+ e^-$	45 [123]		
$D^0 \rightarrow \rho^0 e^+ e^-$	100 [123]	$D_s^+ \rightarrow K^+ e^+ e^-$	3.7 [124]
$D^0 \rightarrow \pi^0 e^\pm \mu^\mp$	86 [123]	$D_s^+ \rightarrow K^+ \mu^+ \mu^-$	21 [124]
$D^0 \rightarrow \rho^0 e^\pm \mu^\mp$	49 [123]	$D_s^+ \rightarrow K^+ e^+ \mu^-$	14 [124]

In Table 1.12 the current upper limits on the rare D and D_s decays are listed. At SCTF a sensitivity of 10^{-8} to rare D decays can be reached.

1.5 Charmed baryons

Charmed baryons (B_c), which can be produced at SCTF in the reaction $e^+e^- \rightarrow B_c\bar{B}_c$, consist of two light quarks (u, d, s) and a heavy c quark. A pair of light quarks forms two SU(3) flavor multiplets: the antisymmetric antitriplet and the symmetric sextet ($3 \times 3 = \bar{3}_A \oplus 6_S$). In S -wave low-lying baryons, the flavor symmetry and spin are related to each other: the total spin of light quarks is equal to 0 for the antitriplet and 1 for the sextet. In combination with the c quark, the antitriplet produces three states with spin 1/2 ($\Lambda_c^+, \Xi_c^+, \Xi_c^0$), while the sextet gives six states with spin 1/2 ($\Sigma_c^{+++,0}, \Xi_c^{\prime+}, \Xi_c^{\prime0}, \Omega_c^0$) and six states with spin 3/2 ($\Sigma_c^{*+++,0}, \Xi_c^{*+}, \Xi_c^{*0}, \Omega_c^{*0}$). All 15 S -wave charmed baryons have been observed. Their parameters are listed in Table 1.13.

Many excited charmed baryons are expected. In particular, the quark model predicts 63 P -wave states [128]. Sixteen of the excited states with masses in the range from 2.6 to 3.1 GeV have been observed [2, 129]. Other excited states of charmed baryons were reported recently by LHCb [130, 131] and Belle [132, 133].

In recent years physics of charmed baryons has been studied mainly at B -factories and at BESIII. In spite of the large number of produced charmed baryons (B factories produced about 10^7 Λ_c), their properties are rather poorly known. There is little or practically no experimental information about the quantum numbers of baryons and absolute branching fractions of their decays. For Λ_c^+ the situation was improved in 2013, when the first model-independent measurement of the absolute branching fraction of $\Lambda_c^+ \rightarrow pK^-\pi^+$ decay was performed by Belle [134] with fivefold improvement in precision over previous model-dependent determinations. This decay mode was used as the golden reference mode in previous measurements for the branching fractions of other Λ_c^+ decay modes. Later, BESIII measured branching fractions of twelve Cabibbo-favored hadronic decay modes of Λ_c^+ [135]. For $\Lambda_c^+ \rightarrow pK^-\pi^+$ decay mode their result is lower by two standard deviations compared to the Belle result [135, 136].

The potential of SCTF in study of charmed baryons depends strongly on the cross sections for the reactions $e^+e^- \rightarrow B_c\bar{B}_c$. For the reaction $e^+e^- \rightarrow \Lambda_c\bar{\Lambda}_c$ the cross section was measured by Belle [137]. The cross section is maximal at the energy about 4.65 GeV. The maximal value is

Table 1.13. The parameters of the S -wave charmed baryons [2].

	Structure	J^P	Mass, MeV	Width, MeV	Decay
Λ_c^+	udc	$(1/2)^+$	2286.46 ± 0.14	(200 ± 6) fs	weak
Ξ_c^+	usc	$(1/2)^+$	$2467.8_{-0.6}^{+0.4}$	(442 ± 26) fs	weak
Ξ_c^0	dsc	$(1/2)^+$	$2470.88_{-0.8}^{+0.34}$	112_{-10}^{+13} fs	weak
Σ_c^{++}	uuc	$(1/2)^+$	2454.02 ± 0.18	2.23 ± 0.30	$\Lambda_c^+ \pi^+$
Σ_c^+	udc	$(1/2)^+$	2452.9 ± 0.4	< 4.6	$\Lambda_c^+ \pi^0$
Σ_c^0	ddc	$(1/2)^+$	2453.76 ± 0.18	2.2 ± 0.4	$\Lambda_c^+ \pi^-$
$\Xi_c'^+$	usc	$(1/2)^+$	2575.6 ± 3.1	—	$\Xi_c^+ \gamma$
$\Xi_c'^0$	dsc	$(1/2)^+$	2577.9 ± 2.9	—	$\Xi_c^0 \gamma$
Ω_c^0	ssc	$(1/2)^+$	2695.2 ± 1.7	(69 ± 12) fs	weak
Σ_c^{*++}	uuc	$(3/2)^+$	2518.4 ± 0.6	14.9 ± 1.9	$\Lambda_c^+ \pi^+$
Σ_c^{*+}	udc	$(3/2)^+$	2517.5 ± 2.3	< 17	$\Lambda_c^+ \pi^0$
Σ_c^{*0}	ddc	$(3/2)^+$	2518.0 ± 0.5	16.1 ± 2.1	$\Lambda_c^+ \pi^-$
Ξ_c^{*+}	usc	$(3/2)^+$	$2645.9_{-0.6}^{+0.5}$	< 3.1	$\Xi_c \pi$
Ξ_c^{*0}	dsc	$(3/2)^+$	2645.9 ± 0.5	< 5.5	$\Xi_c \pi$
Ω_c^{*0}	ssc	$(3/2)^+$	2765.9 ± 2.0	—	$\Omega_c^0 \gamma$

about 0.5 nb. Such a large cross section value can be explained by a presence of a new resonance state $Y(4630)$ near the $\Lambda_c \bar{\Lambda}_c$ threshold with mass $M = 4634 \pm 10$ MeV and width $\Gamma = 92 \pm 40$ MeV [137]. Another resonance $Y(4660)$ with mass $M = (4665 \pm 10)$ MeV and width $\Gamma = (53 \pm 16)$ MeV compatible within errors with those of $Y(4630)$ was observed in the invariant mass spectrum of $\psi(2S)\pi^+\pi^-$ in the Belle and BaBar experiments by initial state radiation technique in the e^+e^- annihilation [138]. At present it is not clear if $Y(4630)$ and $Y(4660)$ are different states, or manifestations of the same state, and their inner structures became a subject of hot discussions [138, 139, 140, 141]. If $Y(4630)$ is a $\Lambda_c \bar{\Lambda}_c$ -baryonium state, a small admixture of the $\psi(2S)f_0(980)$ molecular component can be associated with the $Y(4660)$ signal. Less exotic assignment of $Y(4630)$ as a 5^3S_1 charmonium state was also considered. However, it seems its interpretation as a tetraquark state is more favorable [138, 139, 140, 141].

With an integrated luminosity of 200 fb^{-1} SCTF will produce 10^8 $\Lambda_c \bar{\Lambda}_c$ pairs. This will allow to perform a detailed study of Λ_c properties with the use of the double-tag method. For other charmed baryons the experimental data on the reactions $e^+e^- \rightarrow B_c \bar{B}_c$ are absent. Without a resonance enhancement the expected cross section does not exceed 10 pb. The physics program for baryons depends on the maximum energy of charm-tau factory. Detailed studies of weak decays of the charmed baryons $\Lambda_c^+(2286)$, $\Xi_c^+(2468)$, $\Xi_c^0(2471)$, and $\Omega_c^0(2695)$ seem feasible. The required maximum energies of the factory are 4.7, 5.1 and 5.5 GeV, respectively.

A large expected number (10^8) of $\Lambda_c \bar{\Lambda}_c$ pairs makes it possible to undertake a search of CP violation in Λ_c decays. Although CP violation is well established in K and B meson decays, until

very recently no CP violating signal was seen in the baryonic sector.

The Hyper CP experiment had searched for CP violation signal in strange baryon decays by a 800 GeV proton beam on a Cu target and get for the corresponding CP asymmetry parameter $A_{\Lambda\Sigma} = (0.0 \pm 5.1 \pm 4.4) \cdot 10^{-4}$, which should be compared to the Standard Model predictions $A(\Lambda \rightarrow p\pi^-) \sim (0.05 - 1.2) \cdot 10^{-4}$ and $A(\Sigma^- \rightarrow \lambda\pi^-) \sim (0.2 - 3.5) \cdot 10^{-4}$ [142]. The first 3.3-standard-deviation evidence for CP violation in the four-body hadronic decay $\Lambda_b^0 \rightarrow p\pi^-\pi^+\pi^-$ was found quite recently in the LHCb experiment [143].

Let us briefly discuss CP asymmetry observables on the example of $\Lambda \rightarrow p\pi^-$ decay. In the Λ rest frame, the final state pion-nucleon system can be either in the S -wave, or in the P -wave. Denoting the corresponding parity non-conserving and parity-conserving amplitudes as S and P , we get for the angular distribution of the produced proton [144]

$$\frac{d\Gamma}{d\Omega} \sim 1 + \gamma \vec{\sigma}_i \cdot \vec{\sigma}_f + (1 - \gamma) (\vec{n}_f \cdot \vec{\sigma}_i)(\vec{n}_f \cdot \vec{\sigma}_f) + \alpha \vec{n}_f \cdot (\vec{\sigma}_i + \vec{\sigma}_f) + \beta \vec{n}_f \cdot (\vec{\sigma}_f \times \vec{\sigma}_i), \quad (1.7)$$

where $\vec{\sigma}_i$ and $\vec{\sigma}_f$ are unit vectors in the direction of the initial and final baryon spins, \vec{n}_f is the unit vector along the final baryon momentum, and

$$\alpha = \frac{2\text{Re}(S^*P)}{|S|^2 + |P|^2}, \quad \alpha = \frac{2\text{Im}(S^*P)}{|S|^2 + |P|^2}, \quad \gamma = \frac{|S|^2 - |P|^2}{|S|^2 + |P|^2} = \sqrt{1 - \alpha^2 - \beta^2}. \quad (1.8)$$

Under CP transformation $\vec{n}_f \rightarrow -\vec{n}_f$, $\vec{\sigma}_{i,f} \rightarrow \vec{\sigma}_{i,f}$ and therefore CP symmetry requires $\alpha = -\bar{\alpha}$ and $\beta = -\bar{\beta}$, suggesting to define CP asymmetry parameters as follows

$$A = \frac{\alpha + \bar{\alpha}}{\alpha - \bar{\alpha}}, \quad B = \frac{\beta + \bar{\beta}}{\beta - \bar{\beta}}, \quad \Delta = \frac{\Gamma(\Lambda \rightarrow p\pi^-) - \Gamma(\bar{\Lambda} \rightarrow \bar{p}\pi^+)}{\Gamma(\Lambda \rightarrow p\pi^-) + \Gamma(\bar{\Lambda} \rightarrow \bar{p}\pi^+)}. \quad (1.9)$$

Here $\bar{\alpha}$ and $\bar{\beta}$ are angular distribution parameters in the anti- Λ decay $\bar{\Lambda} \rightarrow \bar{p}\pi^+$. Experiments usually measure the parameter α , which controls the decay asymmetry in the angular distribution if the final proton polarization is not measured.

Similar parameters can be defined for the $\Lambda_c^+ \rightarrow \Lambda\pi^+$ decay and the FOCUS(E831) experiment at Fermilab in 2005 provided the first measurement of the CP asymmetry parameter $A = -0.07 \pm 0.19 \pm 0.24$ which is consistent with zero albeit with large errors [145]. A Monte Carlo estimation shows that, with an integrated luminosity of 200 fb $^{-1}$, charm-tau factory can reach the precision of about 0.3% in this parameter [144].

Under assumption that $\Lambda_c^+ \rightarrow \Lambda\pi^+$ decay is dominated by the $\Delta I = 1/2$ transition, S - and P -wave amplitudes will contain only one strong δ and only one weak ϕ phases: $S = |S|e^{i(\delta_S + \phi_S)}$, $P = |P|e^{i(\delta_P + \phi_P)}$. Then

$$\alpha = \frac{2|S||P|}{|S|^2 + |P|^2} \cos(\delta_P - \delta_S + \phi_P - \phi_S), \quad \beta = \frac{2|S||P|}{|S|^2 + |P|^2} \sin(\delta_P - \delta_S + \phi_P - \phi_S), \quad (1.10)$$

and

$$\bar{\alpha} = \frac{-2|S||P|}{|S|^2 + |P|^2} \cos(\delta_P - \delta_S - \phi_P + \phi_S), \quad \bar{\beta} = \frac{-2|S||P|}{|S|^2 + |P|^2} \sin(\delta_P - \delta_S - \phi_P + \phi_S), \quad (1.11)$$

because for CP -conjugated decay $\Lambda_c^- \rightarrow \bar{\Lambda}\pi^-$ strong phases, which arise from the final-state interactions, are the same (Fermi-Watson theorem), while the remaining part of wave functions undergo complex conjugation and thus weak phases change sign. Overall minus sign appears because of the odd-parity of pions and $(-1)^l$ parity of spatial part of the wave function which means

that S -wave amplitude acquires an additional minus sign under CP , while P -wave amplitude does not.

In this approximation [146]

$$A = \frac{\alpha + \bar{\alpha}}{\alpha - \bar{\alpha}} = \tan(\delta_S - \delta_P) \tan(\phi_S - \phi_P), \quad B = \frac{\beta + \bar{\beta}}{\beta - \bar{\beta}} = \frac{\tan(\phi_S - \phi_P)}{\tan(\delta_S - \delta_P)}. \quad (1.12)$$

Therefore, even in the case of significant CP violation in weak interactions, A -asymmetry can still be very small if the strong phase difference between the two amplitudes is small. On the contrary, B -type asymmetries can be large even with small strong phases. As is evident from (1.7), B -type asymmetries are related to the triple product $\vec{n}_f \cdot (\vec{\sigma}_f \times \vec{\sigma}_i)$. Prospects of the charm-tau factory in studying such triple product asymmetries (proportional to $\beta + \bar{\beta} \sim \cos(\delta_S - \delta_P)$) were examined in Ref. [147] with the conclusion that the precision can reach the level of 10^{-3} .

A unique feature of SCTF is a possible presence of the longitudinal polarization in the electron beam. We think this feature will help to investigate and reduce the systematic errors related to various detector asymmetries.

Within the Standard Model CP violation in the charm sector is tiny, which makes this sector an excellent place to search for a new physics beyond the Standard Model. Charmed baryon decays seem very promising in this respect.

1.6 τ lepton physics

At SCTF τ leptons are produced in the process $e^+e^- \rightarrow \tau^+\tau^-$. Its cross section grows rapidly from about 0.1 nb near the threshold of the $\tau^+\tau^-$ production ($2E = 3.55$ GeV) up to 3.6 nb at the top of the $\psi(2S)$ resonance (taking into account the expected beam energy spread). Near the threshold of $D\bar{D}$ production ($2E \approx 3.7$ GeV) it is about 2.9 nb, and reaches 3.5 nb at the $2E = 4.25$ GeV. During the SCTF operation, about 2.1×10^{10} $\tau^+\tau^-$ pairs will be produced, an order of magnitude larger than at the B factories, but smaller than expected at the Belle II experiment (about 4.6×10^{10}).

One should note that the current accuracy of many τ -lepton parameters, e.g., its leptonic and hadronic decay widths, is limited by systematic effects. For precise measurements of the branching fractions and hadronic spectral functions, a dedicated run near the $e^+e^- \rightarrow \tau^+\tau^-$ threshold is planned. At the threshold τ leptons are produced at rest allowing to suppress background by applying an additional condition on kinematics of hadronic decays: $2m_\tau E_{had} = m_\tau^2 + m_{had}^2$, where E_{had} and m_{had} are the energy and invariant mass of the hadronic system, and m_τ is the τ -lepton mass. Use of this condition allows to select τ events with the tagging method. The remaining background can be measured running below threshold of τ lepton production. With an integrated luminosity of 1 ab^{-1} collected near the $\tau^+\tau^-$ production threshold about 10^8 τ -lepton pairs will be produced.

Branching fractions and spectral functions of the hadronic τ decays can be used to determine the strong coupling constant α_s [148] (see also Ref. [149]). Data on hadronic decays with $\Delta S = 1$ are also used to determine the s -quark mass m_s and the CKM matrix element V_{us} [150]. Potentially τ -lepton decays are the most powerful tool for precise measurements of α_s , m_s and V_{us} .

A high-precision measurement of the branching fractions of leptonic decays as well as the decays $\tau^+ \rightarrow \pi^+\nu$ and $\tau^+ \rightarrow K^+\nu$ will result in a significant improvement of lepton-universality tests in interactions of W -boson with charged lepton current. The review of the current status of such tests in τ decays at B -factories can be found in Ref. [151].

For precision tests of SM and lepton universality, knowledge of the τ lepton mass is mandatory. The most precise method of τ lepton mass determination is a measurement of the energy dependence of the $e^+e^- \rightarrow \tau^+\tau^-$ cross section near threshold. Such measurements require high-precision energy calibration of the collider using methods of resonant depolarization or Compton backscattering.

An important test of the SM is a study of the Lorentz structure of the amplitudes of the leptonic $\tau \rightarrow \ell\nu\nu$, radiative leptonic $\tau \rightarrow \ell\nu\nu\gamma$, and five-lepton $\tau \rightarrow \ell\ell'^+\ell'^-\nu\nu$ ($\ell, \ell' = e, \mu$) τ decays. Thus, lepton energy spectrum in the $\tau \rightarrow \ell\nu\nu$ decay depends linearly on four Michel parameters (ρ, η, ξ and δ) [152]. They are experimentally accessible bilinear combinations of the generalized weak coupling constants, and in the Standard Model get values: $\rho = 3/4, \eta = 0, \xi = 1,$ and $\delta = 3/4$. For measurement of the parameters ξ and δ , knowledge of τ -lepton polarization is required. In experiments at e^+e^- colliders with unpolarized beams, the average polarization of a single τ is zero. However, spin-spin correlations between the τ^+ and τ^- produced in the reaction $e^+e^- \rightarrow \tau^+\tau^-$ can be exploited to measure ξ and δ parameters. Events where both τ leptons decay to the selected final states are analyzed: one τ lepton decays to the signal mode, while the opposite τ decays to the $\pi\pi^0\nu$ mode, which has the largest branching fraction and properly studied dynamics. Thus, the total differential cross section of the reaction $e^+e^- \rightarrow (\tau \rightarrow \ell\nu\nu, \tau \rightarrow \pi\pi^0\nu)$ linearly depends on all four Michel parameters. A longitudinal polarization of initial beams at SCTF (in this case the average polarization of a single τ is nonzero) would allow a more efficient usage of the collected data samples and minimize systematic uncertainties of polarization-dependent parameters.

Data samples collected at the $\tau^+\tau^-$ production threshold allow one to suppress the impact of the radiative corrections (to the $e^+e^- \rightarrow \tau^+\tau^-$ process) on the lepton energy spectrum and decrease the associated systematic uncertainty.

LFV decays of τ lepton, such as $\tau \rightarrow \ell\gamma, \tau \rightarrow \ell\ell\ell^{(\prime)}$ or $\tau \rightarrow \ell h$, where ℓ, ℓ' are electron or muon, and h is a hadronic system, are sensitive to effects of New Physics. Different models beyond the SM predict branching fractions of these decays at the level of 10^{-7} – 10^{-10} (see, for example, Ref. [153]). Experimental upper limits on the branching ratios of LFV decays achieved at the B factories are in the range from 10^{-7} to 2×10^{-8} [2] and already constrain the parameter space of some models. For most of the decays, a much higher sensitivity is expected in future experiments at superKEKB. For some decays an upper limit on the decay probability is determined by background. This is, in particular, true for the $\tau \rightarrow \mu\gamma$ decay, which is very important in a search for New Physics. At B factories the upper limit on the probability of this decay is determined by the background from the process $e^+e^- \rightarrow \tau^+\tau^-\gamma$. At the SCTF this background is negligible [154]. Hence, in spite of less statistics, the sensitivity to the $\tau \rightarrow \mu\gamma$ decay at SCTF (below 10^{-9}) will be better than at superKEKB [155].

CP violation (CPV) in the quark sector does not explain the observed baryon asymmetry of the Universe. Therefore, it is reasonable to search for CPV in the lepton sector, in particular, in τ decays. CP violation can be observed in hadronic τ decays, provided that there are two interfering amplitudes with different strong and weak phases. Under CP transformation, the $e^{i\delta_w+i\delta_s}$ is transformed into $e^{-i\delta_w+i\delta_s}$, where δ_w and δ_s are relative strong and weak phases of two amplitudes. This results, for example, in the non-equality of the widths of the CP -conjugate decays. The asymmetry $A_{CP} = (\Gamma(\tau^+ \rightarrow f^+\nu) - \Gamma(\tau^- \rightarrow f^-\nu))/(\Gamma(\tau^+ \rightarrow f^+\nu) + \Gamma(\tau^- \rightarrow f^-\nu))$ is proportional to the $\sin\delta_s \sin\delta_w$. In the SM, τ lepton decays are described by a single amplitude with a W -boson exchange. Therefore, observation of the CPV would be an explicit indication of the physics beyond SM. The only exception is $\tau \rightarrow K_{S(L)}^0\pi\nu$ decay, in which the CP asymmetry at the level of 3×10^{-3} [156] arises in the SM because of the CPV in the neutral kaons. Suggestions for using various decays to search for CPV are considered in Refs. [157, 158, 159, 160, 161, 162]. The most promising decays are $\tau^\pm \rightarrow K^\pm\pi^0\nu, \tau^\pm \rightarrow K_S^0\pi^\pm\nu, \tau^\pm \rightarrow K_S^0\pi^\pm\pi^0\nu, \tau \rightarrow \rho\pi\nu, \tau \rightarrow \omega\pi\nu,$

$\tau \rightarrow a_1 \pi \nu$. In addition to measuring the asymmetry in the decay width, A_{CP} defined above, it is also suggested to use a so called modified asymmetry, when experimental differential distributions of the final hadrons are integrated with a specially selected kernel over a limited region of the phase space, and an asymmetry in the triple product $\boldsymbol{\sigma} \cdot (\mathbf{p}_1 \times \mathbf{p}_2)$, where $\boldsymbol{\sigma}$, \mathbf{p}_1 , \mathbf{p}_2 are a τ polarization vector and momenta of two final hadrons, respectively. It is worth noting that the asymmetry in the triple product is proportional to the $\cos \delta_s \sin \delta_w$, i.e., a nonzero difference of the strong phases is not needed for its observation.

A search for CP violation was performed in the CLEO experiment using 10^7 τ -lepton pairs for $\tau^\pm \rightarrow \pi^\pm \pi^0 \nu$ [163] and $\tau^\pm \rightarrow K_S \pi^\pm \nu$ [164] decays. The inclusive decay-rate asymmetry $A_{CP} = \frac{\Gamma(\tau^+ \rightarrow \pi^+ K_S(\geq 0\pi^0)\nu) - \Gamma(\tau^- \rightarrow \pi^- K_S(\geq 0\pi^0)\nu)}{\Gamma(\tau^+ \rightarrow \pi^+ K_S(\geq 0\pi^0)\nu) + \Gamma(\tau^- \rightarrow \pi^- K_S(\geq 0\pi^0)\nu)}$ was measured with the data sample of 4.4×10^8 $\tau^+ \tau^-$ pairs at BABAR [165]. The modified asymmetry in the $\tau^- \rightarrow K_S^0 \pi^- \nu$ decay was investigated with the statistics of 6.4×10^8 τ pairs at Belle [166] as a function of the $K_S^0 \pi^-$ invariant mass. The obtained result $A_{CP} = (-0.36 \pm 0.23 \pm 0.11)\%$ is about 2.8 standard deviations from the SM expectation $A_{CP}^{K^0} = (+0.36 \pm 0.01)\%$, while the modified asymmetry in the $\tau^- \rightarrow K_S^0 \pi^- \nu$ decay agree well with no CPV in the whole range of the $K_S^0 \pi^-$ invariant masses. Simultaneous analysis of the $\tau^- \rightarrow K_S^0 \pi^- \nu$ and $\tau^- \rightarrow K_S^0 \pi^- \pi^0 \nu$ decays allows one to study the dynamics of the $K\pi$ -system production in more detail and search for CPV on the new level of precision.

One can expect an increase of the sensitivity after analysis of data accumulated at Belle II and SCTF. The longitudinal polarization of the initial beams at the CTF results in the nonzero average polarization of single τ . This opens possibilities to study various effects (CPV, Michel parameters) and search for New Physics in the spin-dependent part of the τ decay width without reconstruction of the second τ lepton in the $e^+ e^- \rightarrow \tau^+ \tau^-$ event. Besides the increase in the sensitivity to the spin-dependent effects in τ decays, this allows one to decrease associated systematic uncertainties.

1.7 Measurement of $e^+ e^- \rightarrow$ hadrons below 5 GeV

A measurement of the total cross section of $e^+ e^-$ annihilation into hadrons is usually referred to as an R measurement, where R is the ratio of the Born cross section for $e^+ e^- \rightarrow$ адроны to the Born cross section for $e^+ e^- \rightarrow \mu^+ \mu^-$:

$$R = \frac{\sigma^{(0)}(e^+ e^- \rightarrow \text{hadrons})}{\sigma^{(0)}(e^+ e^- \rightarrow \mu^+ \mu^-)}. \quad (1.13)$$

Measurements of R can be utilized to test perturbative QCD and measure α_s [167]. QCD sum rules provide a method of extracting from the values of R such important parameters as quark masses, quark and gluon condensates and the value of Λ_{QCD} [168]. Through dispersion relations R measurements give an input to the calculations of the hadronic corrections to various fundamental quantities: the anomalous magnetic moment of the muon $a_\mu = (g_\mu - 2)/2$ [169], the running fine structure constant $\alpha(s)$ [170], superfine splitting in muonium [171] etc. Depending on the problem, different energy ranges are of importance. For example, for $(g_\mu - 2)/2$ the low energy range up to 2 GeV gives about 93% of the whole leading-order hadronic contribution. However, the region from 2 to 5 GeV also gives a non-negligible contribution, which is about 6%. For $\alpha_{\text{QED}}(M_Z^2)$, the corresponding contributions are about equal, 21.0% and 17.1%, respectively (about 45% comes from energies > 11 GeV, where pQCD can be used with suitable precision). The total leading-order hadronic contributions are calculated to be $a_\mu^{\text{had LO}} = (694.91 \pm 4.3) \times 10^{-10}$ and $\Delta\alpha_{\text{QED}}^5(M_Z^2) = (276.26 \pm 1.38) \times 10^{-4}$ [172]. New experiments on a measurement of the muon anomalous magnetic moment in FermiLab [173] and J-PARC [174] plan to improve accuracy of the experimental a_μ value by a factor of at least 4, up to $\sim 1.5 \times 10^{-10}$. Precise tests of electroweak

theory in experiments at future colliders such as ILC, CLIC, FCC-ee will require knowledge of the hadronic contribution to $\alpha_{QED}(M_Z^2)$ at the level of $\sim 0.5 \div 0.3 \times 10^{-4}$ [175, 176]. To provide comparable accuracies in the theoretical predictions, the accuracy of integral R measurement must be $\sim 0.2\%$.

The c.m. energy range from 2 to 5 GeV is almost asymptotic for u -, d -, and s -quarks. There are no resonances made of light quarks at these energies. The energy dependence of R is very slow from 2 GeV up to threshold of D -meson production (3.73 GeV), except for narrow regions around the J/ψ and $\psi(2S)$ resonances. Its value $R \approx 2.2$ is consistent with the pQCD prediction [177]. The energy region 3.73–5.0 GeV is the resonant region for c -quark; it contains several wide $c\bar{c}$ resonances decaying into D mesons. Numerous R measurements exist in the energy range between 2 and 5 GeV: by Crystal Ball [178], PLUTO [179], DASP [180], Mark-I [181, 182], BES [183, 184, 185, 186], KEDR [187, 188]. In general, the measurements of different experimental groups are consistent. The most detailed measurement was performed by BESII at 165 energy points from 2 to 5 GeV with average systematic uncertainty ranged from 7% to 3.3%. The BESIII result is expected soon: the energy scan (125 points with the total integrated luminosity 1.3 fb^{-1}) of the energy region 2.00–4.59 GeV was performed in 2012–2015. Currently the best systematic accuracy, about 2%, was reached in the KEDR experiment, which measures R at 20 energy points between 1.84 and 3.72 GeV (Fig. 1.6). However, this accuracy is insufficient for high-precision tests of the Standard Model, which require knowledge of the cross section to at least 1%. To reach such accuracy, we need a detailed scan with a few-MeV step and integrated luminosity of 10 pb^{-1} per point or about 10 fb^{-1} in total in the whole energy range.

Below 2 GeV the total cross section can be measured with a sub-percent accuracy using the radiative return method. This method was used in the KLOE [190], BABAR [191], and BESIII [192] experiments. Since the number of possible hadronic final states in this energy range is relatively small, the total cross section can be determined as a sum of cross sections for various exclusive channels. The most comprehensive analysis on the measurement of various hadronic channels below 2 GeV was performed in the BABAR experiment. Statistically close results can be achieved in the BESIII experiment. The Belle II experiment at the SuperKEKB collider, which is under commissioning now, will collect a data sample by two orders of magnitude larger than that collected at BABAR. The design SCTF luminosity provides statistics comparable with Belle II near the $\pi^+\pi^-$ threshold and several times larger at $\sqrt{M^2} \sim 2$ GeV. It should be noted that it is challenging to reach systematic uncertainty on R of about 0.2% in a single experiment. To reach such an accuracy in the world-average value, several systematically independent R measurement should be performed. The radiative-return measurements at SCTF and SuperKEKB are complementary. They will be performed at significantly different c.m. energies and, therefore, have different sources of systematic uncertainties.

The obtained information on exclusive channels of e^+e^- annihilation to hadrons allow also to investigate mechanisms of light quark hadronization at low energies, perform searches for possible exotic states like tetraquarks, hybrids, and glueballs, and study the ρ , ω , and ϕ excitations.

After discovery 40 years ago of the family of broad charmonia above open charm threshold, in the next 30 years the properties of these resonances were determined on the measurements of the total hadronic cross-section at DASP [180] and Mark-I [181]. Some progress was achieved after fits to the Crystal Ball [178] and BES [183, 184] data in Refs. [193, 194]. In Ref. [194] the first attempt to include interference between exclusive decays of ψ -resonances was performed, but the relations between different decay modes were accounted using a model prediction. A real breakthrough happened recently, after appearance of exclusive cross-section measurements for final states with D , D^* , D_s , and D_s^* mesons. These measurements were performed by the Belle and BABAR collaborations in the energy range from 3 to 5 GeV (see the complete bibliography in Ref. [195])

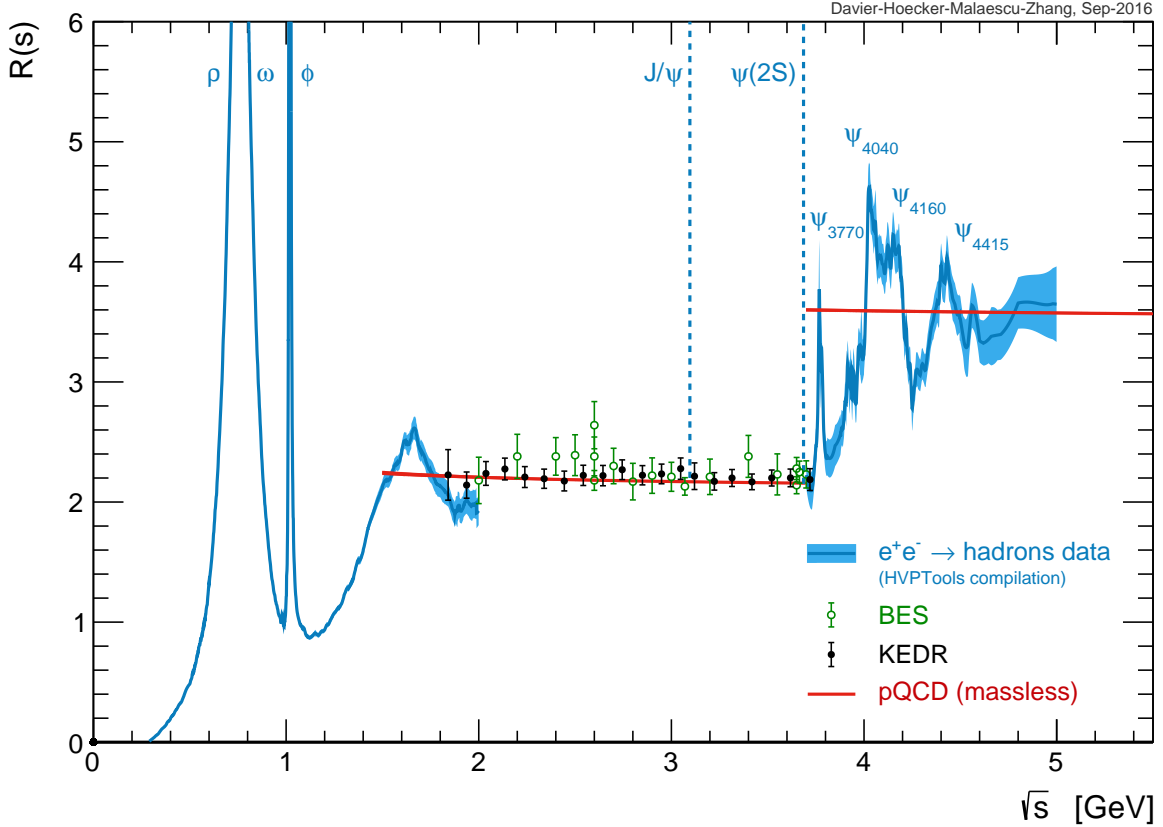


Figure 1.6. The energy dependence of $R = \sigma(e^+e^- \rightarrow \text{hadrons})/\sigma(e^+e^- \rightarrow \mu^+\mu^-)$ [189]. The points are the BESII and KEDR inclusive data. The shaded areas are a sum of exclusive cross sections at $\sqrt{s} < 2$ GeV and average of all R measurements above $\psi(2S)$.

using the radiative return method, and by CLEO [62] in the range from 3.77 to 4.26 GeV using a direct c.m. energy scan. An important conclusion is that the sum of exclusive cross sections for the final states containing various D mesons saturates the total cross section of $c\bar{c}$ production. The latter is obtained from the inclusive BESII R measurement [196] by subtracting the calculated light-quarks contribution (see Fig. 1.7).

After appearance of the exclusive measurements, numerous attempts were performed to describe the energy behavior of exclusive cross sections of D meson production. For example, in Ref. [197] Belle data on different open-charm channels in the energy range 3.7–4.7 GeV are analysed simultaneously using a unitary approach based on a coupled-channel model. Nevertheless, the situation with the spectroscopy of broad charmonia remains largely uncertain. More accurate measurements of exclusive cross sections in the energy range from 3.7 to 5 GeV, as well as improved methods for theoretical interpretation of the results obtained are required to determine parameters of the resonances of the ψ family and the probabilities of their decays.

It is important to note that for various applications, e.g., for determination of quark masses, it is necessary to know the component of R coming from specific quark flavor, particularly in the energy range near the quark production threshold. Experimentally, this is a rather complicated problem. A phenomenological approach to this problem is described in Ref. [198] devoted, in particular, to c -quark mass determination. For the energy range above 3.73 GeV the authors employ the complete set of available R data. To obtain the charm component, they use extrapolation from the fit to R data below $D\bar{D}$ threshold, and apply non-trivial correction for production of secondary

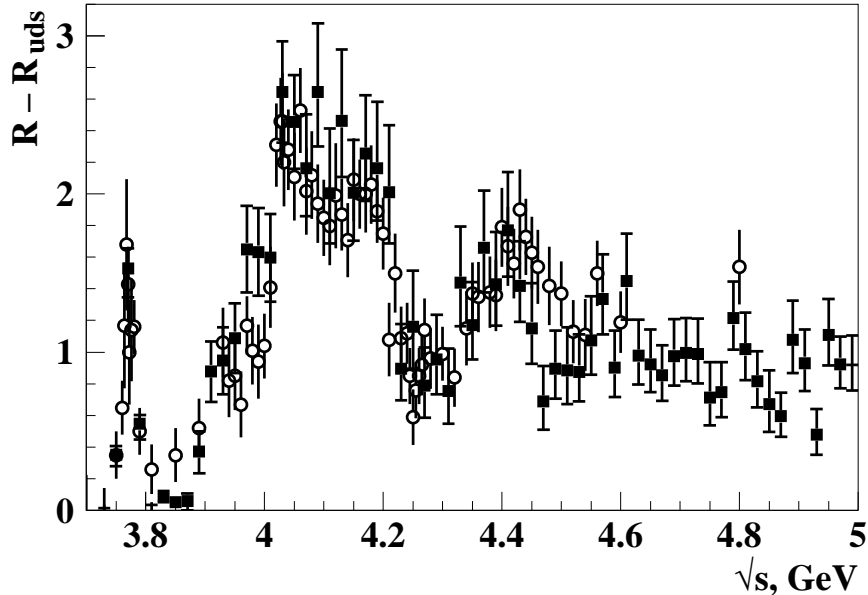


Figure 1.7. Comparison of the inclusive measurement of $R - R_{uds} \equiv R_{cc} = \sigma(e^+e^- \rightarrow c\bar{c})/\sigma(e^+e^- \rightarrow \mu^+\mu^-)$ ($R_{uds} = 2.121 \pm 0.023 \pm 0.083$), performed by BESII (open circles) with a sum of exclusive channels measured in the Belle experiment (solid squares).

$c\bar{c}$ pairs in e^+e^- annihilation into light quarks. To estimate the error on R_{cc} in this method, a sophisticated analysis of experimental uncertainties is needed. Another possibility to obtain R_{cc} is to measure all exclusive final states containing particles with c quark. As discussed above, at the current level of statistical accuracy R_{cc} is saturated by the contributions from the $D^{(*)}\bar{D}^{(*)}$ and $D_s^{(*)}\bar{D}_s^{(*)}$ final states. It is clear that improving accuracy will require the addition of new exclusive channels and a huge integrated luminosity. Substantial progress in the charmonium energy range can be expected in the future experiments, first of all, direct scans at SCTF.

Besides that, running at the threshold of a baryon-antibaryon pair production ($p\bar{p}$, $n\bar{n}$, $\Lambda\bar{\Lambda}$, ...) in a polarized mode of SCTF will allow to study of the baryon form factors near threshold, including a unique chance of doing that for polarized baryons [199]. It is particularly interesting for the Λ -hyperon production, where a final-particle polarization can be determined from the angular distribution in the $\Lambda \rightarrow p\pi^-$ decay.

1.8 Two-photon physics

Today two-photon physics is an important sector of particle physics. In principle, it is physics for photon colliders extensively discussed now but looks like a matter of a distant future. However, e^+e^- colliders as a source of two-photon collisions have an important advantage, one or both virtual colliding photons may be strongly off-shell. This provides additional possibilities compared to the collisions of real photons. Data on the photon-meson transition form factors of resonances (π^0 , η , η' ...) obtained at large momentum transfers $|Q^2| > 4 \text{ GeV}^2$ can be used to test the perturbative QCD calculations. However, of largest interest are data on smaller momentum transfer $|Q^2| < 1.5 \text{ GeV}^2$ (see Ref. [200] and references therein), which can be employed for testing of the form-factor models needed for calculation of the light-by-light contribution to the anomalous magnetic moment of the muon.

Physical tasks of SCTF first of all include a study of C -even resonances, both from light quarks and charmonium states, with quantum numbers $J^{PC} = 0^{++}, 0^{-+}, 2^{-+}, 2^{++}$. When one of the photons is off-shell, particles with $J = 1$ can also be produced, including those with exotic quantum numbers $J^{PC} = 1^{-+}$. High luminosity of SCTF will allow not only a determination of the two-photon widths of the resonances, but also a study of their rare decay modes. A separate problem also requiring high luminosity is a measurement of transition form factors for the vertexes $\gamma^* \rightarrow \gamma M$ and $\gamma^* \rightarrow \gamma^* M$, where M is a C -even resonance.

Note also the importance of measuring the total cross sections of $\gamma\gamma \rightarrow$ hadrons as well as the cross sections for separate channels like $\gamma\gamma \rightarrow M(M')$, where M and M' are mesons ($\pi, K, \eta, \rho, \omega, \phi \dots$) or baryons, starting from the reactions thresholds. For the above mentioned calculation of the light-by-light contribution to the anomalous magnetic moment of the muon, it is of special interest to measure the Q^2 dependence of the pion pair production cross sections.

In such studies, a high hermeticity of the detector is required to suppress background from e^+e^- annihilation into hadrons. The important additional instrument could be a low-angle tagger (similar to that in the KLOE II experiment) to detect scattered electrons. Design of the tagger strongly depends on configuration of the collider final focus system and requires special studies.

1.9 Conclusions

An important difference of SCTF compared to the B factories at SLAC and KEK and the ϕ factory at Frascati is its ability to run in the broad energy range whereas the colliders mentioned above run basically at a single c.m. energy. This complicates the experimental facilities, both a collider and a detector, but of course makes much broader a physical program.

And one more rather general conclusion. In the discussed energy range a predictive power of the existing theory is rather limited. Our recent experience shows that some particles, e.g., $Y(4260)$ or $X(2150)$, were discovered accidentally and their interpretation is still unclear. Therefore, an experimental study is still most important and one can hope that SCTF will help to solve many of the existing problems.

Bibliography

- [1] N. Brambilla *et al.* [Quarkonium Working Group], arXiv:hep-ph/0412158; N. Brambilla *et al.* [Quarkonium Working Group], arXiv:1010.5827; G.V. Pakhlova, P.N. Pakhlov and S.I. Eidelman, Phys. Usp. **53**, 219 (2010).
- [2] C. Patrignani *et al.* (Particle Data Group), Chin. Phys. C **40**, 100001 (2016)
- [3] D. Besson *et al.* [CLEO Collaboration], Phys. Rev. Lett. **96**, 092002 (2006) [arXiv:hep-ex/0512038].
- [4] M. Ablikim *et al.* [BES Collaboration], Phys. Lett. B **660**, 315 (2008) [arXiv:0705.4500 [hep-ex]].
- [5] E. Eichten, S. Godfrey, H. Mahlke and J. L. Rosner, Rev. Mod. Phys. **80**, 1161 (2008) [arXiv:hep-ph/0701208].
- [6] M. A. Sanchis-Lozano, Z. Phys. C **62**, 271 (1994).
- [7] K. K. Sharma and R. C. Verma, Int. J. Mod. Phys. A **14**, 937 (1999) [arXiv:hep-ph/9801202].
- [8] A. Datta, P. J. O'Donnell, S. Pakvasa and X. Zhang, Phys. Rev. D **60**, 014011 (1999) [arXiv:hep-ph/9812325].
- [9] G. Goggi and G. Penso, Nucl. Phys. B **165**, 429 (1980).
- [10] W. J. Huo, T. F. Feng and C. x. Yue, Phys. Rev. D **67**, 114001 (2003) [arXiv:hep-ph/0212211].
- [11] Y. Miyazaki *et al.* [Belle Collaboration], Phys. Lett. B **660**, 154 (2008) [arXiv:0711.2189 [hep-ex]].
- [12] J. P. Ma, R. G. Ping and B. S. Zou, Phys. Lett. B **580**, 163 (2004) [arXiv:hep-ph/0311012].
- [13] X. G. He, J. P. Ma and B. McKellar, Phys. Rev. D **47**, 1744 (1993) [arXiv:hep-ph/9211276].
- [14] R. F. Lebed, R. E. Mitchell and E. S. Swanson, Prog. Part. Nucl. Phys. **93**, 143 (2017) [arXiv:1610.04528 [hep-ph]].
- [15] S. Dubynskiy and M. B. Voloshin, Phys. Lett. B **666**, 344 (2008) [arXiv:0803.2224 [hep-ph]].
- [16] B. Aubert *et al.* (BaBar Collab.), Phys. Rev. Lett. **95**, 142001 (2005).
- [17] C. Z. Yuan *et al.* (Belle Collab.), Phys. Rev. Lett. **99**, 182004 (2007).
- [18] B. Aubert *et al.* [BaBar Collaboration], Phys. Rev. Lett. **98**, 212001 (2007)
- [19] X. L. Wang *et al.* (Belle Collab.), Phys. Rev. Lett. **99**, 142002 (2007).

- [20] J. P. Lees *et al.* [BaBar Collaboration], Phys. Rev. D **89**, no. 11, 111103 (2014).
- [21] X. L. Wang *et al.* [Belle Collaboration], Phys. Rev. D **91**, 112007 (2015).
- [22] J. P. Lees *et al.* (BaBar Collab.), Phys. Rev. D **86**, 051102 (2012).
- [23] G. Pakhlova *et al.* [Belle Collaboration], Phys. Rev. Lett. **101**, 172001 (2008)
- [24] M. Ablikim *et al.* [BESIII Collaboration], Phys. Rev. Lett. **115**, no. 11, 112003 (2015).
- [25] C. P. Shen *et al.* [Belle Collaboration], Phys. Rev. D **89**, no. 7, 072015 (2014).
- [26] X. L. Wang *et al.* [Belle Collaboration], Phys. Rev. D **87**, no. 5, 051101 (2013).
- [27] M. Ablikim *et al.* [BESIII Collaboration], Phys. Rev. D **91**, no. 11, 112005 (2015).
- [28] M. Ablikim *et al.* [BESIII Collaboration], Phys. Rev. D **94**, no. 3, 032009 (2016).
- [29] M. Ablikim *et al.* [BESIII Collaboration], Phys. Rev. D **92**, no. 1, 012008 (2015).
- [30] M. Ablikim *et al.* [BESIII Collaboration], Phys. Rev. Lett. **118**, no. 9, 092002 (2017).
- [31] M. Ablikim *et al.* [BESIII Collaboration], Phys. Rev. Lett. **118**, no. 9, 092001 (2017).
- [32] M. Ablikim *et al.* (BESIII Collab.), Phys. Rev. Lett. **112**, 022001 (2014).
- [33] M. Ablikim *et al.* [BESIII Collaboration], Phys. Rev. Lett. **115**, no. 22, 222002 (2015)
- [34] M. Ablikim *et al.* (BESIII Collab.), Phys. Rev. Lett. **110**, 252001 (2013).
- [35] Z. Q. Liu *et al.* (Belle Collab.), Phys. Rev. Lett. **110**, 252002 (2013).
- [36] T. Xiao, S. Dobbs, A. Tomaradze, K. K. Seth, Phys. Lett. B. **727**, 366 (2013).
- [37] M. Ablikim *et al.* [BESIII Collaboration], Phys. Rev. Lett. **115**, no. 11, 112003 (2015).
- [38] M. Ablikim *et al.* (BESIII Collab.), Phys. Rev. Lett. **111**, 242001 (2013).
- [39] M. Ablikim *et al.* [BESIII Collaboration], Phys. Rev. Lett. **113**, no. 21, 212002 (2014).
- [40] M. Ablikim *et al.* (BESIII Collab.), Phys. Rev. Lett. **112**, 132001 (2014)
- [41] M. Ablikim *et al.* [BESIII Collaboration], Phys. Rev. Lett. **115**, no. 18, 182002 (2015).
- [42] M. Ablikim *et al.* [BESIII Collaboration], arXiv:1703.08787 [hep-ex].
- [43] X. L. Wang *et al.* [Belle Collaboration], Phys. Rev. D **91**, 112007 (2015).
- [44] R. Mizuk *et al.* (Belle Collab.), Phys. Rev. D **78**, 072004 (2008).
- [45] K. Chilikin *et al.* (Belle Collab.), Phys. Rev. D **90**, 112009 (2014).
- [46] R. Aaij *et al.* (LHCb Collab.), Phys. Rev. Lett. **112**, 222002 (2014).
- [47] S. K. Choi *et al.* (Belle Collab.), Phys. Rev. Lett. **100**, 142001 (2008).
- [48] K. Chilikin *et al.* (Belle Collab.), Phys. Rev. D **88**, 074026 (2013).

- [49] M. Ablikim *et al.* [BESIII Collaboration], Phys. Rev. Lett. **112**, no. 9, 092001 (2014).
- [50] C. J. Morningstar and M. J. Peardon, Phys. Rev. D **60**, 034509 (1999) [arXiv:hep-lat/9901004].
- [51] A. Hart, C. McNeile, C. Michael and J. Pickavance [UKQCD Collaboration], Phys. Rev. D **74**, 114504 (2006) [arXiv:hep-lat/0608026].
- [52] E. Klempt and A. Zaitsev, Phys. Repts. **454**, 1 (2007) [arXiv:0708.4016 [hep-ph]].
- [53] J. Z. Bai, *et. al.* (BES Collaboration), Phys. Rev. Lett. **91**, 022001 (2003).
- [54] J. P. Alexander *et. al.* (CLEO Collaboration), Phys. Rev. D **82**, 092002 (2010).
- [55] I. S. Shapiro, Phys. Rept. **35**, 129 (1978).
- [56] M. Ablikim, *et. al.* (BESIII Collaboration), Chinese Phys. C **34**, 421 (2010).
- [57] M. Ablikim, *et. al.* (BESIII Collaboration), Phys. Rev. Lett. **108**, 112003 (2012).
- [58] M. Ablikim, *et. al.* (BESIII Collaboration), Phys. Rev. Lett. **106**, 072002 (2011).
- [59] M. Ablikim, *et. al.* (BESIII Collaboration), Phys. Rev. Lett. **117**, 042002 (2016).
- [60] M. Ablikim, *et. al.* (BESIII Collaboration), Phys. Rev. Lett. **115**, 091803 (2015).
- [61] G. Bonvicini *et al.* [CLEO Collaboration], Phys. Rev. D **89**, 072002 (2014) [arXiv:1312.6775 [hep-ex]].
- [62] D. Cronin-Hennessy *et al.*, Phys. Rev. D **80**, 072001 (2009).
- [63] S. Godfrey and N. Isgur, Phys. Rev. D **32**, 189 (1985).
- [64] P. del Amo Sanchez *et al.* [BaBar Collaboration], Phys. Rev. D **82**, 111101 (2010).
- [65] R. Aaij *et al.* [LHCb Collaboration], JHEP **1309**, 145 (2013).
- [66] E. S. Swanson, Phys. Rept. **429**, 243 (2006) [arXiv:hep-ph/0601110].
- [67] G. Pakhlova *et al.* [Belle Collaboration], Phys. Rev. Lett. **100**,062001 (2008) [arXiv:0708.3313 [hep-ex]].
- [68] T. J. Burns, F. E. Close and C. E. Thomas, Phys. Rev. D **77**, 034008 (2008) [arXiv:0709.1816 [hep-ph]].
- [69] A. V. Evdokimov *et al.* [SELEX Collaboration], Phys. Rev. Lett. **93**, 242001 (2004) [arXiv:hep-ex/0406045].
- [70] J. Brodzicka *et al.* [Belle Collaboration], Phys. Rev. Lett. **100**, 092001 (2008) [arXiv:0707.3491 [hep-ex]].
- [71] B. Aubert *et al.* [BaBar Collaboration], Phys. Rev. Lett. **97**, 222001 (2006) [arXiv:hep-ex/0607082].
- [72] A. Bondar and A. Poluektov, Eur. Phys. J. C **47**, 347 (2006) [arXiv:hep-ph/0510246].

- [73] A. Bondar, T. Gershon and P. Krokovny, Phys. Lett. B **624**, 1 (2005) [hep-ph/0503174].
- [74] B. I. Eisenstein *et al.* [CLEO Collaboration], Phys. Rev. D **78**, 052003 (2008) [arXiv:0806.2112 [hep-ex]].
- [75] M. Ablikim *et al.* [BESIII Collaboration], Phys. Rev. D **89** no.5, 051104 (2014) [arXiv:1312.0374 [hep-ex]].
- [76] A. Zupanc *et al.* [Belle Collaboration], JHEP **1309** 139 (2013) [arXiv:1307.6240 [hep-ex]].
- [77] CKM Fitter Group Home Page, <http://www.slac.stanford.edu/xorg/ckmfitter>
- [78] E. Follana, C. T. H. Davies, G. P. Lepage and J. Shigemitsu [HPQCD Collaboration], Phys. Rev. Lett. **100**, 062002 (2008) [arXiv:0706.1726 [hep-lat]].
- [79] N. E. Adam *et al.* [CLEO Collaboration], Phys. Rev. Lett. **97**, 251801 (2006) [arXiv:hep-ex/0604044].
- [80] C. Aubin *et al.* [Fermilab Lattice Collaboration], Phys. Rev. Lett. **94**, 011601 (2005) [arXiv:hep-ph/0408306].
- [81] M. Ablikim *et al.* [BESIII Collaboration], Phys. Rev. D **92**, no. 7, 072012 (2015) [arXiv:1508.07560 [hep-ex]].
- [82] S. Bianco, F. L. Fabbri, D. Benson and I. Bigi, Riv. Nuovo Cim. **26**, 1 (2003) [arXiv:hep-ex/0309021].
- [83] Heavy Flavor Averaging Group Home Page, <http://www.slac.stanford.edu/xorg/hfag/>
- [84] D. M. Asner and W. M. Sun, Phys. Rev. D **73**, 034024 (2006) [arXiv:hep-ph/0507238].
- [85] X. D. Cheng, K. L. He, H. B. Li, Y. F. Wang and M. Z. Yang, Phys. Rev. D **75**, 094019 (2007) [arXiv:0704.0120 [hep-ex]].
- [86] A. Bondar, A. Poluektov, V. Vorobiev, Phys. Rev. D **82**, 034033 (2010) [arXiv:1004.2350].
- [87] M. Bona *et al.*, arXiv:0709.0451 [hep-ex].
- [88] N.K. Nisar *et al.*[Belle Collaboration], Phys. Rev. Lett. **112**, 211601 (2014) [arXiv:1404.1266 [hep-ex]].
- [89] B.R. Ko *et al.*[Belle Collaboration], Phys. Rev. Lett. **106**, 211801 (2011) [arXiv:1101.3365 [hep-ex]].
- [90] R. Aaij *et al.*[LHCb Collaboration], JHEP **10**, 055 (2015) [arXiv:1508.06087 [hep-ex]].
- [91] X.C. Tian *et al.*[Belle Collaboration], Phys. Rev. Lett. **95**, 231801 (2005) [arXiv:hep-ex/0507071].
- [92] T. Aaltonen *et al.*[CDF Collaboration], Phys. Rev. D **86**, 032007 (2012) [arXiv:1207.0825 [hep-ex]].
- [93] H. Mendez *et al.*[CLEO Collaboration], Phys. Rev. D **81**, 052013 (2010) [arXiv:0906.3198 [hep-ex]].

- [94] D. M. Asner *et al.*[CLEO Collaboration], Phys. Rev. D **70**, 091101 (2004).
- [95] B. Aubert *et al.*[BaBar Collaboration], Phys. Rev. D **78**, 051102 (2008) [arXiv:0802.4035 [hep-ex]].
- [96] B.I. Eisenstein *et al.*[CLEO Collaboration], Phys. Rev. D **78**, 052003 (2008) [arXiv:0806.2112 [hep-ex]].
- [97] E. M. Aitala *et al.*[E791 Collaboration], Phys. Lett. B **403**, 377 (1997).
- [98] X. C. Tian *et al.*[Belle Collaboration], Phys. Rev. Lett. **95**, 231801 (2005) [hep-ex/0507071].
- [99] J. M. Link *et al.*[FOCUS Collaboration], Phys. Lett. B **622**, 239 (2005) [hep-ex/0506012].
- [100] B. Aubert *et al.*[BaBar Collaboration], Phys. Rev. Lett. **100**, 061803 (2008) [arXiv:0709.2715 [hep-ex]].
- [101] M. Staric *et al.*[Belle Collaboration], Phys. Lett. B **670**, 190 (2008) [arXiv:0807.0148 [hep-ex]].
- [102] J.P. Alexander *et al.*[CLEO Collaboration], Phys. Rev. D **79**, 052001 (2009) [arXiv:0901.1216 [hep-ex]].
- [103] P.U.E. Onyisi *et al.*[CLEO Collaboration], Phys. Rev. D **88**, 032009 (2013) [arXiv:1306.5363 [hep-ex]].
- [104] Y. Grossman, A. L. Kagan and Y. Nir, Phys. Rev. D **75**, 036008 (2007) [arXiv:hep-ph/0609178].
- [105] B. Aubert *et al.* [BaBar Collaboration], Phys. Rev. D **78**, 011105 (2008) [arXiv:0712.2249].
- [106] M. Staric *et al.* [Belle Collaboration], Phys. Rev. Lett. **98**, 211803 (2007) [arXiv:hep-ex/0703036].
- [107] A. A. Petrov, arXiv:0711.1564 [hep-ph].
- [108] D. s. Du, Eur. Phys. J. C **50**, 579 (2007) [arXiv:hep-ph/0608313].
- [109] A. A. Petrov, Phys. Rev. D **69**, 111901 (2004) [arXiv:hep-ph/0403030].
- [110] D. M. Asner *et al.* [CLEO Collaboration], Phys. Rev. D **70**, 091101 (2004) [arXiv:hep-ex/0311033].
- [111] I. I. Bigi, arXiv:0710.2714 [hep-ph].
- [112] A. Datta and D. London, Int. J. Mod. Phys. A **19**, 2505 (2004) [arXiv:hep-ph/0303159].
- [113] G. Burdman and I. Shipsey, Ann. Rev. Nucl. Part. Sci. **53**, 431 (2003) [arXiv:hep-ph/0310076].
- [114] B. Aubert *et al.* [BaBar Collaboration], Phys. Rev. D **78**, 071101 (2008) [arXiv:0808.1838 [hep-ex]].
- [115] P. Rubin *et al.* [CLEO Collaboration], Phys. Rev. D **82**, 092007 (2010) [arXiv:1009.1606 [hep-ex]].

- [116] V. M. Abazov *et al.* [D0 Collaboration], Phys. Rev. Lett. **100**, 101801 (2008) [arXiv:0708.2094 [hep-ex]].
- [117] S. Prelovsek and D. Wyler, Phys. Lett. B **500**, 304 (2001) [arXiv:hep-ph/0012116].
- [118] G. Burdman, E. Golowich, J. L. Hewett and S. Pakvasa, Phys. Rev. D **66**, 014009 (2002) [arXiv:hep-ph/0112235].
- [119] S. Fajfer, N. Kosnik and S. Prelovsek, Phys. Rev. D **76**, 074010 (2007) [arXiv:0706.1133 [hep-ph]].
- [120] J. P. Lees *et al.* [BaBar Collaboration], Phys. Rev. D **85**, 091107 (2012) [arXiv:1110.6480 [hep-ex]].
- [121] M. Petric *et al.* [Belle Collaboration], Phys. Rev. D **81**, 091102 (2010) [arXiv:1003.2345 [hep-ex]].
- [122] R. Aaij *et al.* [LHCb Collaboration], Phys. Lett. B **725**, 15 (2013) [arXiv:1305.5059 [hep-ex]].
- [123] A. Freyberger *et al.* [CLEO Collaboration], Phys. Rev. Lett. **76**, 3065 (1996) [Erratum-ibid. **77**, 2147 (1996)].
- [124] J. P. Lees *et al.* [BaBar Collaboration], Phys. Rev. D **84**, 072006 (2011) [arXiv:1107.4465 [hep-ex]].
- [125] R. Aaij *et al.* [LHCb Collaboration], Phys. Lett. B **724**, 203 (2013) [arXiv:1304.6365 [hep-ex]].
- [126] B. Aubert *et al.* [BaBar Collaboration], arXiv:hep-ex/0607051.
- [127] K. Kodama *et al.* [E653 Collaboration], Phys. Lett. B **345**, 85 (1995).
- [128] D. Pirjol and T. M. Yan, Phys. Rev. D **56**, 5483 (1997) [arXiv:hep-ph/9701291].
- [129] R. Mizuk, arXiv:0712.0310 [hep-ex].
- [130] R. Aaij *et al.* [LHCb Collaboration], arXiv:1701.07873 [hep-ex].
- [131] R. Aaij *et al.* [LHCb Collaboration], arXiv:1703.04639 [hep-ex].
- [132] J. Yelton *et al.* [Belle Collaboration], Phys. Rev. D **94**, no. 5, 052011 (2016) [arXiv:1607.07123 [hep-ex]].
- [133] Y. Kato *et al.* [Belle Collaboration], Phys. Rev. D **94**, no. 3, 032002 (2016) [arXiv:1605.09103 [hep-ex]].
- [134] A. Zupanc *et al.* [Belle Collaboration], Phys. Rev. Lett. **113**, no. 4, 042002 (2014) [arXiv:1312.7826 [hep-ex]].
- [135] M. Ablikim *et al.* [BESIII Collaboration], Phys. Rev. Lett. **116**, no. 5, 052001 (2016) [arXiv:1511.08380 [hep-ex]].
- [136] W. Song, JPS Conf. Proc. **13**, 020041 (2017).

- [137] G. Pakhlova *et al.* [Belle Collaboration], Phys. Rev. Lett. **101**, 172001 (2008) [arXiv:0807.4458[hep-ex]].
- [138] H. X. Chen, W. Chen, X. Liu and S. L. Zhu, Phys. Rept. **639**, 1 (2016) [arXiv:1601.02092 [hep-ph]].
- [139] X. D. Guo, D. Y. Chen, H. W. Ke, X. Liu and X. Q. Li, Phys. Rev. D **93**, no. 5, 054009 (2016) [arXiv:1602.02222 [hep-ph]].
- [140] A. Esposito, A. L. Guerrieri, F. Piccinini, A. Pilloni and A. D. Polosa, Int. J. Mod. Phys. A **30**, 1530002 (2015) [arXiv:1411.5997 [hep-ph]].
- [141] X. Liu, Chin. Sci. Bull. **59**, 3815 (2014) [arXiv:1312.7408 [hep-ph]].
- [142] I. I. Bigi, X. W. Kang and H. B. Li, arXiv:1704.04708 [hep-ph].
- [143] R. Aaij *et al.* [LHCb Collaboration], Nature Phys. (2017) doi:10.1038/nphys4021 [arXiv:1609.05216 [hep-ex]].
- [144] J. Liu, R. G. Ping and H. B. Li, τ -charm factory,” J. Phys. G **42**, no. 9, 095002 (2015).
- [145] J. M. Link *et al.* [FOCUS Collaboration], Phys. Lett. B **634**, 165 (2006) [hep-ex/0509042].
- [146] J. F. Donoghue and S. Pakvasa, Phys. Rev. Lett. **55**, 162 (1985).
- [147] X. W. Kang, H. B. Li, G. R. Lu and A. Datta, Int. J. Mod. Phys. A **26**, 2523 (2011) [arXiv:1003.5494 [hep-ph]].
- [148] E. Braaten, S. Narison and A. Pich, Nucl. Phys. B **373**, 581 (1992).
- [149] S. Bethke, arXiv:0908.1135 [hep-ph].
- [150] E. Gamiz, M. Jamin, A. Pich, J. Prades and F. Schwab, JHEP **0301**, 060 (2003) [arXiv:hep-ph/0212230]; Phys. Rev. Lett. **94**, 011803 (2005) [arXiv:hep-ph/0408044].
- [151] A. Lusiani [BaBar Collaboration], EPJ Web Conf. **118**, 01018 (2016).
- [152] L. Michel, Proc. Phys. Soc. A **63**, 514 (1950); C. Bouchiat and L. Michel, Phys. Rev. **106**, 170 (1957).
- [153] J. R. Ellis, J. Hisano, M. Raidal and Y. Shimizu, Phys. Rev. D **66**, 115013 (2002) [arXiv:hep-ph/0206110]; T. Fukuyama, T. Kikuchi and N. Okada, Phys. Rev. D **68**, 033012 (2003) [arXiv:hep-ph/0304190]; A. Brignole and A. Rossi, Phys. Lett. B **566**, 217 (2003) [arXiv:hep-ph/0304081].
- [154] H. Hayashii Possible search for tau \rightarrow mu/e gamma at the Super-tau-charm factory Talk at 10th International Workshop on Tau Lepton Physics, Novosibirsk, Russia, 22-25 September 2008 <http://tau08.inp.nsk.su/talks/27/Hayashii.ppt>
- [155] A. V. Bobrov, A. V. and A. E. Bondar, Nucl. Phys. Proc. Suppl., **225-227** (2012) 195; A. V. Bobrov and A. E. Bondar, Nucl. Phys. Proc. Suppl. **253-255** (2014) 199.
- [156] I. I. Bigi and A. I. Sanda, Phys. Lett. B **625**, 47 (2005) [arXiv:hep-ph/0506037].
- [157] Y. S. Tsai, SLAC-PUB-5003

- [158] Y. S. Tsai, Phys. Rev. D **51**, 3172 (1995) [arXiv:hep-ph/9410265].
- [159] J. H. Kuhn and E. Mirkes, Phys. Lett. B **398**, 407 (1997) [arXiv:hep-ph/9609502].
- [160] A. Datta, K. Kiers, D. London, P. J. O'Donnell and A. Szykman, Phys. Rev. D **75**, 074007 (2007) [Erratum-ibid. D **76**, 079902 (2007)] [arXiv:hep-ph/0610162].
- [161] D. Delepine, G. Faisl, S. Khalil and G. L. Castro, Phys. Rev. D **74**, 056004 (2006) [arXiv:hep-ph/0608008].
- [162] K. Kiers, K. Little, A. Datta, D. London, M. Nagashima and A. Szykman, Phys. Rev. D **78**, 113008 (2008) [arXiv:0808.1707 [hep-ph]].
- [163] P. Avery *et al.* [CLEO Collaboration], Phys. Rev. D **64**, 092005 (2001) [arXiv:hep-ex/0104009].
- [164] G. Bonvicini *et al.* [CLEO Collaboration], Phys. Rev. Lett. **88**, 111803 (2002) [arXiv:hep-ex/0111095].
- [165] J. P. Lees *et al.* [BaBar Collaboration], Phys. Rev. D **85** (2012) 031102 [Erratum-ibid. D **85** (2012) 099904] [arXiv:1109.1527 [hep-ex]].
- [166] M. Bischofberger *et al.* [Belle Collaboration], Phys. Rev. Lett. **107** (2011) 131801 [arXiv:1101.0349 [hep-ex]].
- [167] J. Kühn and M. Steinhauser, Nucl. Phys. B **619** (2001) 588; Erratum-ibid, B640 (2002) 415.
- [168] M.A. Shifman, A.I. Vainshtein and V.I. Zakharov, Nucl. Phys. B **147** (1979) 385.
- [169] M. Davier, S. Eidelman, A. Höcker, Z. Zhang, Eur. Phys. J. C **31** (2003) 503.
- [170] B. Pietrzyk and H. Burkhardt, Phys. Lett. B **513** (2001) 46.
- [171] A. Czarnecki, S.I. Eidelman and S.G. Karshenboim, Phys. Rev. D **65** (2002) 053004.
- [172] K. Hagiwara, R. Liao, A. D. Martin, D. Nomura and T. Teubner, J. Phys. G **38** (2011) 085003
- [173] J. Grange *et al.* [Muon g-2 Collaboration], FERMILAB-DESIGN-2014-02, arXiv:1501.06858 [physics.ins-det].
- [174] M. Aoki, et al., KEK-J-PARC-PAC2009-12.
- [175] M. Baak *et al.* [Gfitter Group], Eur. Phys. J. C **74** (2014) 3046
- [176] P. Azzi *et al.*, arXiv:1703.01626 [hep-ph].
- [177] P. A. Baikov *et al.*, Phys. Lett. B **714**, 62 (2012).
- [178] A. Osterheld *et al.*, SLAC-PUB-4160, 1986.
- [179] J. Burmeister *et al.*, Phys. Lett. **66B** (1977) 395.
- [180] R. Brandelik *et al.*, Phys. Lett. **76B** (1978) 361.

- [181] J.L. Siegrist *et al.*, Phys. Rev. Lett. **36** (1976) 700.
- [182] J.L. Siegrist *et al.*, Phys. Rev. D **26** (1982) 969.
- [183] J.Z.Bai *et al.*, Phys. Rev. Lett. **84**, 594 (2000).
- [184] J.Z.Bai *et al.*, Phys. Rev. Lett. **88**, 101802 (2002).
- [185] M. Ablikim *et al.*, Phys. Rev. Lett. **97** (2006) 262001
- [186] M. Ablikim *et al.* [BES Collaboration], Phys. Lett. B **677** (2009) 239
- [187] V. V. Anashin *et al.*, Phys. Lett. B **753** (2016) 533
- [188] V. V. Anashin *et al.*, arXiv:1610.02827 [hep-ex].
- [189] M. Davier, arXiv:1612.02743 [hep-ph].
- [190] D. Babusci *et al.* [KLOE Collaboration], Phys. Lett. B **720** (2013) 336
- [191] V. P. Druzhinin, S. I. Eidelman, S. I. Serednyakov and E. P. Solodov, Rev. Mod. Phys. **83** (2011) 1545.
- [192] M. Ablikim *et al.* [BESIII Collaboration], Phys. Lett. B **753** (2016) 629.
- [193] K.K. Seth *et al.*, Phys. Rev. D **72**, 017501 (2005).
- [194] M. Ablikim *et al.*, Phys. Lett. B **660**, 315 (2008).
- [195] N. Brambilla *et al.*, Eur. Phys. J. C **71** (2011) 1534.
- [196] M. Ablikim *et al.* [BES Collaboration], eConf C **070805**, 02 (2007) [Phys. Lett. B **660**, 315 (2008)].
- [197] T. V. Uglov, Y. S. Kalashnikova, A. V. Nefediev, G. V. Pakhlova and P. N. Pakhlov, JETP Letters vol. 105, issue 1, page 3 (2017)
- [198] B. Dehnadi, A. H. Hoang and V. Mateu, JHEP **1508** (2015) 155
- [199] A. Bondar *et al.*, Phys. Lett. B **697**, 159 (2011).
- [200] C. F. Redmer, EPJ Web Conf. **130**, 01013 (2016).

Chapter 2

Detector

2.1 Overview

The physics program of experiments at the Super $c\tau$ factory with a peak luminosity of $10^{35} \text{ cm}^{-2}\text{c}^{-1}$ in the energy region $2E = 2 \div 5 \text{ GeV}$ is dedicated to studies of rare decays of D mesons, τ lepton, $D^0\bar{D}^0$ oscillations and searches for so-far unobserved lepton-flavor-violating τ decays, in particular $\tau \rightarrow \mu\gamma$ decay. The proposed program requires creation of a universal magnetic detector with a field of about 1 T. The detector should have the following features:

- an excellent momentum resolution for charged particles and a good energy resolution for photons;
- a particle identification system with the best parameters among detectors already existing or under construction. For selection of rare D decays K/π separation higher than 3σ is needed. In addition, for selection of $\tau \rightarrow \mu\gamma$ decay and suppression of high π mesons background a robust μ/π separation up to 1.2 GeV/ c momentum is required;
- a digitizing hardware and data acquisition system, able to read events at a rate of 300 – 400 kHz with an average event length of about 30 kB;
- a powerful trigger capable to select physics events and suppress very high rate background processes.

To achieve a high data taking efficiency and to minimize detector maintenance time, the detector design should satisfy the following requirements:

- the digitization hardware should reside inside the detector 10 Gbit optical links will be used to transmit the data;
- the detector design should provide fast access to detector subsystems for repair and hardware replacement; the typical disassembling–repair–assembling time should not exceed 12 – 24 hours;
- input (output) of the detector magnetic field should not take more than two-three hours;
- a movable radiation shield should provide fast access to detector subsystems to enable the personnel to work on the detector and its technological entresols while beams are in the collider.

The design of the universal magnetic detector for $c\tau$ factory is based on the experience of the Budker Institute experiments as well as that coming from the BaBar and Belle collaboration.

The detector (see Fig. 2.1) contains a standard set of subsystems:

- a vacuum chamber,
- a vertex detector,
- a drift chamber,
- a particle identification system based on a Cherenkov detector with a multilayer aerogel radiator (*Focusing Aerogel RICH – FARICH*),
- an electromagnetic calorimeter based on pure CsI crystals,
- a superconducting coil produced by the conventional technology,
- an iron yoke with a muon system inside.

2.2 Vacuum chamber

The beams collide in the center of a beryllium vacuum chamber with a radius of 20 mm and a length of 600 mm. The wall thickness is 1 mm. To suppress the background from synchrotron radiation, the chamber inside is coated with a 0.05 mm thick copper layer. This design introduces a small amount of material, for normal incidence particles it is about 0.6% of the radiation length.

2.3 Vertex detector

The Vertex detector (VD) is placed between the vacuum chamber and the drift chamber and provides the detection solid angle up to 98 %. The VD is a cylinder with a length of 60 cm and inner and outer diameters of 50 mm and 400 mm respectively. Its task is to detect secondary vertices from the decays of short-lived particles such as K_S^0 or Λ . Furthermore, the VD complements the drift chamber in measuring the momenta of charged particles. Since the VD is placed in the vicinity of the beam pipe, it should handle a high particle flux when the collider operates at its maximum luminosity of $10^{35} \text{cm}^{-2} \text{s}^{-1}$.

Information from the VD can be processed either together with the data from the drift chamber to improve the momentum resolution, or alone to reconstruct secondary vertices.

Two options of the VD are foreseen at the moment: a time projection chamber (TPC) discussed below or a stack of silicon strip layers.

2.3.1 Time projection chamber

A time projection chamber [1] is a combination of drift and proportional chambers (see example in Fig. 2.2). The drift volume is filled with a gas mixture, e.g., Ar/CO₂ 80/20, and has an axial electric field created by two endcap anode planes and a mesh cathode in the middle of the chamber. The field uniformity is preserved using a special field cage.

A charged particle traversing the sensitive volume leaves a track as a chain of clusters of the ionized gas. The linear cluster density depends on the gas properties. For example, for

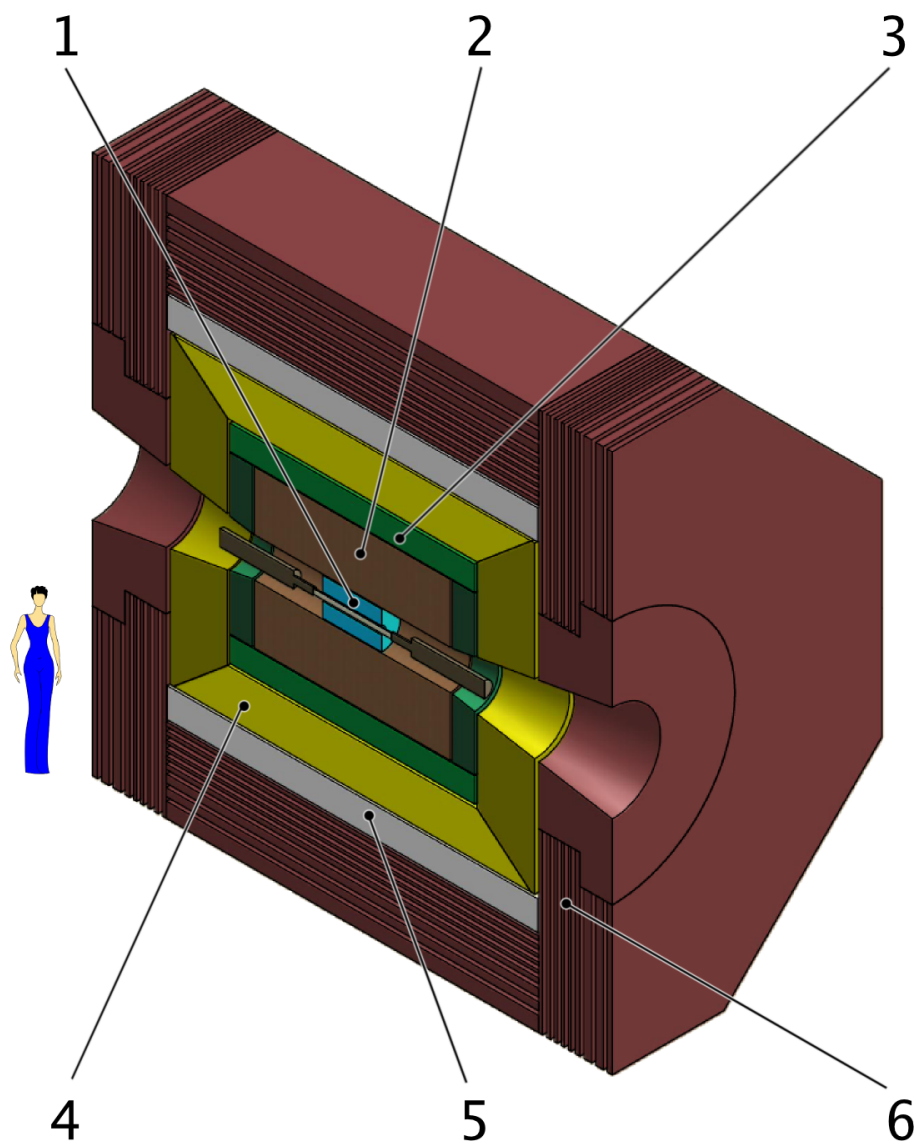


Figure 2.1. Universal magnetic detector: 1 – vertex detector; 2 – drift chamber; 3 – FARICH identification system; 4 – calorimeter; 5 – superconducting coil; 6 – yoke with a muon system.

argon at normal temperature and pressure it is about 30 clusters per cm. Electrons drift with a constant velocity towards the anode planes and create avalanches detected by a sensitive pad planes providing information about two coordinates. The third coordinate of the track is calculated as a product of the drift time of each primary electron cluster and the drift velocity. Despite the relatively large drift distance of about 30 cm, the transverse diffusion is relatively small due to the longitudinal magnetic field of 1 T (see Fig. 2.3). That allows the transverse spatial resolution to achieve 50–100 μm depending on the drift path. In the longitudinal direction the resolution is somewhat worse — about 300 μm because of larger diffusion.

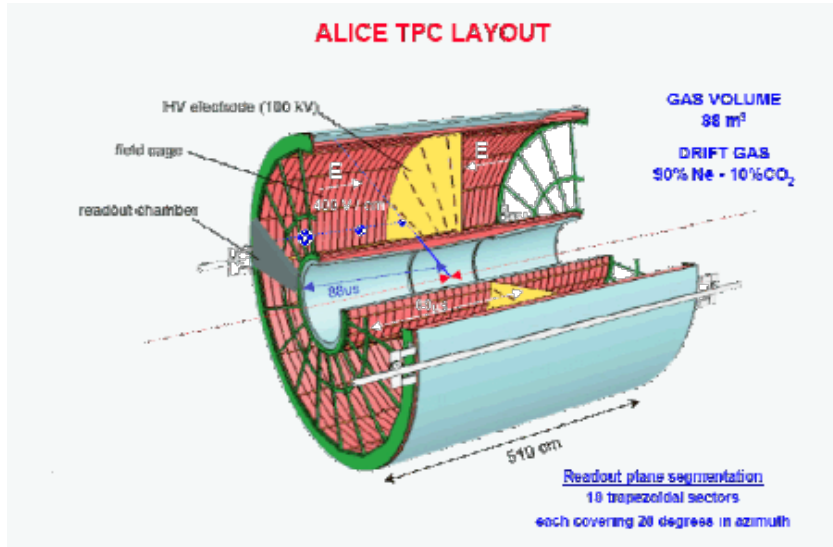


Figure 2.2. ALICE time projection chamber (CERN).

Currently, TPCs use multiwire proportional chambers (MWPCs) for detection of ionization clusters. Those chambers cannot work in the continuous mode because of a backflow of ions, resulting in a space charge accumulation which leads to electric field distortion. And the later deteriorates the spatial resolution. A special protection mesh is needed to prevent the effect. This mesh opens access to the MPWC by an external trigger signal. As a result, a large dead time after each event leads to a loss of physics events.

A new generation of colliders including the $c\tau$ factory will have a very small time between consequent events, and thus a standard TPC cannot be used. To overcome this problem, several new readout schemes were suggested based on the novel micropattern gas technologies. For example, the $\overline{P}ANDA$ Collaboration is developing a TPC [2] with the continuous readout using gas electron multipliers (GEM) [3]. The same chamber is being designed for a detector for the international linear collider by the LC TPC Collaboration [4]. Besides the GEM option, the LC TPC Collaboration also studies the possibility of using Micromegas for signal amplification (see Fig. 2.4). It should be noted that both amplification methods allow to suppress the backflow of ions by more than three orders of magnitude. Therefore, a TPC equipped with an additional device can work in the continuous mode.

A very good spatial resolution, close to the theoretical limit, has been achieved during tests of the prototypes with different readout schemes. The tests have been done with the “hot” gas mixture, Ar/CF₄/C₄H₁₀ in the proportion 95/3/2. The spatial resolution of the prototypes with GEM and Micromegas in a 1 T magnetic field parallel to the electric field lines 5 cm from the readout plane was equal to 52 μm and 55 μm , respectively (see Figs. 2.5 and 2.6).

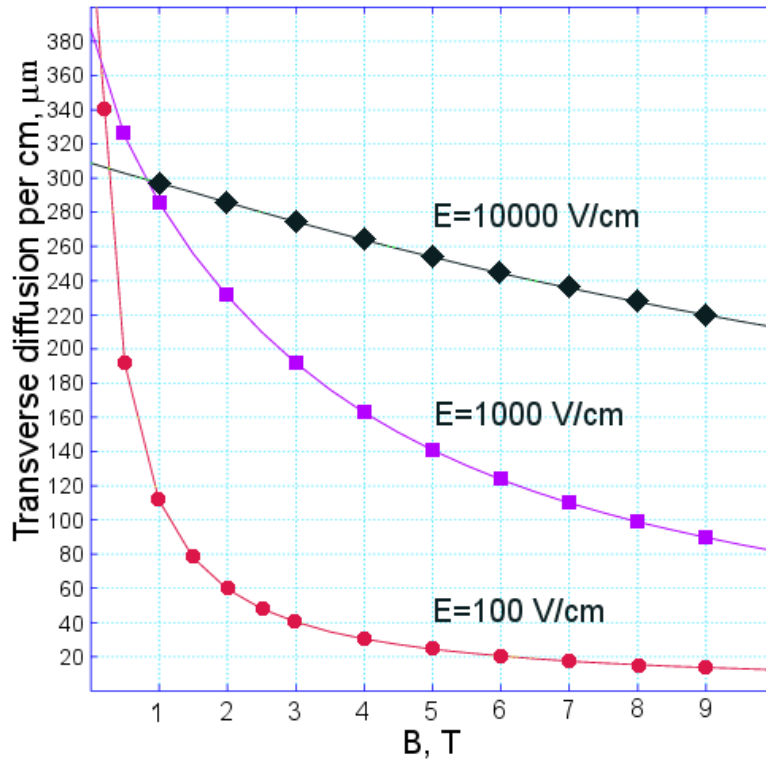


Figure 2.3. Transverse diffusion as a function of magnetic field intensity for the gas mixture Ar/C_2H_4 80/20 for different electric field values.

Further improvement of the spatial resolution can be achieved with the sensitive pad size decrease. In the examples above, the pad sizes were $1.2 \times 5.4 \text{ mm}^2$ for the GEM version and $3.2 \times 7 \text{ mm}^2$ for the Micromegas one. It should be noted that in the latter case (Micromegas) the sensitive pads were covered by a special resistive layer to spread the charge over a larger area and improve the spatial resolution. At the present time an experiment to directly detect a signal in the silicon pixel detector with a pixel size of $50 \times 50 \mu\text{m}^2$ is in progress. It is anticipated that the spatial resolution in this case will be about $40 \mu\text{m}$ in the vicinity of the detection plane.

Apart from the position information, the TPC can be used for particle identification based on the ionization energy loss in gas. Indeed, at a typical pad size of 2 mm each particle crossing the chamber along the radius will produce about 70 fired pads. That should provide the dE/dx resolution at the level of a few percent.

There is another issue with of the chamber wall thickness minimization, although should the walls should be strong enough to keep the electric potential difference at a level of a few tens kilovolts. The high values of potential are required to provide an electric field in the order of $200 - 300 \text{ V/cm}$, allowing to have an electron drift velocity about $5 \text{ cm}/\mu\text{s}$.

At present the detector design is studied using a dedicated computer simulation with Geant4 and Root packages.

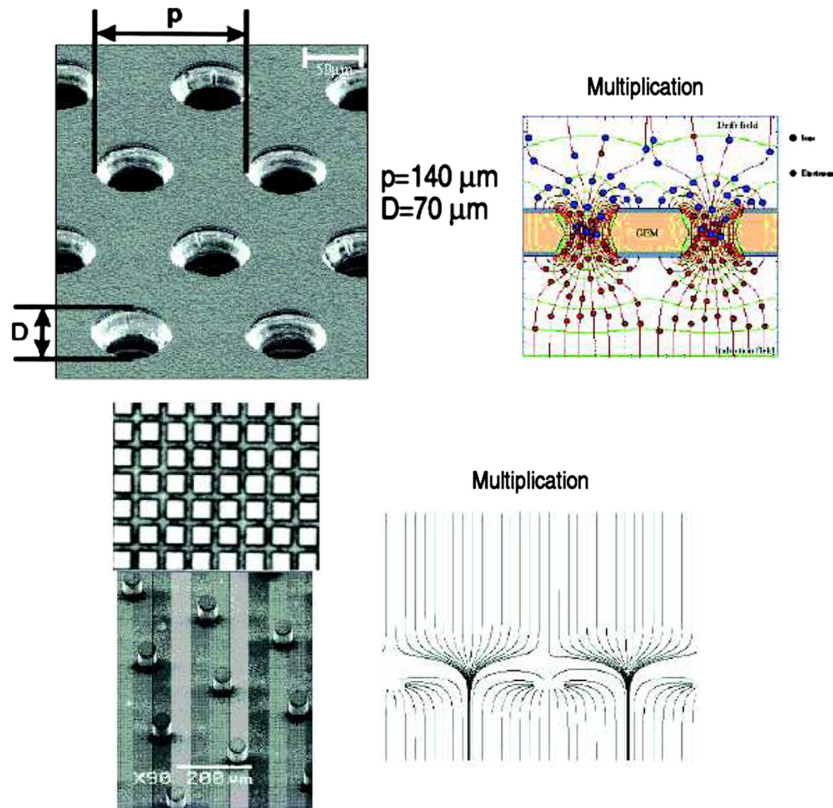


Figure 2.4. Layout and principle of GEM operation (upper row) and Micromegas (lower row). The figure is taken from [5].

2.4 Drift chamber

2.4.1 Introduction

The drift chamber (DCH) is the main tracking and momentum-measuring system. It provides precision momentum measurements as well as good particle identification for low momentum tracks. The DCH design is based on the BaBar drift chamber described in detail in [6].

2.4.2 Drift chamber design

The drift chamber has cylindrical shape with 1.6 m outer diameter, 0.4 m inner diameter and 2.0 m length. The endplates are carrying an axial load of about 32,000 N and made of 24 mm thick aluminum. They hold plastic and metal feedthroughs for the wires. The maximum total deflection of the endplates under loading is small, it is about 2 mm or 28% of the 7 mm wire elongation under tension. The inner cylinder is made of 1.5 mm carbon fiber. The outer cylinder is made of 5 mm thick fiber glass. The inner cylindrical wall of DCH carries 40% of the wire load, while the outer wall bears 60%. To simplify installation this external wall was constructed of two half-cylinders with longitudinal and circumferential joints. The main structural element consists of 5 mm fiber glass. The outer shell is capable to withstand a pressure change up to 30 mbar and temperature variations up to $\pm 20^\circ\text{C}$, those conditions could be encountered during shipping or installation. The aluminum foil, 25 μm thick on the internal surface and 100 μm on the external one, has good electric contact with the endplates and thereby ensures the RF shield for the chamber. The total

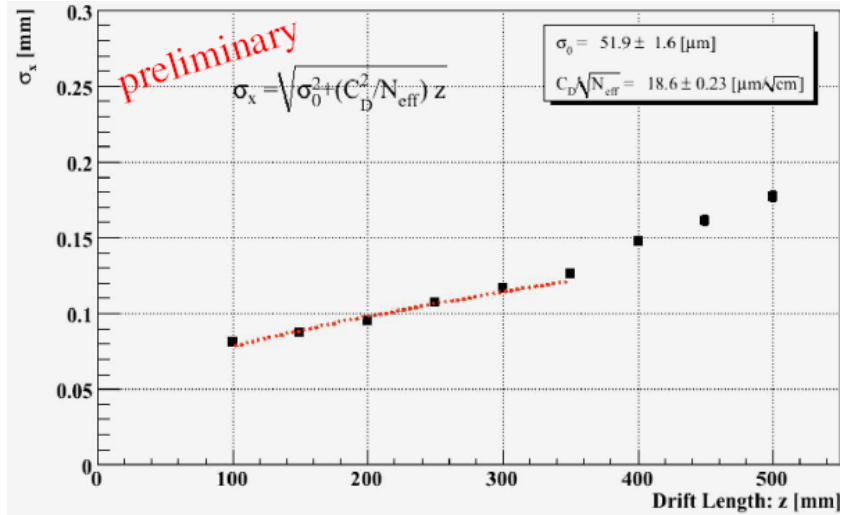


Figure 2.5. Spatial resolution of the TPC prototype with the GEM readout.

thickness of the DCH for particles at normal incidence is $1.08\%X_0$, where $0.2\%X_0$ is a contribution from wires and gas mixture and $0.28\%X_0$ is from the inner wall.

The drift system of the chamber consists of 40 layers with 7104 close-packed small hexagonal cells. Each cell has a single sense wire surrounded by field-shaping wires and is approximately 1 cm in radius.

2.4.3 Drift cells

2.4.3.1 Layer arrangement

The layers are grouped by four into ten superlayers with the same wire orientation and equal numbers of cells in each layer of a superlayer. Sequential layers are staggered by half a cell. This arrangement allows finding a local segment and left-right ambiguity resolution within a superlayer, even if one of the four signals is missed. The stereo angles of the superlayers alternate between axial (A) and stereo (U,V) pairs in the order of AUVAUVAUVA as shown in Fig. 2.7.

To provide three-dimensional track reconstruction the superlayers appear alternately as axial (with wires parallel to the z axis) and small-angle stereo (with wire endpoints offset by 7 to 12 cells, in alternate directions). The stereo angles vary between ± 32 mrad and ± 56 mrad; they have been chosen so that the drilling patterns are identical for the two endplates. The hole pattern has a 16-fold azimuthal symmetry which is well suited to the modularity of the electronic readout and trigger system.

2.4.3.2 Cell Design and Wires

The drift cells are hexagonal shape, 11.9 mm in the radial and 19.0 mm in the azimuthal directions, respectively. The hexagonal cell configuration is preferable for our detector because approximate circular symmetry can be achieved over a large portion of the cell. The choice of the aspect ratio has a benefit of decreasing the number of wires and electronic channels, the 40-layer chamber fitting in a confined radial space. Each cell consists of one sense wire surrounded by six field wires.

The sense wires are made of tungsten-rhenium alloy, 20 μm in diameter and tensioned with

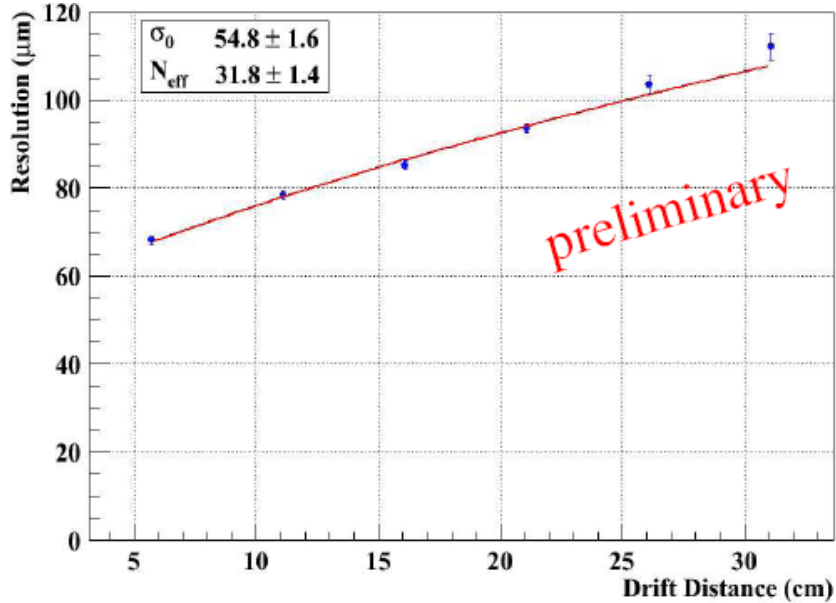


Figure 2.6. Spatial resolution of the TPC prototype with the Micromegas readout.

a weight of 30 g. The deflection due to gravity is 200 μm at midlength. Tungsten-rhenium has a substantially higher linear resistivity (290 Ω/m) in comparison with pure tungsten (160 Ω/m), but is considerably stronger and has better surface quality.

While the field wires are grounded, a positive high voltage is applied to the sense wires. An avalanche gain of approximately $5 \cdot 10^4$ is obtained at a typical operating voltage of 1960 V and a 80/20 helium/isobutane gas mixture.

The tension on the approximately 2 m-long sense wires was chosen to be relatively low so that the aluminum field wires have a matching gravitational sag and are tensioned well below the elastic limit. A simulation of the electrostatic forces shows that the cell configuration has no instability problems. At the nominal operating voltage of 1960 V, the wires deflect by less than 60 μm .

The tension of the field wires is 155 g to match the gravitational sag of the sense wires to within 20 μm . This tension is less than half the tensile yield strength of the aluminum wire. For cells at the inner or outer boundary of a superlayer, two guard wires are added to improve the electrostatic performance of the cell and to match the gains of the boundary cells to those of the cells in the inner layers. At the innermost boundary of layer 1 and the outermost boundary of layer 40, two clearing wires have been added per cell to collect charges created through photon conversions in the material of the walls.

A total of three different types of feed-throughs were required for the chamber to accommodate the sense, field, and clearing field wires. The three types are illustrated in Fig. 2.8. They incorporate crimp pins of a simple design which fasten and precisely locate the wires. The choice of the pin material (gold-plated copper for the signal wires and gold-plated aluminum for the field wires) and wall thickness in the crimp region was optimized to provide an allowable range of almost 150 μm in the crimp size as a primary means to avoid wire breakage.

2.4.3.3 Drift Isochrones

The calculated isochrones and drift paths for ions in adjacent cells of layers 3 and 4 of an axial superlayer are presented in Fig. 2.9. The isochrones are circular near the sense wires, but are deviated strongly from circles near the field wires. Ions originating in the gap between superlayers

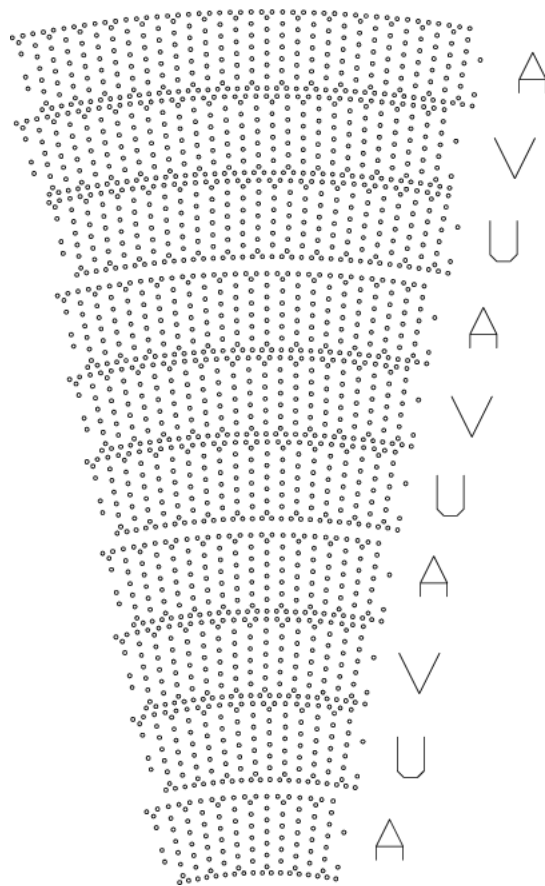


Figure 2.7. Arrangement of drift chamber wires. One sixteenth sector of the full chamber is shown, with axial (A) and small-angle stereo (U and V) superlayers indicated.

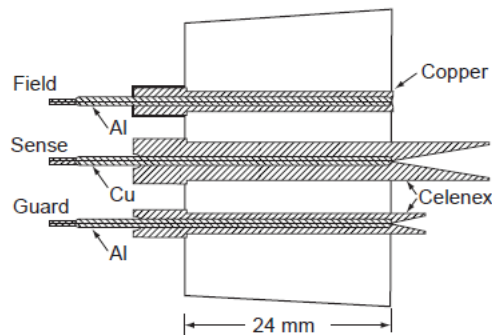


Figure 2.8. Design of three DCH wire feedthroughs for the 24 mm-thick endplates. The copper jacketed feedthrough is for grounded field wires, the other four are for sense wires (4.5 mm diameter), and guard and clearing field wires (2.5 mm diameter), all made of the Celenex insulator surrounding the crimp pins.

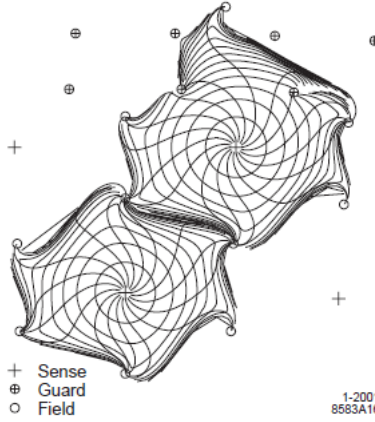


Figure 2.9. Drift cell isochrones, i.e. contours of equal drift times of ions in cells of layers 3 and 4 of an axial superlayer. The isochrones are spaced by 100 ns. They are circular near the sense wires, but become irregular near the field wires and are extended into the gap between the superlayers.

are collected by cells in the edge layers after a delay of several μs . These lagging ions do not affect the drift times measurements, but they contribute to the dE/dx measurement.

2.4.3.4 Cross Talk

A signal on one sense wire produces oppositely charged signals on the neighboring wires due to capacitive coupling. The cross talk is the largest between adjacent cells of adjacent layers, ranging from -0.5% at a superlayer boundary to -2.7% for internal layers within the superlayers. For adjacent cells in the same layer, the cross talk ranges from -0.8 to -1.8% , while for cells separated by two layers it is less than 0.5% .

2.4.3.5 Gas system

The drift chamber is operated with a gas mixture of 80% helium and 20% isobutane, passed through a bubbler to introduce 3500 ppm of water vapor. The bubbler also introduces approximately 100 ppm of oxygen into the gas mixture, which has a small effect on the avalanche gain. A recirculating pump maintains in the chamber a pressure of 4 mbar over atmospheric pressure; freshly mixed gas is introduced when necessary to compensate losses.

2.4.3.6 Drift chamber performance

Drift chamber project for $c\tau$ factory is similar to the BaBar one. Our choice stems from the fact that the performance of the BaBar drift chamber during six years of operation has been excellent. The momentum resolution is determined by reconstructing through-going cosmic ray events as two separate “tracks” and taking the difference in the fitted transverse momentum (the inverse curvature radius in the XY plane) in the center of the chamber as a resolution. The result is

$$\frac{\sigma(p_T)}{p_T} = (0.13 \pm 0.01)\% \cdot p_T + (0.45 \pm 0.03)\%$$

The single-hit position resolution is determined for all tracks from comparison of the fitted trajectory excluding each measured hit with the position of the hit determined from the readout

timing and the calibration time-to-distance relation for that cell. The result (Fig. 2.10) is a weighted-average resolution of $125 \mu m$ over all cells; in the region of each cell with the most uniform electric field the resolution reaches $100 \mu m$.

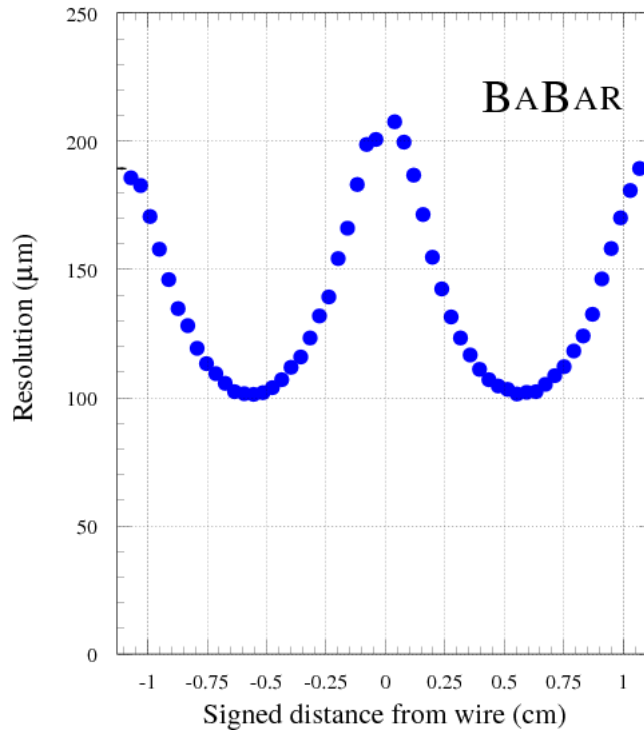


Figure 2.10. BaBar single-hit resolution vs. distance from the sense wire. The resolution is computed from the residual of the hit position compared with the fitted track excluding that hit. The sign of the distance is positive (negative) for tracks passing to the right (left) of the radial vector to the sense wire.

The drift chamber readout system includes both timing, with 1 ns precision, and integrated charge information. The detector is calibrated for the electronics gain of each channel, normalized to the charge deposition and avalanche gain as a function of the track trajectory in each layer of the chamber. With these calibrations, the integrated charge from each hit can be used to compute the relative energy loss; the ionization energy loss dE/dx for each track is computed from the 80% truncated mean of the hits assigned to the track, as shown in Fig. 2.11. For electrons from radiative Bhabha events $\sigma(dE/dx)/(dE/dx) \leq 7.5\%$ is obtained.

2.5 FARICH system

2.5.1 Introduction

Excellent particle identification (PID) for hadrons and leptons over the full momentum range for particles coming from charm and τ decays is essential to achieve the physics objectives of the experiment. In particular, a search for lepton flavor violation in the decay channel $\tau \rightarrow \mu\gamma$ with a sensitivity to the branching fraction of 10^{-9} requires a good μ/π separation for 1 GeV/ c particle momentum. Another example is a search for CP violation in D decays, which needs full particle identification to reconstruct exclusive final states and tag the flavor of the other D meson in the event.

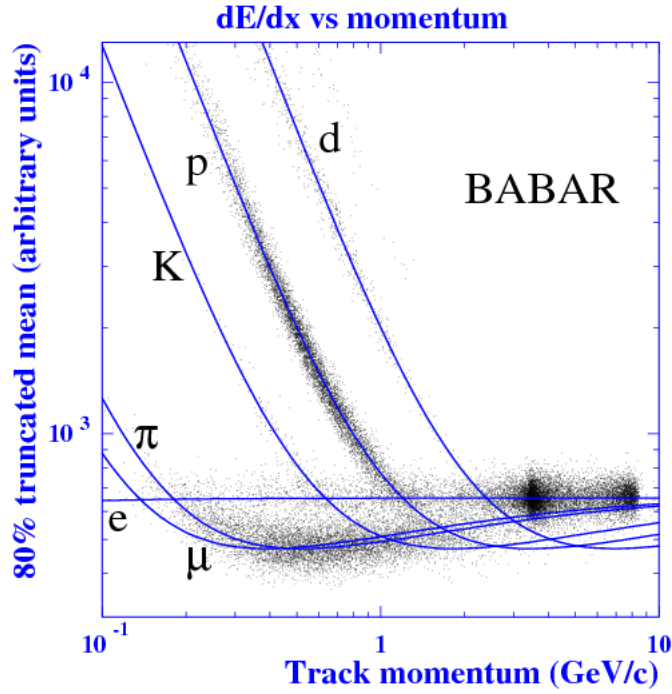


Figure 2.11. dE/dx distribution vs momentum for particle samples.

Identification of leptons is performed by the electromagnetic calorimeter and the muon system, while the energy losses in the drift chamber (dE/dx) can be used to identify charged hadrons. However, the latter technique cannot discriminate between pions and kaons with momenta above $0.7 \text{ GeV}/c$. Identification of muons with momenta below $1 \text{ GeV}/c$ is a hard task for the existing muon range detectors. For example, the efficiency of the BaBar detector for muons with $1 \text{ GeV}/c$ momentum was 64% while the pion misidentification rate was 2% (2.4σ separation) [7]. The KLM system of the Belle detector has a better performance with a 78% muon efficiency and 2% pion misidentification rate (2.8σ separation) at a $1 \text{ GeV}/c$ momentum [8].

For particle identification in the experiments at $c\tau$ factory a novel Ring Imaging Cherenkov counter with a *focusing* aerogel radiator (FARICH) is proposed. It is able to provide high μ/π separation below and about $1 \text{ GeV}/c$, as well as excellent $\pi/K/p$ separation for high momenta not covered by dE/dx measurements. Section 2.5.4 reports the results of FARICH performance for MC simulation.

Silica aerogel is a porous silicon dioxide with a variable index of refraction ($1.006 \div 1.2$), which is applicable in Cherenkov detectors for particles with a few GeV/c momentum.

The first RICH detector using silica aerogel as a Cherenkov radiator was successfully employed in the HERMES experiment [9]. Later it was followed by RICH1 of the LHCb detector [10]. Both RICH detectors use gas as a second radiator and focusing mirrors to form Cherenkov ring images on a photon detection plane.

A RICH with proximity focusing uses the gap between a layer of radiator medium and photon detector to make a ring image. This allows one to construct more compact RICH detectors as compared with a RICH with focusing mirrors. This design was implemented in the RICH with the dual aerogel-NaF radiator for the upcoming ISS-born experiment AMS-02 [11]. Besides that, the PID system based on proximity focusing dual layer aerogel Cherenkov radiator for the end-cap of the Belle-II detector at Super KEK-b collider in Japan is under development and construction now. The thickness and the refractive index of the layers are adjusted in the way that the Cherenkov

rings from different layers overlap very well in the photodetector plane (200 mm). First beam test results are in good agreement with calculation and simulation [21].

2.5.2 FARICH concept

In a proximity focusing RICH, one of the main factors limiting the Cherenkov angle resolution is the finite thickness of a radiator. In [12, 13, 14] it was proposed to use a radiator consisting of several layers of aerogel with different refractive indices to overcome this limitation. The index of refraction and the thickness of each layer are chosen so that the rings from all layers coincide in the photon detection plane. Another possibility is to have several separate rings (Fig. 2.12). Both options allow one to diminish the photon emission point uncertainty. We call a detector employing this technique a Focusing Aerogel RICH (FARICH).

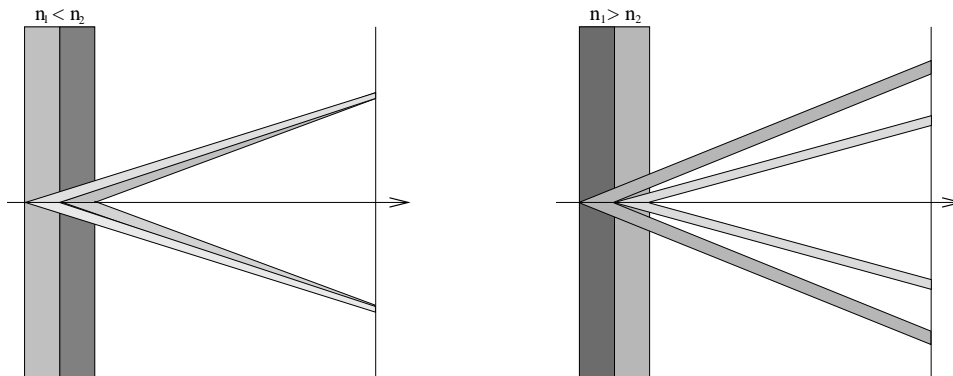


Figure 2.12. FARICH in single-ring (left) and multi-ring (right) alternatives.

In 2004 the first multilayer aerogel sample has been obtained in Novosibirsk [13]. Four layers of that aerogel had indices of refraction and thicknesses that match the designed ones with a good precision. At present, we have several aerogel tiles in a single-ring option with 2–4 layers with dimensions of up to $115 \times 115 \times 40 \text{ mm}^3$.

2.5.3 Design

The FARICH for SCTF should cover almost a 4π solid angle and identify muons and hadrons with momenta of up to approximately $2 \text{ GeV}/c$. The FARICH will work in a magnetic field of 1 T, which imposes a serious limitation on the photon detector choice. Presently, the only existing single photon detector sensitive to the visible spectrum that is able to work in a strong magnetic field of arbitrary direction is the multipixel Geiger-mode avalanche photodiode (MPGM-APD or SiPM) [25]. The SiPM is almost insensitive to a magnetic field, has a gain of the order of 10^6 , a high photon detection efficiency (PDE) in the visible region, a low voltage bias and a size of a few mm. There are two types of SiPMs today. The silicon photomultiplier is called a Digital SiPM (DSiPM) when part of digital electronics such as time-to-digital converter (TDC), memory blocks or something else are integrated with photon sensor in one chip [26, 27, 28]. In this case the geometrical efficiency becomes worse because each element and photo sensitive area are placed on one side of the crystal. The best geometrical efficiency (69%) and thus the photon detection efficiency (PDE) of about 30% for such DSiPMs was achieved with the Philips PDPC design which includes 2 TDCs connected with four $4 \times 4 \text{ mm}$ size pixels. The major concern was that rather big dead-time of the TDCs limits the level of operable sensor loads and work in single photon

counting mode with these devices is possible only with sufficient suppression of intrinsic noise level, for instance by decreasing temperature. The other type is Analogue SiPM single pixels or their arrays. The most known manufacturers of the devices are Hamamatsu (Japan) [29], FBK (Italy) [30] and SensL (Ireland) [31]. The main parameters (PDE, dark count rate (DCR), and probability of optical crosstalks) of the recently designed SiPMs from these manufacturers are very close. A comparison of these devices is presented in [32]. The level of DCR for all modern SiPM designs is less than 100 CPS/mm² at room temperature, and the PDE in peak achieves a value of 40÷50%. Several comparisons of Digital SiPM and Analogue SiPM are given in [33]. The main limitation of their usage in the particle collider experiments is their low radiation resistance [34, 35]. Several investigations have shown that after a cumulated dose of about 10¹⁰n_{eq}/cm² the SiPM DCR increases two times. It could lead to distortion of the Cherenkov ring reconstruction process and additional loads of the data transfer system.

Other candidates as the photon detectors are photomultiplier tubes with microchannel plates (MCP PMT) and hybrid avalanche photodiode (HAPD). The main advantages of MCP PMT in comparison with SiPM are their good radiation hardness and low level of intrinsic noises (100 kcps/cm²). MCP PMTs are able to work in parallel magnetic fields without degradation of efficiency and at a tilt 45° to a magnetic field of 1 T the collection efficiency of photoelectrons decrease in two times only [36]. For the Aerogel RICH (ARICH) system of the Belle-II detector, the photon detection plane is based on HAPDs. One segment of the system, based on two layers of aerogel (20 mm with refractive index n=1.045 plus 20 mm with n=1.055) and HAPDs, was tested on a beam. For the relativistic particle 8.6 photoelectrons were emitted and angle resolution per track $\sigma_t = \frac{\sigma_\theta}{\sqrt{N_{pe}}} = \frac{15.6}{\sqrt{8.6}}$ mrad was obtained [21]. The possibility to work with an HAPD in a parallel magnetic field of 1.5 T was demonstrated too. Radiation hardness tests show that the HAPDs are able work at an integrated neutron dose up to 10¹²n_{eq}/cm², which is the estimation of the integrated neutron dose after collecting of 70 ab⁻¹ in the Belle-II experiment. MCP PMTs and HAPDs are very promising candidates for the end-cap parts of the FARICH system for the cτ factory in Novosibirsk (Russia).

The suggested FARICH layout is shown in Fig. 2.13. It consists of the barrel and endcap parts. The solid angle of the system is 98% of 4π. The radiator has an area of 17 m²; photon detectors, of 21 m². The number of SiPMs and electronics channels is about one million.

The very large number of channels and their high density will require development of dedicated front-end electronics based on ASICs. The digitizing part (TDC) should be located right in the detector. A lot of specialized chips for SiPM arrays readout have been developed: NINO [37], MAROC, SPIROC [38], PETA [39], BASIC [40], VATA64HDR16 [41] and TOFPET [42]. Generally, they were developed for Positron Emissive Tomography (PET) or for other application with fast scintillation crystals (LYSO, LaBr3 and other). Some of them such as NINO and VATA64HDR16 will be used for Cherenkov light registration from quartz. For example, NINO is a amplifier-discriminator, which in couple with fast TDC (i.e. HTDC) provides registration of signals with picosecond time resolution. This chip was also tested with MCP PMT within the frame of the development of the particle identification system TORCH for the LHCb detector at the Large Hadron Collider (LHC) [43]. The other above chips are very complex devices able to determine the photon position (pixel number) and the amplitude and time of the signal. It takes a lot of time to transfer this information through the data acquisition (DAQ) system. So it is impossible use these chips with event rates higher than 100 kHz and therefore are not applicable for the SCTF project, where a rate of events in the DAQ system of about 300 kHz is expected. In the FARICH system only a few detected photons per track are expected and there is no necessity to determine the signal amplitudes in each channel because it will be not more than one photo-

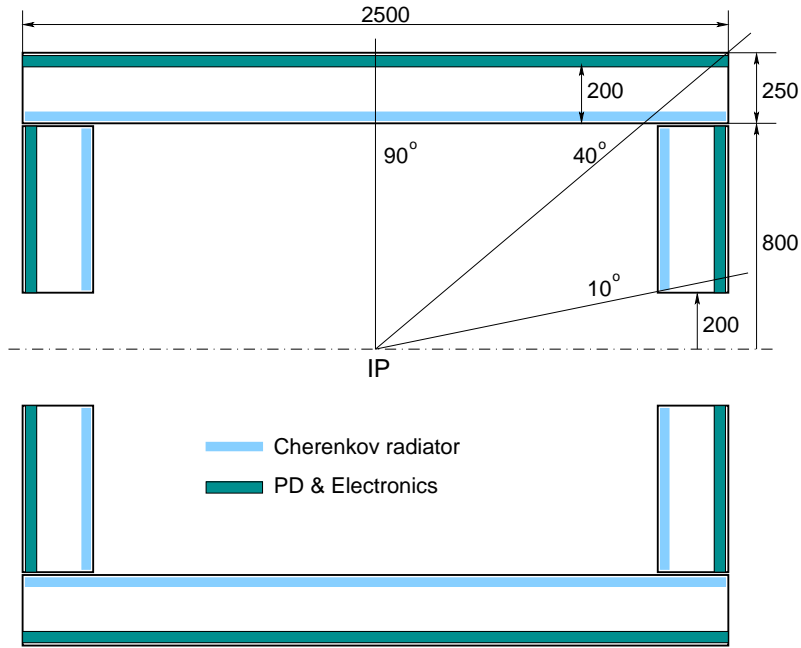


Figure 2.13. FARICH PID system for the SCTF.

electron amplitude. One of the possible ways to develop the electronics for the FARICH system is to modernize some of existing chips, improving their transfer capability and abandoning the amplitude measurements.

2.5.4 MC performance

The following configuration of FARICH is considered and studied using a Geant4-based Monte Carlo simulation program:

- the distance between the radiator and photon detector of 200 mm,
- a single-ring four-layer aerogel radiator with a total thickness of 35 mm and $n_{\max} = 1.07$,
- a photon detector — MPPC (Hamamatsu Photonics) with a $3 \times 3 \text{ mm}^2$ active area, $\text{PDE}(500\text{nm}) = 30\%$ and packing density 53%.

The simulation takes into account the processes of radiation, absorption and scattering of the Cherenkov light. The interactions of charged particles with matter were proved to be negligible (except for multiple scattering at momenta below $0.5 \text{ GeV}/c$) and are not simulated. A magnetic field of 1 T is included in the simulation. The effects of the SiPM dark noise and detector background currently are not taken into account.

The simulation shows that the number of photoelectrons for a relativistic particle is about 25 (Fig. 2.14a), which is enough for a robust ring reconstruction. The velocity resolution reaches $5 \cdot 10^{-4}$ (Fig. 2.14b). Figures 2.14c,d demonstrate π/K and μ/π separation levels derived from the velocity resolution. The π/K separation is very good for momenta from the kaon Cherenkov threshold in aerogel ($1.3 \text{ GeV}/c$) and up to a few GeV/c . In an experiment, the π/K separation will be affected by other processes like kaon decays, photon detector noise, detector backgrounds, etc. The μ/π separation can be provided at a level $\geq 3\sigma$ from 0.4 to $1.7 \text{ GeV}/c$ particle momentum and range from 5.5 to 8σ at $1 \text{ GeV}/c$ momentum.

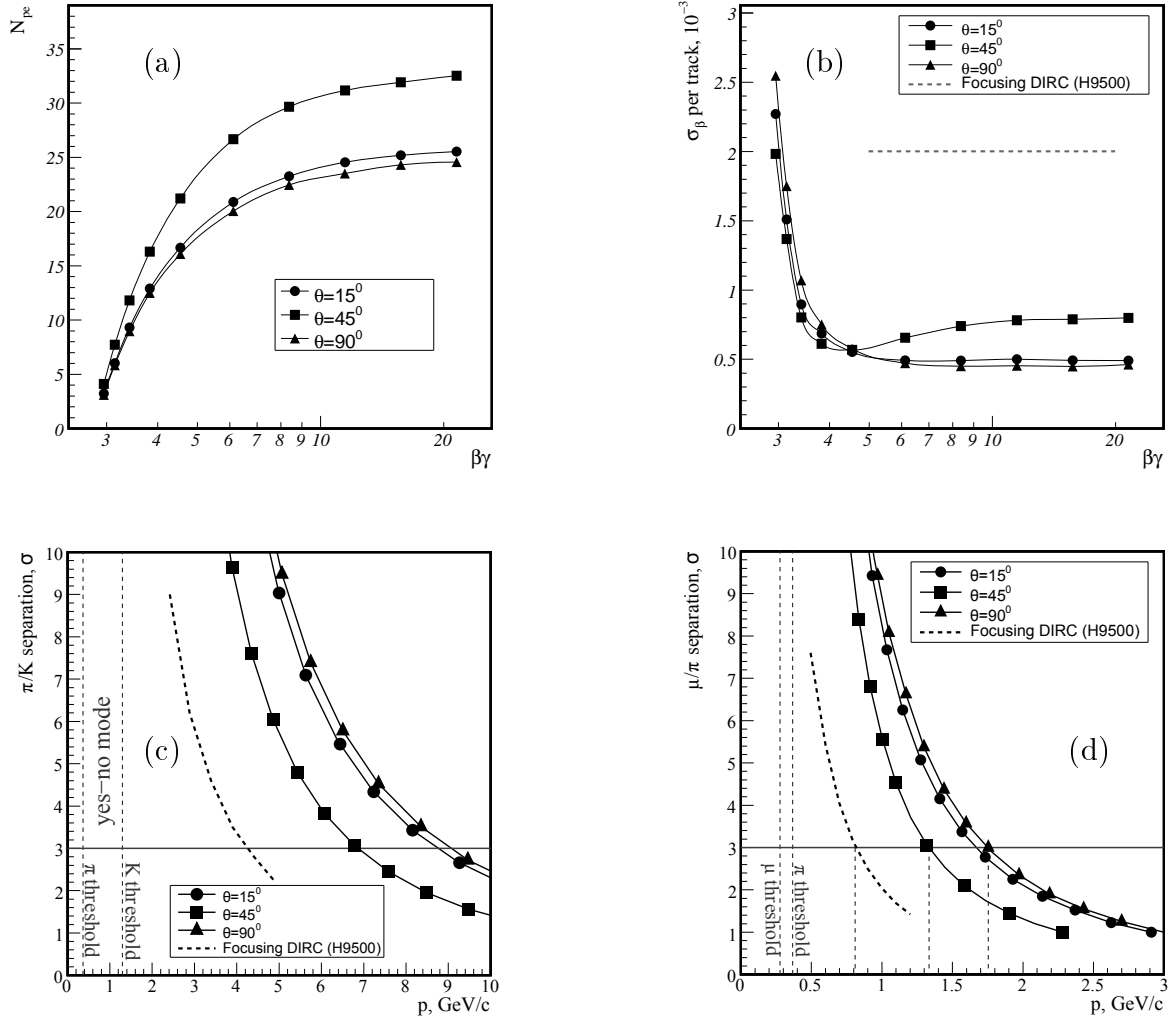


Figure 2.14. FARICH simulation results for three polar angles: the number of photoelectrons (a), velocity resolution (b), π/K (c) and μ/π (d) separations. Focusing DIRC performance is shown for comparison.

The development of DIRC upgrade with a focusing mirror and chromaticity correction (FDIRC) was made at SLAC [44]. The project of FDIRC for SuperB-factory in Italy (today the whole Italian project is closed) was developed. Several types of photodetectors were considered; the electronics design was suggested; the prototype tests with cosmic rays and hadron beams were performed [45].

π/K separation of the Focusing DIRC (FDIRC) is shown along with the FARICH performance in Fig. 2.14c. We calculated from these data the corresponding velocity resolution, which is $\sim 2 \cdot 10^{-3}$ (Fig. 2.14b) and the μ/π separation (Fig. 2.14d), which amounts to 2σ at a 1 GeV/c momentum.

The methods to cover the lower momenta are currently discussed and can be either a threshold mode of operation (“yes-no mode”) or employment of an additional radiator of higher index of refraction such as NaF crystal ($n = 1.33$).

2.5.5 First FARICH prototype tests

In 2011 the first test of the FARICH prototype at the installation “Extracted beams” at the VEPP-4M complex were performed [46]. 32 SiPMs from CPTA (Moscow) with a sensitive area of $2.1 \times 2.1 \text{ mm}^2$, 16-channel discriminator boards with built-in pre-amplifiers, and 64-channel multi-hit TDC V1190B (CAEN) with a 100 ps time tick were used for photon detection. At the beam test with 1.5 GeV electrons, the Cherenkov angle resolution for a single photon with a 4-layer aerogel sample was measured and the focusing effect in comparison with single layer aerogel samples was demonstrated [47]. In Fig. 2.15 the radial distributions of Cherenkov photons for two aerogel samples are shown: 4-layer aerogel with 30 mm thickness (a) and 1-layer aerogel with 20 mm thickness (b).

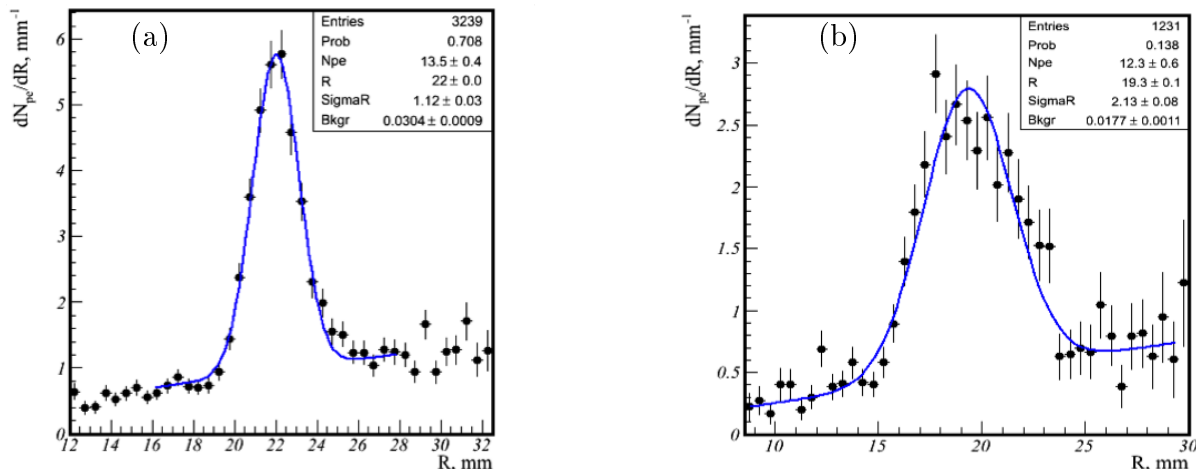


Figure 2.15. FARICH beam test results obtained with 1.5 GeV electrons. Cherenkov photon distribution on radius for 4-layer aerogel sample 30 mm thick (a) and 1-layer aerogel sample 20 mm thick (b).

The particle identification capability of the FARICH method was tested with hadron beams at CERN in 2012 [47, 48]. The prototype was based on a 4-layer aerogel sample with the maximal refractive index $n_{\max} = 1.046$ and dimensions $15 \times 115 \times 37.5 \text{ mm}$. A matrix of 24×24 of silicon “digital” photosensors DPC3200-22-44 Philips [26] with overall sizes $200 \times 200 \text{ mm}$ was used as a photon detector. Each sensor consists of four $3.2 \times 3.9 \text{ mm}$ pixels (in total 2304 pixels). The Cherenkov rings for different particles (p , K^\pm , π^\pm , μ^\pm , e^\pm) with pulses equal to 6 GeV/c are shown in Fig. 2.16a. In Fig. 2.16b the distribution of the same events on radius is presented. Distribution of events over the Cherenkov radius for particles with 1 GeV/c pulses is presented in Fig. 2.16c. The power of the μ/π -separation at a level of 5.3σ was obtained at a 1 GeV/c momentum, and π/K -separation better than 3.5σ until the momentum equals 6 GeV/c was observed. The obtained results demonstrate better particle identification FARICH capability in comparison with FDIRC (see Fig. 2.16d).

2.6 Electromagnetic calorimeter

Since a considerable fraction of the hadrons produced in the $c\tau$ factory energy range are π^0 's and other neutral particles providing photons in a wide energy range from 20 MeV to 2 GeV, a high resolution calorimeter is a very important part of the detector. The main tasks of the calorimeter are as follows:

- detection of γ -quanta with high efficiency,

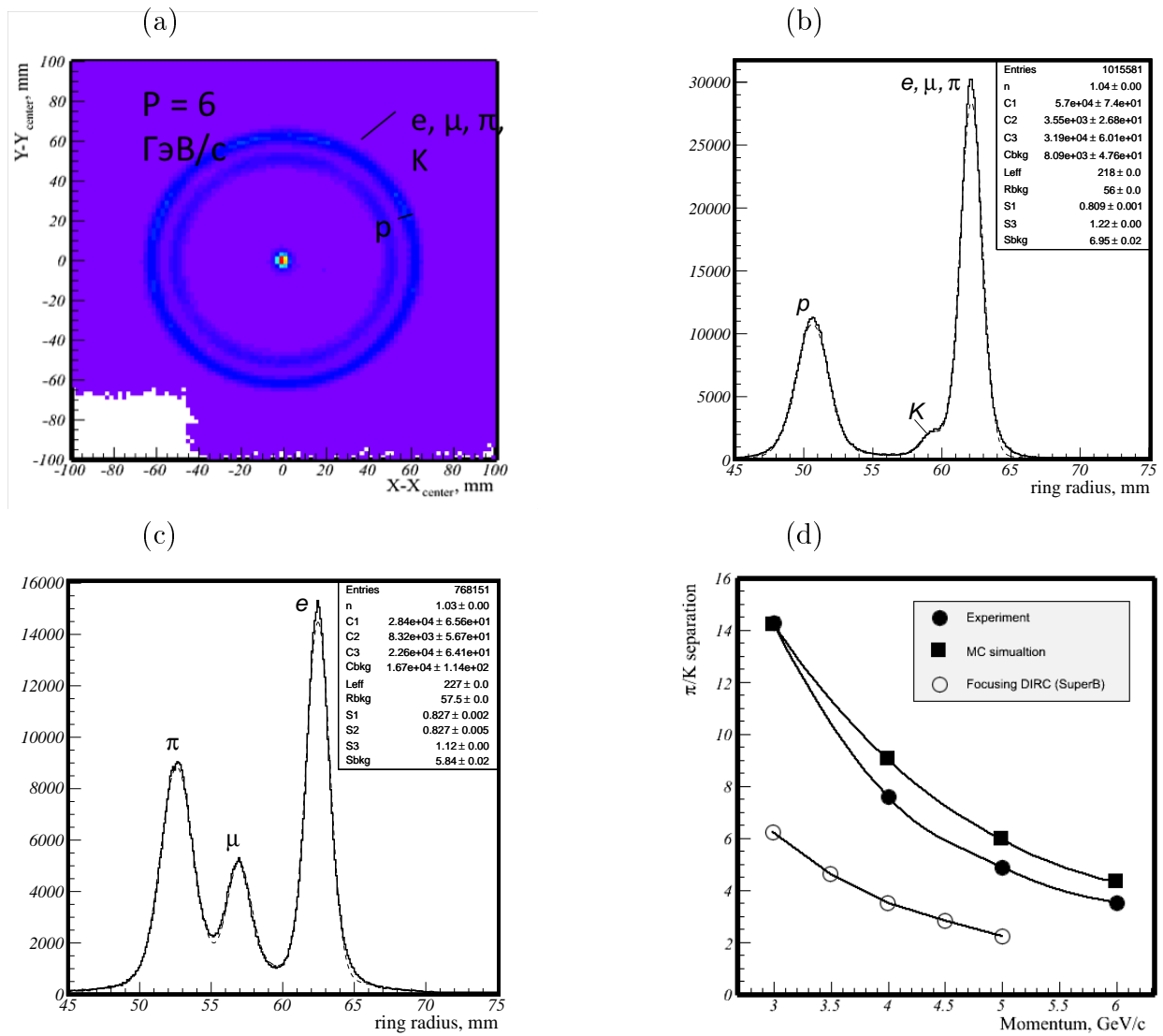


Figure 2.16. FARICH beam test results obtained with particles momentum $P = 1 \div 6 \text{ GeV}/c$: Cherenkov rings for particles momentum $6 \text{ GeV}/c$ (a), Cherenkov photon distribution on radius for particles momentum $6 \text{ GeV}/c$ (b), Cherenkov photon distribution on radius for particles momentum $1 \text{ GeV}/c$ (c), dependence of π/K -separation power in σ on momentum for prototype of FARICH (measurements and simulation) and FDIRC (measurements) (d).

- precise determination of the photon energy and coordinates,
- electron/hadron separation,
- K_L detection,
- generation of proper signal for the trigger,
- on-line and off-line luminosity measurement.

One of the most important tasks for $c\tau$ factory is a search for the lepton flavour violating decay $\tau \rightarrow \mu\gamma$. This decay mode has to provide a narrow peak in the $\mu\gamma$ invariant mass spectrum. The sensitivity to the mentioned decay strongly depends on the width of this peak, provided by the calorimeter energy and spatial resolution.

At present, the best energy resolution for photons in the energy range around 1 GeV and below is obtained with calorimeters based on scintillation crystals CsI(Tl) [65, 50], $\sigma_E/E \approx 1.8\%$ at 1 GeV and about 3% at 100 MeV. The space resolution of such calorimeters is about $6 \text{ mm}/\sqrt{E(\text{GeV})}$. It is also worth noting that Budker Institute of Nuclear Physics has large experience of developments, construction and exploitation of calorimeters based on scintillation alkali-halide crystals.

Other advantages of scintillation calorimeters are their high stability and low maintenance cost. CsI(Tl) crystals have a high light output (up to 50,000 photons/MeV) and emission spectrum with a maximum at about 550 nm well matching the region of high sensitivity of silicon photodetectors. An example of the high resolution electromagnetic calorimeter is the calorimeter of the Belle detector. It contains 8736 counters based on CsI(Tl) crystals of 30 cm length ($16.1 X_0$). Each crystal is equipped with two silicon PIN $20 \times 10 \text{ mm}^2$ diodes for light readout.

The preamplifier attached to the crystal is followed by the shaper boards placed in the crates around the detector; the digitizing and trigger modules are installed at the electronics hut. The shaper board contains a $CR - (RC)^4$ active filter with $\tau = 1 \mu\text{s}$ shaping time.

The average light output of the crystals was about 5000 photoelectrons/MeV, while the electronics noise level is about 1000 electrons, which corresponds to an energy noise equivalent (ENE) of about 200 keV.

The ten-year experience of CsI(Tl) Belle calorimeter exploitation in the B factory experiments demonstrated its high performance and reliability. The radiation resistance of the crystals is sufficiently high for the conditions of e^+e^- colliders. At the Belle detector, the total radiation dose absorbed by the crystals closest to the beam pipe was about 500 rad during the 10 years of operation. At $c\tau$ factory with a luminosity of $10^{35} \text{ cm}^{-2}\text{c}^{-1}$, the absorbed dose can reach about 1 krad after the 5 years of experiments. According to the measurements performed in [52], that results in about 20% loss of the light output only.

However, scintillation of the CsI(Tl) crystals is relatively slow with a decay time of about $1 \mu\text{s}$. This leads to a high probability of the pile-up of the background and useful signals at a high background counting rate (about 100 kHz or more per crystal). A natural solution of this problem is to use faster crystals. An example of such a material is non-activated (pure) CsI crystals, well known in high energy physics. The decay time of the pure CsI scintillation is about 30 ns.

Pure CsI characteristics are presented in Table 2.1 in comparison with the CsI(Tl) properties. Crystals of this type were proposed for the Belle II [53] endcap calorimeter, which is developed by

Table 2.1. Properties of pure CsI and CsI(Tl) scintillation crystals.

	$\rho, \text{ g/cm}^3$	$X_0, \text{ cm}$	$\lambda_{em}, \text{ nm}$	$n(\lambda_{em})$	N_{ph}/MeV	$\tau_d, \text{ ns}$	$dL/dT, \text{ \%}/^\circ (20^\circ\text{C})$
pCsI	4.51	1.85	305	2.0	2000-5000	20/1000	- 1.3
CsI(Tl)	4.51	1.85	550	1.8	52000	1000	0.4

the team of BINP physicists [54]. However, since the light output of pure CsI is approximately ten times lower than that of CsI(Tl), one has to use photosensors with an intrinsic gain and ability to operate in a magnetic field. The emission spectrum of pure CsI has a maximum at a wavelength of 310 nm, which puts additional requirements on the photosensor. In addition to the fast component of scintillation, a pure CsI crystal has a slow component with a decay time longer than $1 \mu\text{s}$. The ratio of the slow component of the scintillation light to the total amount of the light integrated over the first $1 \mu\text{s}$, referred usually as f/t ratio, is an important characteristic of this crystal. When pure CsI crystals are used in the high energy physics experiments, the requirement $f/t > 70\text{-}80\%$ is usually applied.

Taking into account the large experience of the BINP team on R&D with pure CsI crystals, the option of the calorimeter based on pure CsI is taken as a baseline for this project and the following sections of this chapter are mostly devoted to that. The technology of production of pure CsI crystals is well established at several crystal-growing companies such as Amcryst (Ukraine), Saint Gobain (USA), HPK (Japan-China), which enables production of the necessary crystal amount within 2-3 years.

In the last decade new crystal scintillators with high light output and short emission time are actively developed. Most promising materials are lutetium orthosilicate (LSO), lutetium aluminate (LuAP) and lanthane bromide (LaBr₃) doped with cerium. However, the cost of these crystals is quite high (5-10 times more expensive than CsI(Tl)) that makes problematic a use of a large amount of these crystals in experiments. On the other hand, active studies of the properties of the new crystals and the possibilities of their usage in the large experiments in close cooperation with crystal producers can improve the technology of their growth and make these crystals cheaper.

2.6.1 Calorimeter elements

Since the electromagnetic calorimeter of the detector for $c\tau$ factory should have high energy resolution for photons ($\sim 1.5\%$ at $E_\gamma=1$ GeV), the energy fraction deposited in the active material of the calorimeter should not be less than 95 % of the initial photon energy. To meet this condition the calorimeter thickness should be 16-18 radiation lengths, which corresponds to 30–34 cm for CsI. The lateral size of the calorimeter element is determined by the transverse shower development and for CsI it is usually taken as 4~7 cm. A smaller size of the element somewhat improves the spatial resolution, but results in increase in the total volume in the gaps between crystals and larger number of electronics channel.

An option of the calorimeter subdivision is shown in Fig. 2.17. The proposed calorimeter

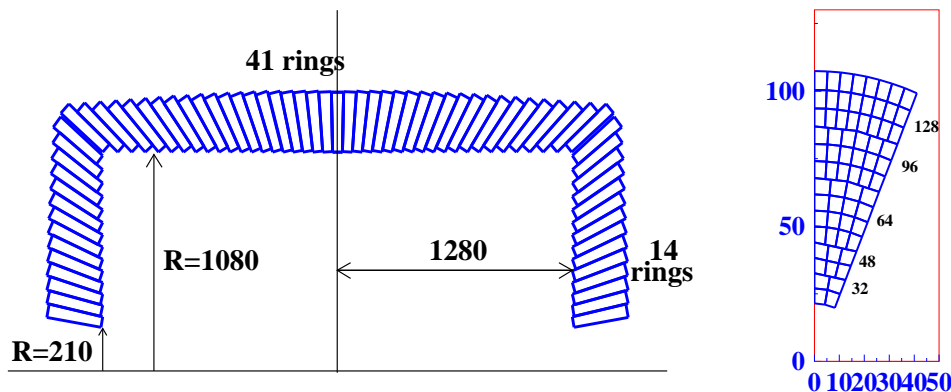


Figure 2.17. Disposition of the counters in the calorimeter: Z-projection (left), one sector of the endcap calorimeter (right).

consists of the barrel part and two end caps. The barrel includes 5248 counters arranged in 128 sectors with 41 crystals each. It gives 21 different geometry types of the crystals. The total mass of the crystals in the barrel is 26 (31) tons for a 30 (34) cm crystal length respectively.

The end cap calorimeter consists of 16 sectors, with 68 crystals each. The crystals in the sectors are arranged in 14 arc-layers as it is shown in Fig. 2.17. The crystal number in each layer

is shown in Table 2.2. The total mass of the crystals in each end cap is 5(6) tons for a 30 (34) cm crystal length.

Table 2.2. Arrangement of crystals in the endcap calorimeter.

layer number	crystals in the sector	crystals total	number of types
1	2	32	1
2	2	32	2
3	3	48	3
4	3	48	3
5	4	64	4
6	4	64	1
7	4	64	1
8	4	64	2
9	6	96	3
10	6	96	1
11	6	96	3
12	8	128	4
13	8	128	1
14	8	128	1
	68	1088	30

The calorimeter element (counter) is a pure CsI crystal wrapped with a 200 μm layer of white porous teflon as a diffusive reflector. The counter is covered by the outer layer of aluminized polyethylene 25+25 μm thick. Such a package provides sufficient light and electric insulation of the counters as well as high light collection efficiency at its good uniformity.

The light output of the pure CsI crystal has essential temperature dependence: -1.5%/centigrade. To achieve an energy resolution at a level of 1% one has to measure the temperature map inside the calorimeter with an accuracy of 0.1° and provide proper thermo-stabilization.

2.6.2 Photodetectors

Two alternative options for the scillation light readout are considered: based on the vacuum photopentodes (PP) as well as using the avalanche silicon photodiodes (APD).

2.6.2.1 Vacuum photopentodes

An option of photodetector that can operate in a magnetic field is the 2" vacuum photopentodes (PP) developed by Hamamatsu Photonics. Such a photopentode is shown in Fig. 2.18. The

photopentodes has small anode capacity (10 pF), gain factor of 150-250 without magnetic field, and quantum efficiency of 15-25 % in the wavelength range around 310 nm.

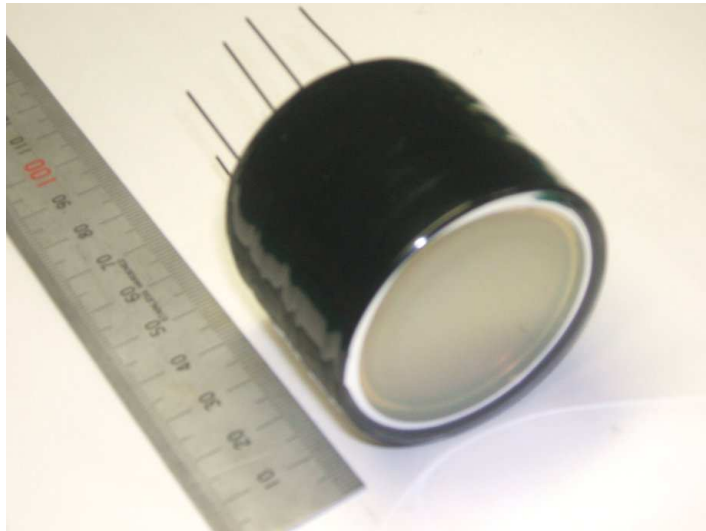


Figure 2.18. 2" vacuum photopentode R2185UV-MOD2 (Hamamatsu Photonics).

The voltage dependence of the photopentode gain is close to linear as shown in Fig. 2.19 a. The PP gain depends on the value of the axial magnetic field as shown in the Fig. 2.19 b. For a magnetic field of 1.5 T, the gain factor drops down approximately 3.5 times. The dependence of the gain factor on the angle between the magnetic field and PP axis has been measured and it is shown in Fig. 2.19 c. The PP gain factor is sufficient up to about 45°; for angles of 20-30° the PP signal even increases to 20 %. A counter based on the pure CsI crystal (with the Belle counter

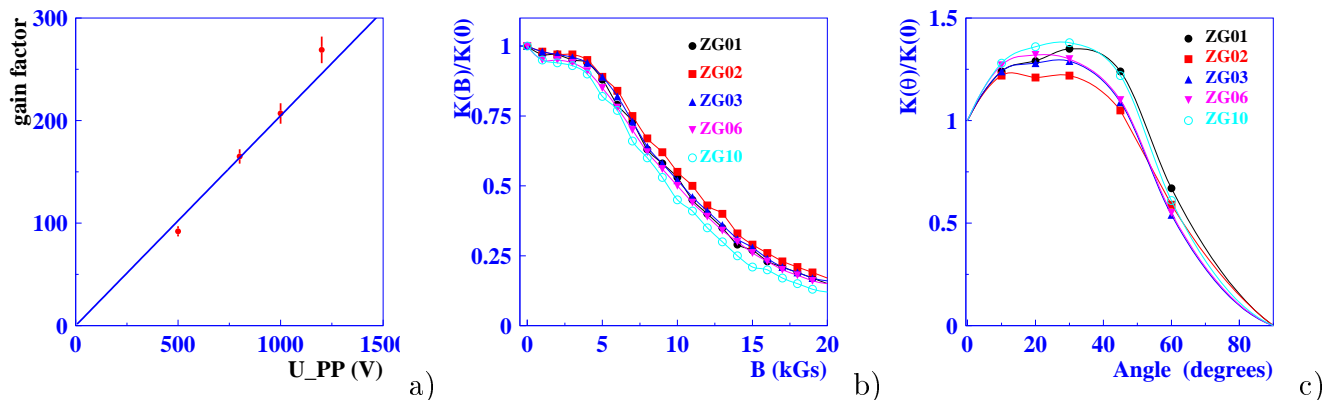


Figure 2.19. a) PP gain–voltage characteristic. b) The PP gain versus the magnetic field, parallel to the PP axis. c) PP signal in dependence on the angle between the magnetic field vector and PP axis. $B=1.5$ T. $U=1000$ B.

size) with PP readout without magnetic field has an ENE of about 50 keV, which, according to our measurements, corresponds to 170 keV in a magnetic field of 1.5 T.

The calorimeter is supposed to work in the heavy radiation conditions during about 10 years and the PP performance and characteristics should not change considerably. From this point of view, the long term stability of the gain factor and quantum efficiency at the full anode charge are

very important. For the stability studies two counters based on pure CsI and PP were constructed. In three years, the regular measurements of the cosmic ray spectrum were performed with these counters and the peak position was determined. No changes at a level of 3 % have been found. A special test bench was developed to study the dependence of the PP signal amplitude on the integrated anode charge. The light background on the PP photocathode was generated by a LED. A cosmic particle spectrum was accumulated, and the peak positions corresponding to the minimum ionizing particles crossing the crystal were monitored. The measurements show a small linear increase (about 10 %) of the signal with anode charge growth which stabilizes when the charge reaches 15 C. The measurements were carried out up to 140 C, which is 5 times larger than the expected accumulated charge for $c\tau$ factory operation.

2.6.2.2 Silicon avalanche photodiodes

The light readout scheme with vacuum PPs has some disadvantages. The most important of them are the large sizes of PPs and the necessity to orientate them within a small ($< 45^\circ$) angle relative to the magnetic field direction. The latter requirement is not a problem for the end cap calorimeter part, but it demands a special solution for the barrel. One of the options is the usage of the special prism-shape light guides, which, however, decreases considerably the light collection efficiency and makes the design much more complicated. It should be noted that the photosensors will be practically inaccessible during all the period of the experiments, which requires high reliability of all elements of the light readout. For example, in the calorimeter of the Belle detector each crystal is equipped with two independent readout channels with a silicon PIN photodiode and a charge-sensitive preamplifier. As a result, in spite of almost 20 years after the calorimeter construction, all 8736 counters are working, only one of the two channels is working in somewhat five counters. Such a scheme is not possible in case of the light readout option based on the vacuum PP.

At present the alternative light readout scheme using wavelength shifting plates (WLSP) and silicon avalanche photodiodes (APD) is under study. The APD working gain factor can be 50-100 and independent from the magnetic field. Performed studies of this option demonstrated a good characteristics as well as a possibility of its realization [56].

A scheme of the counter with WLSPs and APDs studied in the mentioned work is presented in Fig. 2.20. The WLS plate with the maximum absorption spectrum close to the pure CsI maximum emission of the fast component ($\lambda_{max} \approx 320$ nm) [57] is attached without optical contact to the large edge of the pure CsI crystal. Absorbed light is re-emitted in the range of around 600 nm where the APD quantum efficiency is about 80 %. This light is measured by four APD of the Hamamatsu S8664-55 type with a sensitive area of 5×5 mm² attached with the optical contact to the back plane or side surface of the WLSP as shown in the Fig 2.20.

The measured spectrum of the cosmic ray energy deposition obtained with such counter based on $6 \times 6 \times 30$ cm³ pure CsI crystal is presented in Fig. 2.21,a. The peak energy deposition corresponds to somewhat 33 MeV. The width of the distribution is defined by the angular and energy distribution of the cosmic rays as well the ionisation losses fluctuations. The electronics channel was calibrated in the units of the electron-hole pairs number produced in the APD before amplification. A gain of 50 was chosen. Taking into account the mentioned values it was found that the signal level before amplification is about 110 photoelectrons per 1 MeV for option a) (Fig. 2.21) and about 150 phe/MeV for option b). At this signal level, the photoelectron statistics does not contribute to the calorimeter energy resolution even after taking into account the excess noise factor (≈ 2.5).

The ENE values depending on the shaping time are presented in Fig. 2.21,b. For option b)

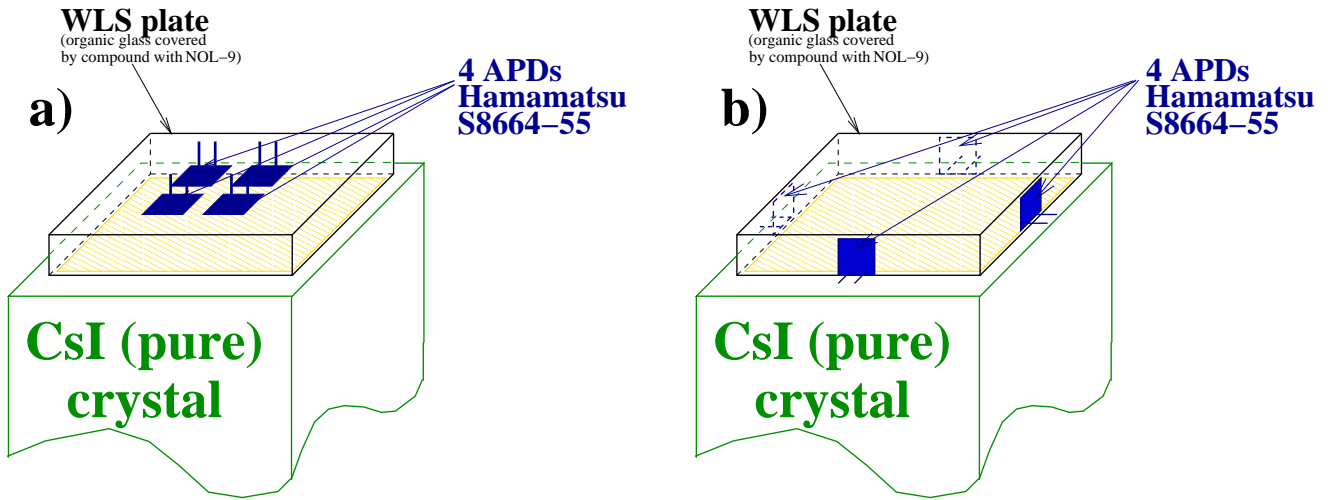


Figure 2.20. Two design options of the light readout using wavelength shifting plates (WLSP) and silicon avalanche photodiodes (APD).

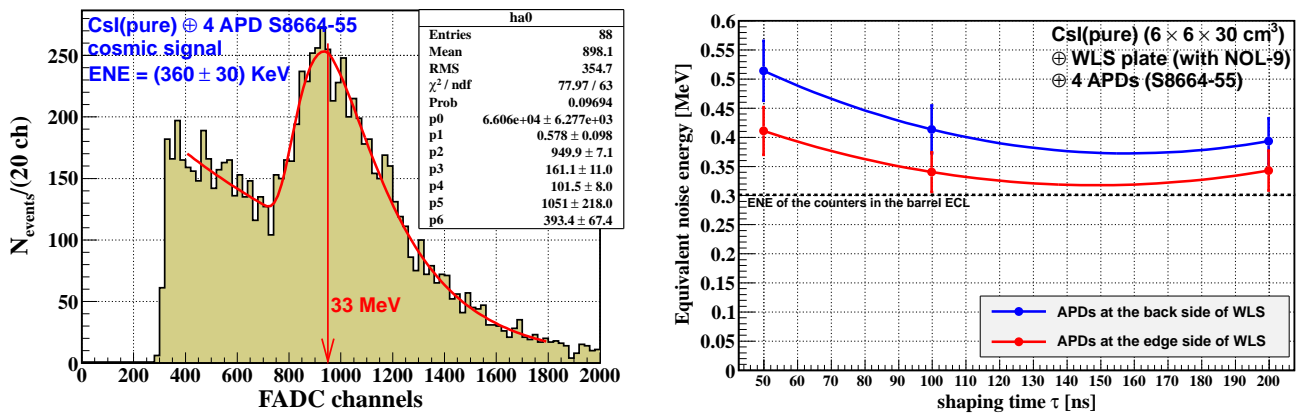


Figure 2.21. a) Measured spectrum of cosmic ray energy deposition obtained with the counter based on pure CsI crystal. WLSP and four APD are used for the light readout. b) Measured energy noise equivalent (ENE) in dependence of the signal shaping time. The dashed line shows the noise level for the BelleII calorimeter based on CsI(Tl) crystals and the shaping time of 500 ns.

and a shaping time of $\tau_s=50$ ns, the ENE is about 0.4 MeV, while at the minimum, $\tau_s=150$ ns, it is about 0.32 MeV. Such a noise level does not provide any considerable contribution to the calorimeter energy resolution.

It should be noted that to achieve high stability of the gain the APDs need precise stabilisation of the temperature (not worse than 0.1°) and bias voltage (not worse than 10 mV). However, this problem was solved for a very large number of APD channels in the electromagnetic calorimeter of the CMS detector [58]. This experience can be used for the APD option of the calorimeter of the $c\tau$ factory.

2.6.3 Calorimeter electronics

The calorimeter electronics layout is shown in Fig. 2.22 [59]. The photodetector signal is applied

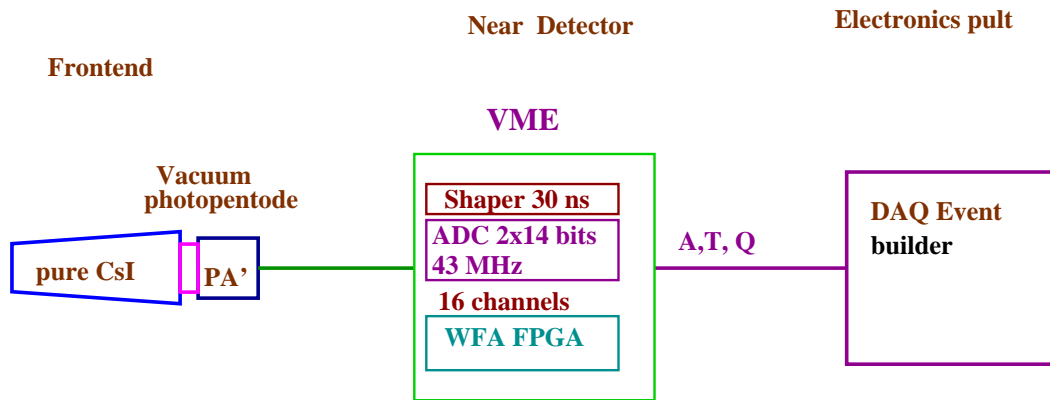


Figure 2.22. Calorimeter electronics layout.

to the charge sensitive preamplifier (CUSP) mounted on the counter. The CUSP has a paraphase output connected to a shaper-DSP module. The shaper-DSP modules are located in VME crates nearby the detector; each module serves 16-24 counters. Every channel contains a differentiation and four integration stages with a shaping time of 30 ns and two 14-bit flash ADC. The ADCs sampling frequency is 40 MHz. Two ADC are used to extend the dynamical range of the channel; they are connected directly to the shaper and with eight-fold attenuation. It enables a bin width of 50 keV for a maximum signal of 2 GeV.

After a trigger signal comes, ADC data of 16 channels are recorded to the buffer of the FPGA. 31 amplitudes are recorded for each channel within the trigger time. The FPGA algorithm provides rejection of the signals with an amplitude lower than the processing threshold and performing the fitting procedure to calculate the signal amplitude and time. The fitting is performed in three iterations in integer calculations according to the algorithm presented in Fig. 2.23. The last iteration provides the quality of the fit. The reconstructed zero level, amplitude, time and fit quality together with the number of the calorimeter channels are packed and send to the DAQ system of the detector if the pulse height exceeds a certain threshold. Such electronics provide readout with a trigger rate of 30 kHz with 30 % latency.

2.6.4 Pure CsI radiation resistance

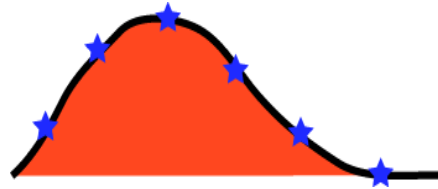
The radiation resistance of crystals is a very important issue from the point of view calorimeter reliability and performance during long term experiments. That is why we performed two studies

Algorithm details

$$\chi^2(A, p, t_0) = \sum_{i,j} (y_i - Af(t_i - t_0) - p) S_{ij}^{-1} (y_j - Af(t_j - t_0) - p) \rightarrow \min$$

$$S_{ij} = \overline{(y_i - \bar{y})(y_j - \bar{y})}$$

$f(t)$ – counter response



$$Af(t_i - t_1 - \Delta t) = Af(t_i - t_1) - A\Delta t f'(t_i - t_1) = Af(t_i - t_1) + Bf'(t_i - t_1)$$

where t_1 – initial time (trigger time)

$$\left\{ \begin{array}{l} \sum_{i,j} f_i S_{ij}^{-1} (y_j - Af_j - Bf'_j - p) = 0 \\ \sum_{i,j} f'_i S_{ij}^{-1} (y_j - Af_j - Bf'_j - p) = 0 \\ \sum_{i,j} S_{ij}^{-1} (y_j - Af_j - Bf'_j - p) = 0 \end{array} \right. \Rightarrow \begin{array}{l} A = \sum_i \alpha_i y_i \\ B = \sum_i \beta_i y_i \Rightarrow \Delta t = -B / A \\ p = \sum_i \gamma_i y_i \end{array}$$

Figure 2.23. The algorithm of the amplitude and time reconstruction.

of the radiation resistance of the pure CsI crystals with the sizes and shapes of real counters [60] and [61]. At BINP the crystals were exposed to a wide aperture beam of bremsstrahlung photons produced in a Pb(Mo) converter by a 1.4 MeV electron beam from the industrial accelerator ELV-6. The accumulated dose was measured by a counter based on same active material, CsI(Tl) crystal, which makes recalculation of the dose simpler and clearer.

The relative light output was measured using a collimated ^{137}Cs radiative source, which could move along the crystal axis. The crystal scintillation spectrum was detected with a PM tube and digitized with an ADC. The scheme was calibrated with a reference crystal, which was not irradiated.

Since the light output of pure CsI has strong temperature dependence, the temperature of the crystal was measured and corrections were implemented. The accuracy of the light yield measurement after correction was 1.5-2 %.

In the first study [60], four crystals and one counter based on a pure CsI crystal with PP readout were irradiated.

The dose rate was controlled by the accelerator current and was measured by a special dose counter, a small $1 \times 2 \times 2 \text{ cm}^3$ CsI(Tl) crystal. The light from this crystal was detected by a PIN diode coupled with the crystal with optical grease. The PIN diode current is proportional to the light intensity from the crystal or the energy deposition rate, which is the dose rate.

Series of irradiations with dose ranges from 250 to 30000 rad were carried out. Before and after irradiation, everyday measurement of the crystals and counter light output was performed. The counter lightoutput time dependence is shown in Fig. 2.24,a The figure shows an essential light output decrease just after irradiation and its partial recovery within a few days after irradiation. A similar dependence was observed for all counters. The resulting value of the light output was used to obtain the dependence of the light output on the accumulated dose shown in Fig. 2.24,b. As seen from the figure, the 15 krad of absorbed dose results in a light output loss of less than 15 %

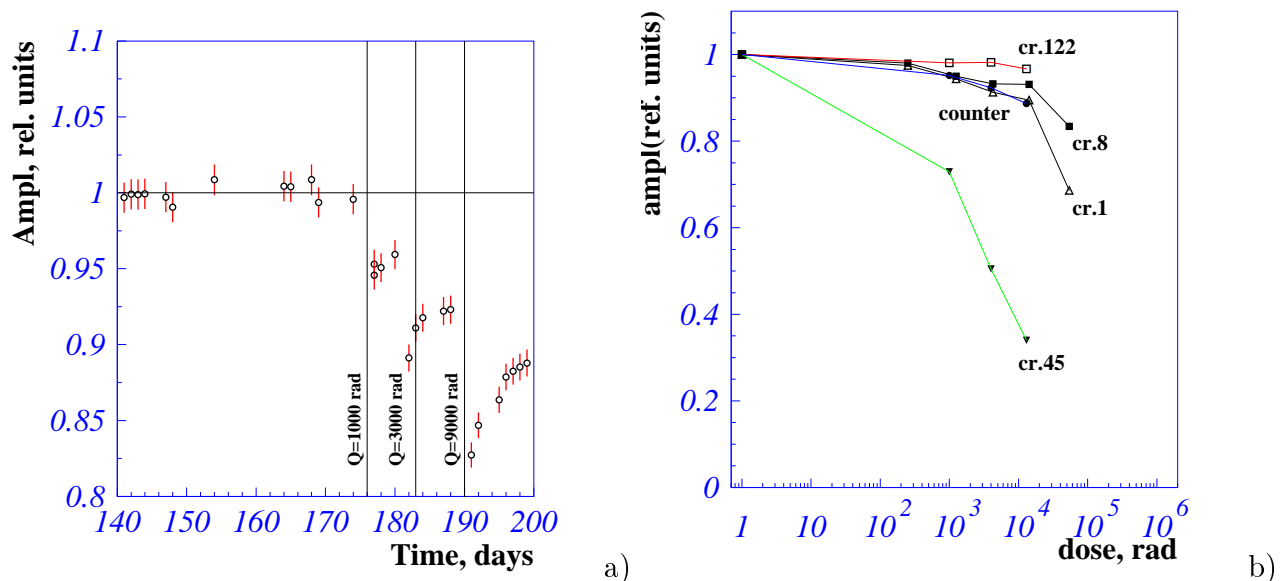


Figure 2.24. a) Lightoutput time dependence of assembled counter; b) Light output for four studied crystals.

for 3 crystals, while one of the crystals has much worse radiation resistance and is good enough. The presence of crystals with poor radiation resistance requires development of a special procedure to reject such crystals. No changes in the f/t -ratio were found within 3 % accuracy.

In a later work [61], we studied 15 full size samples produced with various modification of the growing technology. Part of these crystals had satisfactory scintillation characteristics (light output and f/t -ratio), while others did not satisfy the requirements on these parameters. In this work, strong correlation between the scintillation characteristics of the crystal and its radiation resistance was observed. It was shown that crystals with high light output and good f/t -ratio have good radiation resistance as well.

2.6.5 Measurements with calorimeter prototype

To study the calorimeter performance a prototype of 20 counters based on pure CsI crystals was prepared. The prototype was irradiated at a photon beam of ROKK – 1M at VEPP – 4M collider at BINP, Novosibirsk [54, 62]. The crystals had sizes of the modules of the Belle calorimeter and had been produced by AMCRIS company. The light readout was performed by vacuum phototetrodes. Each counter was packed according to the description in section 2.6.1. On the large end-side of the crystal, a phototetrode was attached with optical grease and fixed together with the voltage divider and preamplifier board. The light output of the crystals corresponded to 150-200 photoelectrons from the PP photocathode and $f/t > 50\%$. The counter layout is shown in Fig. 2.25. Special electronics in the CAMAC module was developed for readout of phototetrode

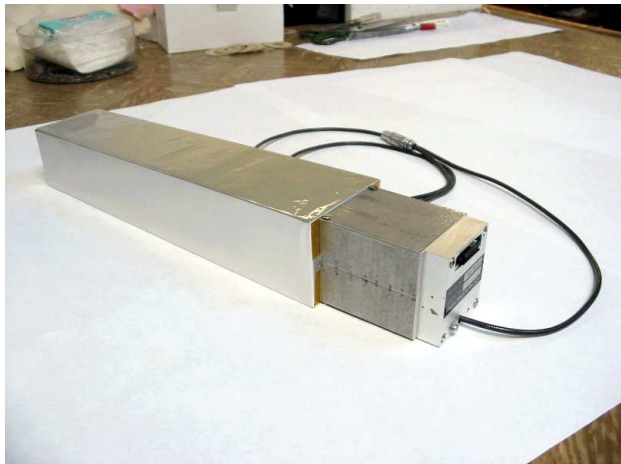
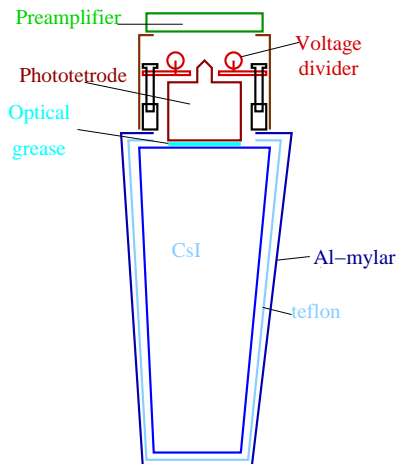


Figure 2.25. Counter layout and picture.

signal. Conceptually the module corresponds to the electronics described in section 2.6.3. The produced counters were calibrated on the cosmic rays. The energy noise equivalent was determined from the pedestal width and corresponded to 43 keV.

The pile-up noise value was measured in dependence on the background rate for the assembled counter and Belle detector CsI(Tl). The pile-up noise was simulated by γ -quanta of ^{60}Co radiative source (1.17 MeV and 1.33 MeV). The photon rate was varied via change in the distance from the counters to the radioactive source. Figure 2.26 shows the scheme of the measurement and results of comparison of the total noise level for the pure CsI and CsI(Tl). The results are in agreement with the simple estimation obtained from the decay times ratio $\sqrt{\tau_{Tl}/\tau_{pure}} = \sqrt{1000\text{ ns}/30\text{ ns}} \approx 5.5$.

For the beam test, twenty counters were assembled in a 4×5 matrix imitating endcap calorimeter part as shown in Fig. 2.27.

The prototype was irradiated by the photon beam of ROKK – 1M on the VEPP – 4M collider at BINP. Laser UV photons with the energy $\omega_0 = 2.34\text{ eV}$, scattering on the electron beam of VEPP – 4M produced the beam of backward-scattered photons. The photon energy varies from

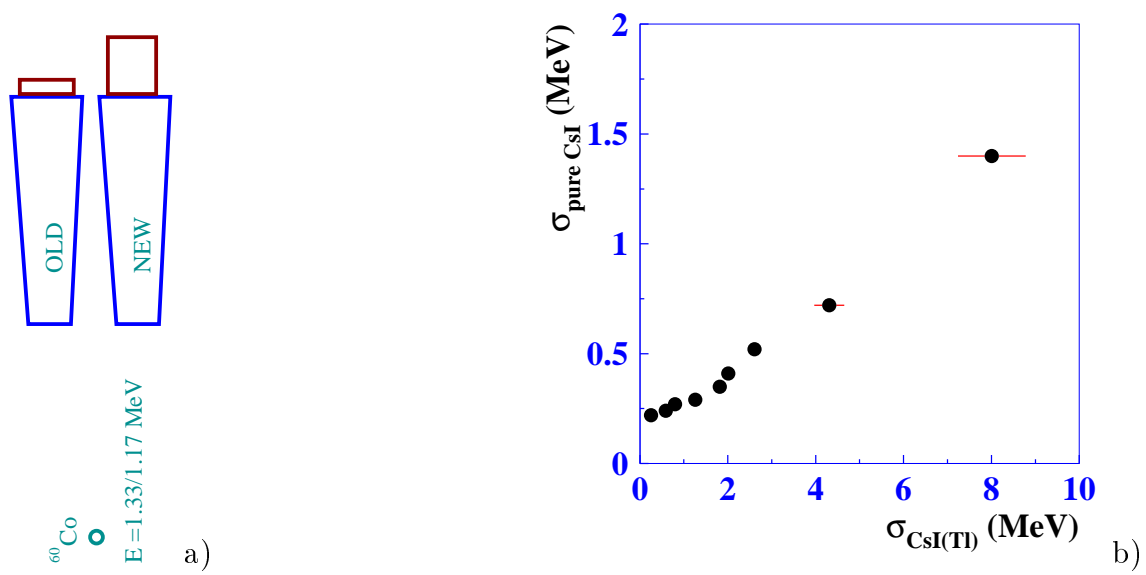


Figure 2.26. a) Pile-up measurement scheme; b) results of comparison of the counters based on pure CsI and CsI(Tl) Belle counter.

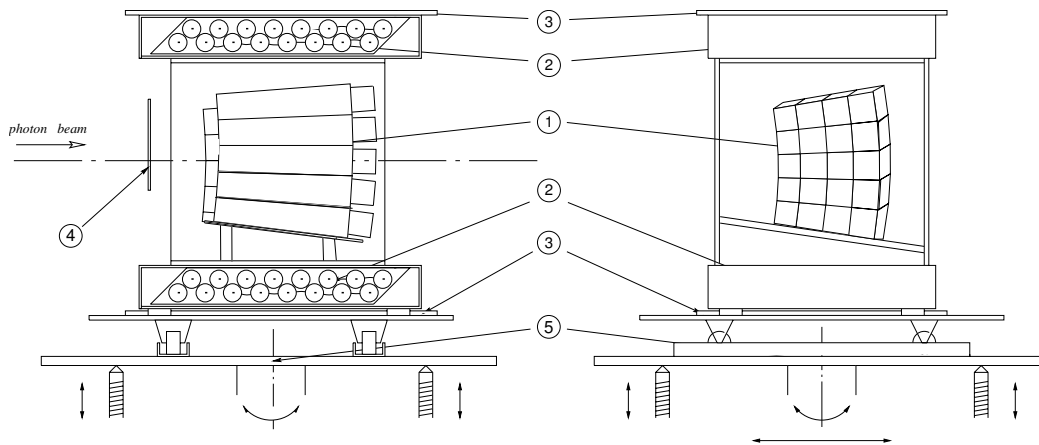


Figure 2.27. The scheme of the measurements with the calorimeter prototype on the VEPP – 4M photon beam. 1 – counters based on pure CsI crystals and photothetodes; 2 – streamer tubes system for cosmic rays coordinates measurements; 3 – cosmic trigger scintillation counters; 4 – veto scintillation counter of charged particles; 5 – movable steel base frame.

ω_0 to the maximal energy $\omega_{max} = \frac{4(E_{beam}/m_e)^2\omega_0}{(1 + 4E_{beam}\omega_0/m_e^2)}$ with a typical Compton spectrum shape, shown in Fig. 2.28a. This spectrum has a typical sharp right edge corresponding to the maximum photon energy. The electron energy $E_{beam} = 1.5 \sim 2.2 \text{ GeV}$ corresponds to the maximum photon energy $\omega_{max} = 70 \sim 160 \text{ MeV}$. The edge smearing (see Fig. 2.28b) is determined by the energy resolution. Fitting the measured spectrum to the convolution of the Compton spectrum with a logarithmic-normal function, we obtain the energy resolution.

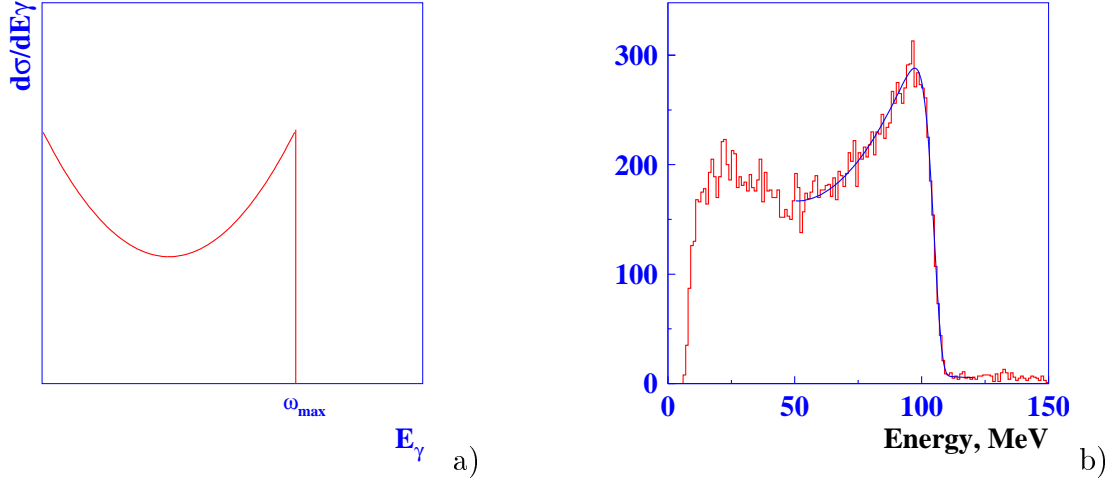


Figure 2.28. a) Backward scattered photon spectrum b) Spectrum of photon energy measured with prototype.

The measured resolution is shown in Fig. 2.29a. The obtained data are in a good agreement both with the Monte-Carlo simulation and the results obtained with the Belle calorimeter prototype [51]. The time resolution of the calorimeter depending on the energy deposition in the

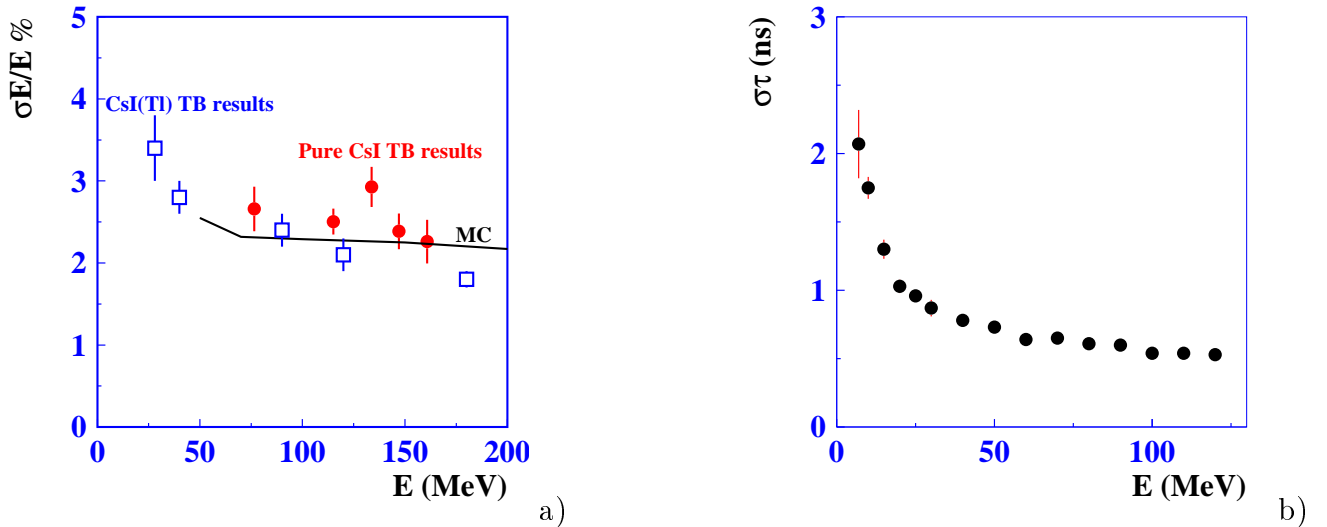


Figure 2.29. Energy a) and time b) resolution obtained with the pure CsI prototype.

counter is shown in Fig. 2.29b. For energy higher than 20 MeV the time resolution is better than 1 ns. Since the signal in magnetic field is expected 3.5 times lower, the corresponded time

resolution will be obtained at 3.5 times larger energies. The time information enables essential suppression of the beam background signals.

2.6.6 Summary

The calorimeter based on the pure CsI crystals is a proper solution for the experiments at $c\tau$ factory that provides high energy and position resolution for photons in a wide energy range with the expected background. The photopentodes as well as silicon avalanche photodiodes can be used as photosensors. The radiation resistance of the counters allows keeping stable calorimeter performance during the whole experiment.

Although the cost of the considered system is rather high, we do not see at present another option, cheaper and well developed, which could guarantee achievement of the necessary parameters. There is a possible compromise of using pure CsI crystals in the end caps, where the background is very high, while in the barrel part, where the background is lower, we could use cheaper CsI(Tl) crystals. In this case, the length of the barrel crystals could be increased to improve the energy resolution in the range 1-2 GeV. Of course, R&D works on other options are highly desirable.

2.7 Muon system

The muon system consists of nine layers of coordinate detectors in the barrel and eight layers at the endcap. The barrel part covers a solid angle of $64\% \times 4\pi$ ($50^\circ < \Theta < 130^\circ$), while the endcap of $30\% \times 4\pi$ ($20^\circ < \Theta < 50^\circ$ and $130^\circ < \Theta < 160^\circ$). The coordinate detectors are alternated with layers of a steel absorber, which also serves as the yoke of the magnet.

The main task of the muon system is to separate muons from a large number of hadrons produced in e^+e^- annihilation. Muons are identified by measuring their penetration depth (range) in the absorber. The ranges of muons and hadrons in matter are determined by two main processes: the ionization energy loss of a charged particle and nuclear interactions of hadrons with atoms of the absorber. Muons have larger kinetic energy as compared with pions and kaons at the same momentum, so they could lose more energy on ionization and their path is longer. Nuclear interactions of hadrons with the medium lead to additional absorption and further decrease of their range.

Due to the bending of the particle track in the magnetic field, the muon system detection threshold is at a particle momentum of 0.4–0.5 GeV/ c . In reality it is difficult to obtain reliable μ/π separation at the momenta below 0.8 GeV/ c — a pion range can be close to a muon due to fluctuations or a pion can decay into muon and neutrino with muon emitted in the direction of the initial pion. Above 0.8 GeV/ c , the muon detection efficiency reaches 95–98 % and the level of pion misidentification is $\sim 5\%$ which corresponds to a pion suppression factor of ~ 20 . To achieve the main goals of the $c\tau$ factory research program, pion suppression at a level of 100 or better is desirable. For this the muon system will work in combination with the FARICH identification system. The information from the FARICH can also be used for muon system calibration.

In modern experiments, coordinate detectors of different types are used in muon systems: counters with a localized discharge [66], streamer mode gas detectors [67], and scintillation counters [68]. The choice of the detection technology of coordinate chambers requires a study of their long-term stability and resistance to the backgrounds under the experimental conditions of the $c\tau$ factory. The total area of the coordinate detectors is more than 1000 m², so the cost of the detector production should be taken into account.

Currently, as a “working” option of the coordinate detectors for the muon system, it is proposed

to use coordinate detectors similar to the streamer tubes used in the KEDR detector [69]. Streamer tubes in a single block are arranged in two layers and are shifted relative to each other by half of the diameter. With this arrangement, a particle track always crosses one or more tubes at any incidence angle. Tubes of one electronic channel are connected sequentially in a row and alternate with the other channel tubes to reduce the probability of simultaneous triggering of several tubes in one channel by a single particle.

The basis of the block are two duraluminum flanges holding thin-wall stainless steel tubes. At the ends of the tubes, kapronit plugs with two holes are pressed. One hole in the center is for pin fixation and the second is for a gas inlet or outlet. In the center of the tube an anode wire is stretched with a force of 300 g and fixed in pins. The wire material is gold-plated molybdenum with a diameter of 100 μm .

The scheme of the readout electronics of one channel is shown in Fig. 2.30. A measurement of the longitudinal coordinate is based on the difference between the arrival times of signals on the opposite ends of the tube row. Two amplifiers with variable threshold discriminators are connected to both ends of the row. Load resistors prevent reflections at the ends of the row. The “start” and “stop” signals from both discriminators are transmitted to the expander. The “stop” signal is delayed to come later than the “start” regardless of the hit position along the row. The expander gives a paraphase signal with the duration equal to the interval between the “start” and the “stop” multiplied by a coefficient of expansion of about 40. Signals from the outputs of the expanders are transmitted via shielded twisted-pair cables to the inputs of the TDCs.

The duration of the output pulse from the expander depends on the particle hit location. Reconstruction of the hit longitudinal coordinate is done using a linear approximation taking into account the length of the wires connecting the tubes. The typical resolution of the longitudinal coordinate is about 4 cm. The transverse coordinate is given by the number of fired tube. A more accurate measurement of the transverse coordinate using the drift time of ionization is possible but not necessary because of the strong multiple scattering in the absorber.

For operation in the streamer mode, the gas mixture should contain a component with strong photon absorption in the UV spectrum. The working gas in the muon system is a nonexplosive mixture of 70%Ar : 23%CO₂ : 7%n-pentane.

2.8 Superconducting solenoid

2.8.1 Main requirements

The superconducting solenoid is intended to produce an axial magnetic field in the detector volume. The coil of the solenoid will be placed between the EM calorimeter and the muon system. This placement does not impose strong constraints on the thickness of the solenoid.

The main parameters of the solenoid are listed in Table 2.3.

2.8.2 Original approach

Analogous superconducting solenoids were produced in the last decade by Japanese and European companies. For their production, a technology based on superconducting cable with aluminum stabilizer was developed. The stabilizer made of 99.999% Al with the price of \$1000/kg dominates the cost of the solenoid. The main purpose of the stabilizer is quench protection. The stabilizer drastically minimizes the heat generation inside the solenoid, i.e. ρJ^2 , where J is the current density and ρ is the electrical resistivity of the stabilizer. This circumstance was considered from three following points of view:

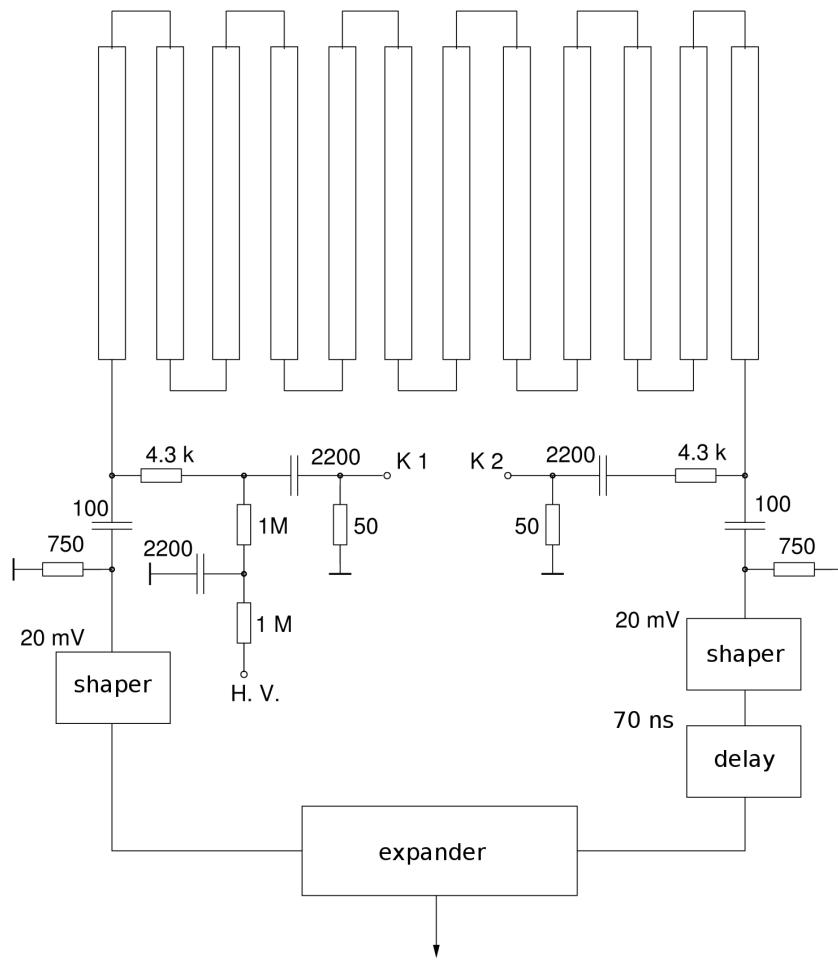


Figure 2.30. Readout electronics of the muon system

Table 2.3. Main parameters of the solenoid.

Length	4 m
Internal diameter	3.2 m
Magnetic field	1 T
Stored energy	12.9 MJ
Charging time	< 4 h

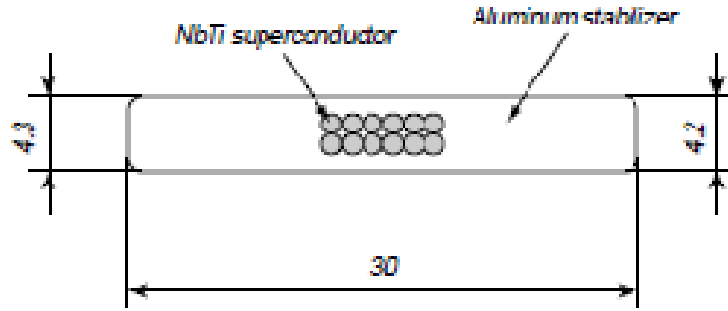


Figure 2.31. SC cable used in the ATLAS central solenoid.

1. the electrical and thermal properties of 99.999% Al and 99.99% Al differ by factors of 2 to 5, while the cost of 99.99% Al is less by factor of > 100 ;
2. the heat generation can be also minimized by increasing the amount of the stabilizer;
3. in the modern solenoids employed at LHC active quench protection is used.

The solenoid design for the $c\tau$ factory is based on the superconducting cable with the stabilizer of 99.99% Al. Active quench protection with heaters will be used for quench propagation. The proposed approach allows \$1–2 millions to be saved for the solenoid production.

Preliminary calculations show that the size of superconducting cable (SC) can be the same as for the ATLAS central solenoid, which is shown in Fig. 2.31. The cable for ATLAS was produced by Hitachi Co, Japan.

2.8.3 Cryogenics

The cryogenics of the detector should provide the operation of the detector solenoid and the final focus quadrupoles of the collider at a temperature of 4.5 K. The cryogenics will be based on a refrigerator with 100 W cooling performance at 4.5 K.

2.9 Trigger

The trigger of the $c\tau$ factory detector will be based on the concept of the “open-trigger”, which can select and save up to 100% of useful events. This concept implies that event selection is based on the following universal criteria: the presence and the topology of tracks in the coordinate system, the total energy deposition in the calorimeter, the topology of the energy deposition, the number

Table 2.4. Luminosity, physical cross section, rates of useful, Bhabha and cosmic events at different energy ranges.

	J/ψ	$\psi(2S)$	$\tau\bar{\tau}$	$\psi(3770)$	$\tau\bar{\tau}$	$\Lambda_c\bar{\Lambda}_c$
E_{cm} , MeV	3097	3686	3700	3770	4250	4650
L , 10^{34} $\text{cm}^{-2}\text{s}^{-1}$	7.7	9.2	9.2	9.4	10	10
σ , nb	~ 3400	~ 640	2.5	~ 6	3.5	0.5
f , kHz	260	60	2.3	5.6	3.5	0.5
Bhabha, kHz	~ 90	~ 80	~ 80	~ 80	~ 60	~ 50
Cosmics, kHz	~ 2					

of clusters in the calorimeter and the response of the muon system. The “open trigger” is not specially tuned for the selection of a particular predefined processes. This approach is conditioned by the very wide and diverse physics program of $c\tau$ factory and the task of finding “new physics”, which is impossible to predict in advance. A disadvantage of this approach is that basing on the trigger it is impossible to separate useful events from the events of nonresonant hadron production.

The useful event rates and rates of Bhabha events at different energies as well as rates from cosmic events are presented in Table 2.4. The cross section of the nonresonant hadron production at these energies is ~ 20 nb, which corresponds to a counting rate of 20 kHz at a luminosity of 10^{35} $\text{cm}^{-2}\text{c}^{-1}$. At present, it is difficult to estimate the trigger counting rate from the background events associated with the beam loss and beam interaction with the residual gas. The working conditions at the B factories at KEK and SLAC and the current development of the Super B factory in Italy indicate that this counting rate will be at a level of several tens of kHz.

As follows from the data in Table 2.4, the maximum readout rate of useful events will reach 300–400 kHz. The average size of a single event is estimated as 30 kB.

To achieve such a high event readout rate at the $c\tau$ factory, it is planned to use the methods and approaches developed at the BaBar detector and for the Super B project.

- All signals from the detector systems are continuously digitized in the electronics located directly on the detectors. The data are stored in digital pipelines for a few microseconds. The storage time is determined by the decision-making time of the L1 (L1) trigger.
- The electronics of the drift chamber, calorimeter and muon system give additional “fast” signals, which are transmitted directly to the L1 trigger.
- After receiving the signal from the L1 trigger, data from the onboard electronics are transmitted on the high-speed optical links (10 Gbps) into the readout processors (ROP), which are located outside the detector. The preprocessing is performed in the ROPs (actual signal amplitudes and times are computed) in order to reduce the amount of data. Additional filtering based on the topology and timing information is also performed at this stage.
- Data from the ROPs of each system come into the “event builder” computer farm, where they are synchronized and then processed by the high level trigger.
- The L1 trigger uses “fast” signals from the detector systems for a search of “useful” events (Fig. 2.32). It is based on a specialized pipelined processor with the programmed logic of the

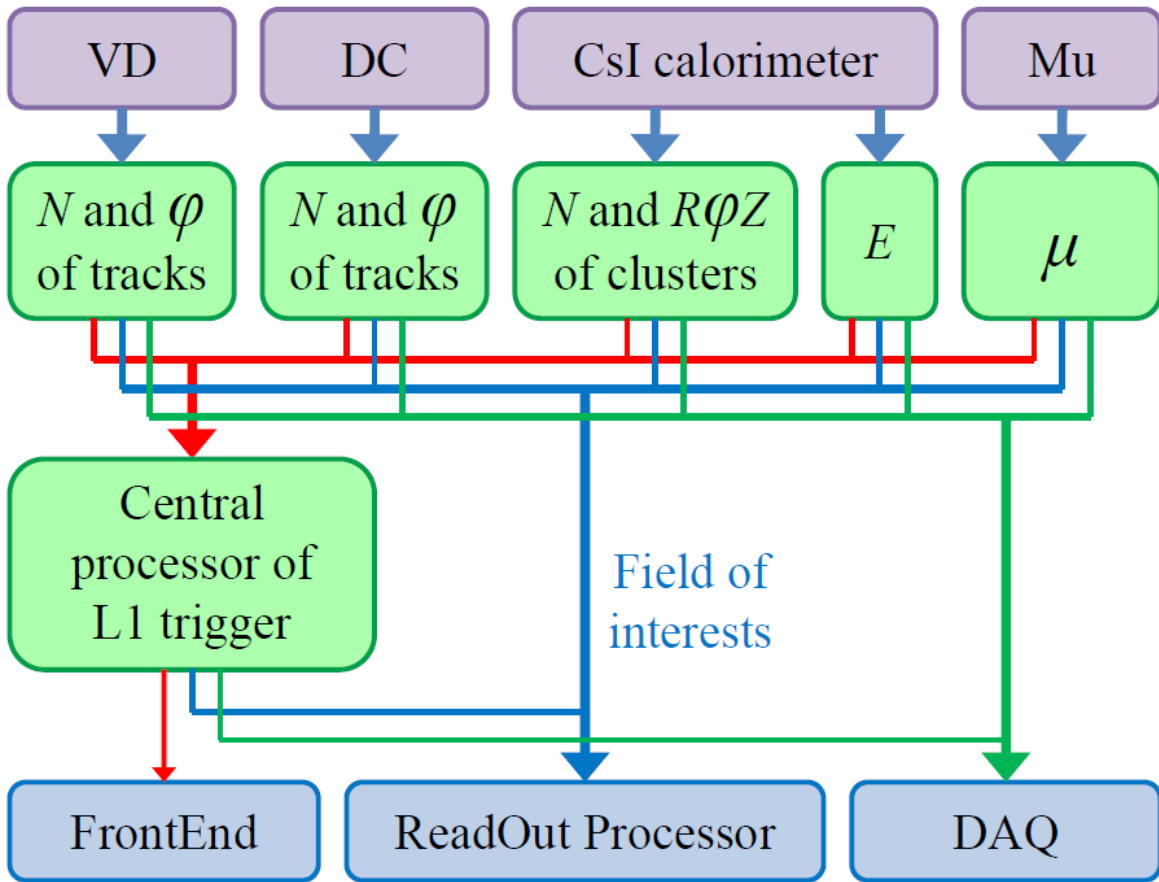


Figure 2.32. Block diagram of the Level 1 trigger.

event search. This logic uses the topology of tracks in the coordinate system, the total energy deposition, the topology of energy deposition and the number of clusters in the calorimeter, as well as data from the muon system.

- The L1 trigger decision pulse goes to the FrontEnd electronics. The fields of interests are transferred to the ROPs. And the intermediate information about the trigger is transmitted to the Data Acquisition system.
- The L1 trigger will occupy two racks that will be located near the detector together with ROP racks.
- The maximum frequency of the decision making is 500 kHz, the effective “dead time” of the L1 trigger should not exceed 100 ns. The decision making time of the L1 trigger is a few microseconds.
- The high level trigger is software based. The fast preliminary reconstruction of the events to get information about the coordinates, momentum and energy of all secondary particles is performed. At this stage, the effective rejection of the background events from the beam interactions and cosmics is done. To reduce the amount of the recorded information, prescaling of the Bhabha scattering events could be implemented. The high level trigger will be organized on the basis of a specialized computer farm, consisting of several hundred processors.

2.10 Electronics

Electronics together with the computers and telecommunication equipment of the detector are one of the key elements of the $c\tau$ factory detector.

The collider parameters important for the electronics are given below.

- The RF frequency is about 508 MHz.
- The period of bunch circulation is $2.557 \mu s$.
- The quantity of separatrices is 1300.
- Each third separatrix is filled, so the time gap between bunches is around 6 ns.
- The mode with filling each fourth separatrix is under discussion.
- The maximum quantity of bunches in a train is 390.
- A gap of 5–10% (130 separatrices) in a bunch train is necessary for suppression of the ion instability.

For precise time measurement of several detector subsystems it will be necessary to know the bunch distribution in a train. Therefore, the binary map of the bunches will be used (Fig. 2.33). It will be especially important at the beginning of work, while not all bunches are filled.

The synchronizing “phase” pulse for the bunch circulation will be also necessary.

The structure of the subsystems of the new detector should be taken into account during the development of electronics for the $c\tau$ factory detector. The electronics will have a huge number of channels. It should be fast and reliable and have a possibility of remote control and self-test capability.

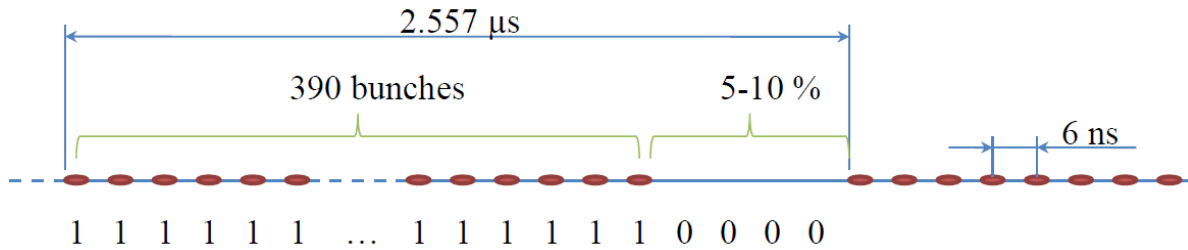


Figure 2.33. The bunch distribution and the corresponding binary map.

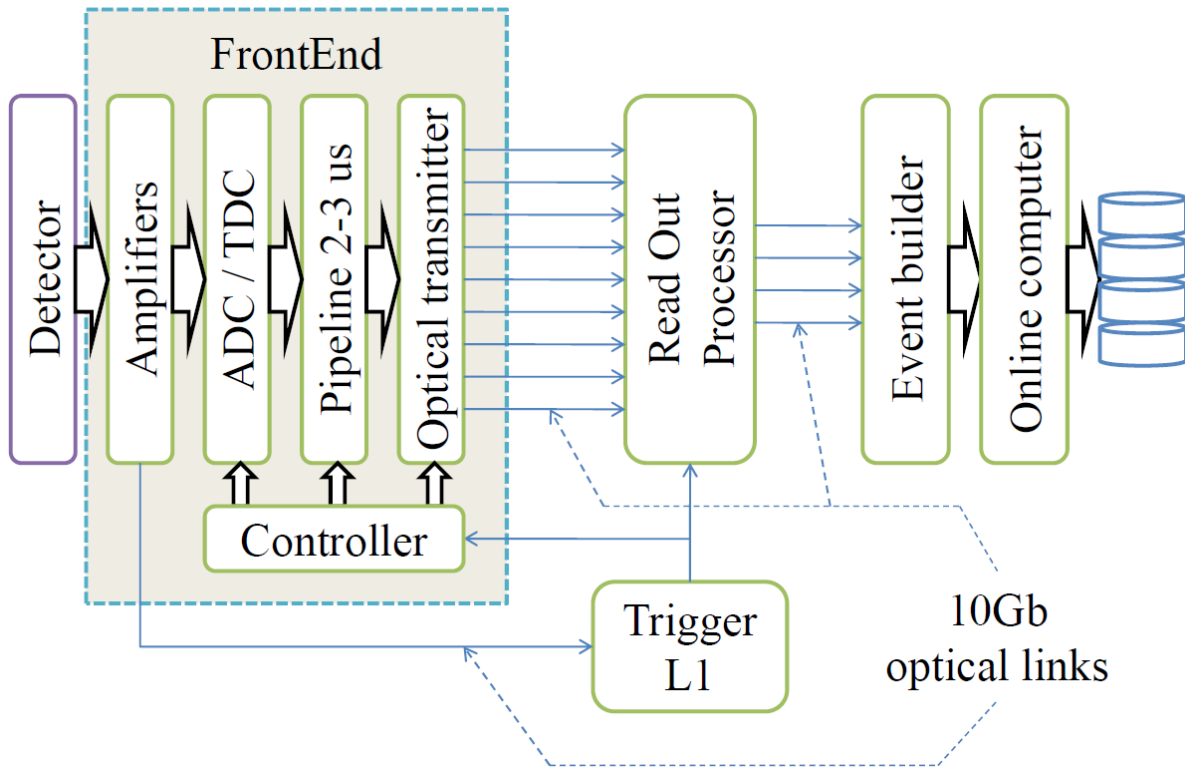


Figure 2.34. Block diagram of electronics.

During the designing of the analog and digital electronics for the detector subsystems, it is necessary to optimize the electronics for particular systems, as well as minimizing the cost of electronics development.

The overview block diagram of the readout electronics is shown in Figure 2.34. The FrontEnd (FE) electronics contain amplifiers, ADC and TDC, an obligatory pipeline for the working time of the L1 trigger, controller, which manages the operation and optical transmitters. 10 Gbps optical links connect the FE electronics and the readout processors (ROP) located near the detector. The ROPs get raw data and perform calculations of the amplitude and time of pulses. The ROPs can also perform additional selection of information based on the L1 trigger data. The results are sent to EventBuilders and to on-line computers located in the data storage hall.

The L1 trigger is located near the detector. It also gets fast information from the FE electronics via 10 Gbps optical links.

Table 2.5. Limitations and demands on electronics of subsystems.

Detector	Channel quantity	Channel size	Power consumption	Trigger participation	Information
VD-GEM	56 K	$2 \times 2 \text{ mm}^2$	1 kW	Possible	A, T, P
VD-Pixel	10 M	$150 \times 150 \mu\text{m}^2$			
DC	7.1 K	$12 \times 20 \text{ mm}^2$	2 kW	Yes	A, T, P
FARICH	1 M	$4.5 \times 4.5 \times 50 \text{ mm}^3$	100 kW (21 m^2)	No	T, P
Calorimeter	7.5 K	$(40 - 70)^2 \text{ mm}^2$	2 kW	Yes	A, T, P
Mu	4-44 K	diameter 20 mm	1-9 kW	Yes	T, P

2.10.1 FrontEnd electronics

Table 2.5 presents the quantity of electronics channels for different subsystems of the detector, the geometrical size of the channels, an estimated power consumption, participation of subsystems in the trigger and the type of required information (A - amplitude, T - time, P- position).

All analog-to-digit conversions will be performed inside the detector in the FE electronics. The events information selected by the L1 trigger will be packaged and sent via 10 Gbps optical lines. It is necessary to use the ASICs to reach a required channel density and power consumption.

The FrontEnd electronics will be cooled as follows. Printed circuit boards (PCB) will be installed into aluminium boxes, which will provide EMR shielding and heat removal. All microchips on the PCBs will have thermal contact with the boxes through heat conductive rubber. If the usage of a closed box is not suitable, an aluminium plate can be applied. The heat from the boxes or plates will be transferred out by the water pipe system. The excess heat will be released in a chiller. The pressure in the water pipes should be less than the atmospheric one to prevent possible leakages. Then in case of seal failures, the water will not flow out but the air will be sucked in.

It will be possible to roll away the detector end caps (Fig. 2.36). So, one will have access to the internal systems of the detector. It will simplify the electronics maintenance. The FrontEnd-electronics will be modular it will allow to change broken units quickly.

Table 2.6 shows the maximal channel load, the time characteristics of the pulses, the required rates of digitization, number of bits of ADC and TDC and the necessary precision of time measurements.

Depending on the implementation, the vertex detector will have 56K to 10M channels. In the first case, it is the GEM detector and in the second case it is the semiconductor pixel detector. In the case of GEM, the load per channel is expected to be at a level of 33 kHz. Digitization of signals with an edge of about 25 ns requires a 10-12 bit ADC with sampling rates of about 80 MHz. The time position of a signal is to be defined with an accuracy of 1 ns.

The drift chamber will contain 7K sensitive wires. The loading of one channel is expected to be at a level of 50 kHz. A 10-bit ADC with a sampling rate of about 50 MHz will suit for ordinary DC operation with the edge of signals at a level of several hundred ns. In case of operation in the cluster mode, an ADC with a sampling rate about 1 GHz is required.

The FARICH will have a huge number of channels. A loading of each channels is expected to be at a level of 1 MHz. The time position of short signals is to be defined with an accuracy of

Table 2.6. Parameters of electronics of subsystems.

Detector	Channel load	Duration of signals	Rate of digitization	Bit quantity of ADC (TDC)	Time meas. precision
VD	33 kHz	Rising edge 25 ns	from 20 to 80 MHz	10–12 bit ADC	1 ns
DC	50 kHz	Rising edge	50 MHz (ordinary mode)	10 bit ADC	1 ns
		100–200 ns, Follow edge 300 ns	500–1000 MHz (cluster mode)	10 bit ADC	1 ns
FARICH	1 MHz	5–10 ns	—	6 bits (for 8 ns) TDC	200 ps
Calorimeter	15 kHz	30 ns for pure CsI	40–50 MHz	18 bit ADC	1 ns
Mu	100 kHz	30–200 ns	—	11–12 bit TDC	60 ps

Table 2.7. Number of electronics channels, data and trigger links.

Detector	Number of channels	Number of data links	Number of trigger links
VD–GEM	56 K	56	56
VD–Pixel	10 M	n/a	n/a
DC	7.1 K	48	48
FARICH	1 M	100	0
Calorimeter	7.5 K	32	32
Mu	4 – 44 K	32	32

several hundred ps.

The calorimeter will have 7.5 K channels with loading of each at a level of 15 kHz. Exact measurement of amplitude in a large dynamic range requires an ADC with a large width of about 18 bits.

The muon system made of streamer tubes will have 4K to 44K channels, depending on the scheme of their connection. The main aim of the electronics here it to get a time resolution at a level of 60 ps.

Table 2.7 was composed basing on an evaluation of data streams from FrontEnd electronics and taking into account the design features of the detector subsystems. The quantity of optical links for data transfer and trigger information is presented. Totally 268 data links and 168 trigger links will be necessary.

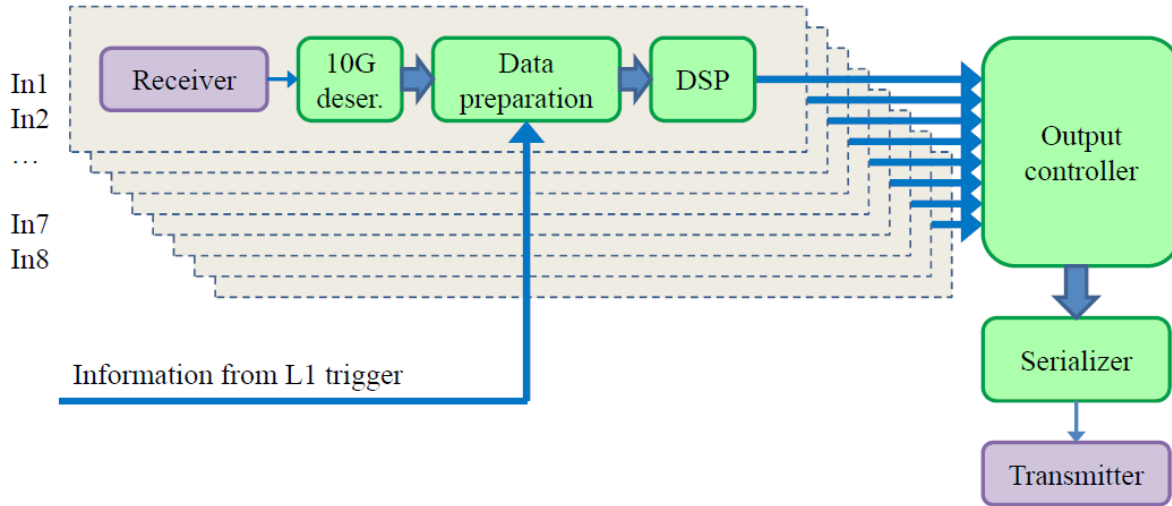


Figure 2.35. Block diagram of the ReadOut processor.

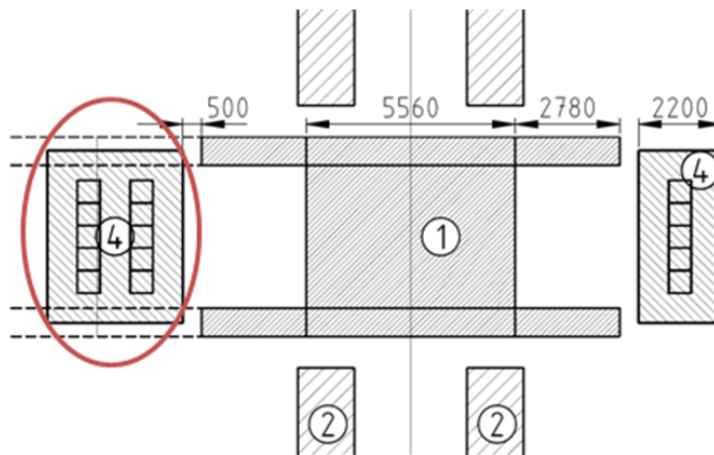


Figure 2.36. Location of racks with ROPs near the detector.

2.10.2 Readout processor

The Readout processor (ROP) gets data via several optical links (Fig. 2.35). The ROP can be equipped with 2 to 8 optical inputs depending on the complexity of executed algorithms. Therefore, up to 134 ROPs will be necessary. This unit calculates the amplitude and time of pulses from the raw data coming from the FE electronics. It uses L1 trigger information to process the so called “field of interests”, the places in the detector where channels have been triggered. This approach reduces the processing time and amount of the output data. Results are sent to EventBuilders for the next stage of processing.

134 ROPs will occupy 14 VME crates, which will be located in 5 racks. The preliminary power consumption of one crate is about 900 W, so one rack will consume 1.8–2.7 kW. The racks with ROPs will be located near the detector (Fig. 2.36).

2.10.3 Drift chamber electronics

As an example, we consider in more detail the FE electronics of the drift chamber (Fig. 2.37). The DC FE electronics will be composed of 48 modules of 3 types. Each module will have 128 to 192 channels, 2 to 4 FE boards (FEB), and one readout board (ROB). Each FE board will contain 48 to 64 channels of the amplifiers and ADCs. The readout board will have a common pipeline and controller, which will send information to a ROP upon a signal arrival from the L1 trigger. A calibration signal will be sent to each module. This signal will be used for checking the electronic channels.

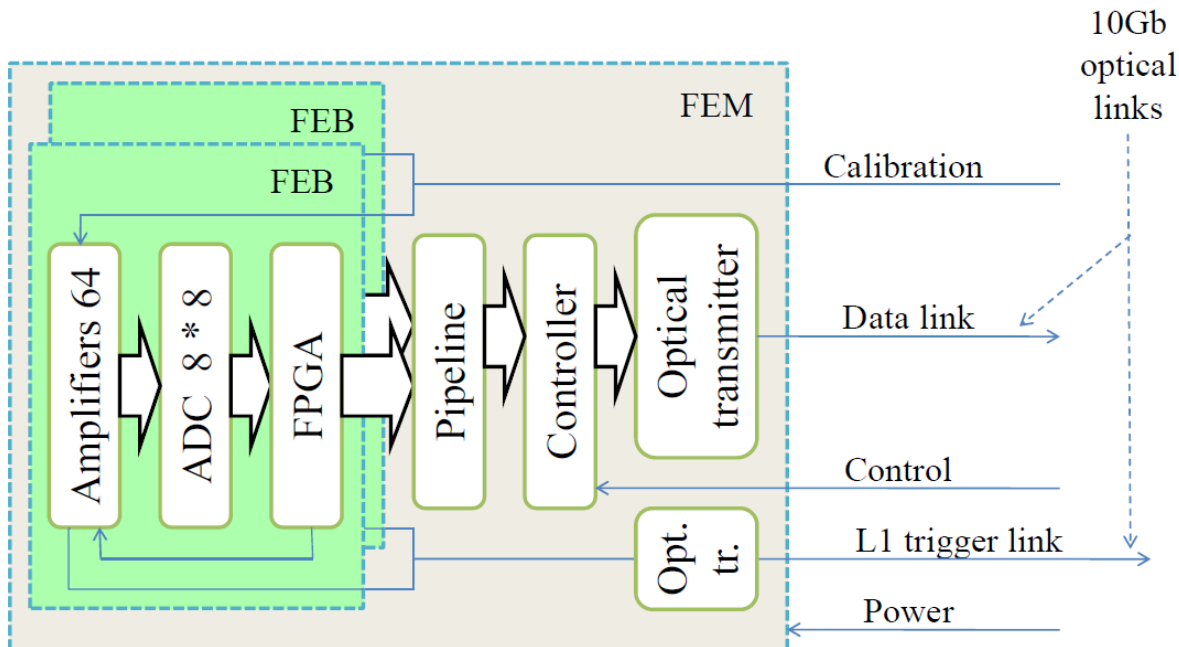


Figure 2.37. Block diagram of the drift chamber FE module.

2.11 Networking and computing systems

2.11.1 Introduction

The networking and computing infrastructure will play a substantial role in the experiment at the $c\tau$ factory detector. Below we give a thorough overview of designing, building and operating the computing infrastructure for this experiment.

The requirements to the computing infrastructure of $c\tau$ factory are discussed in section 2.11.2. The overview of the whole computing system, including the trigger and DAQ, offline data processing and data storage, is discussed in section 2.11.3. A more detailed description of the data processing and data storage systems is given in section 2.11.4. The estimation of the hardware and financial resources required for the proposed computing and networking solutions and the implementation and deployment plans are discussed in section 2.11.5.

Section 2.11.3 contains a brief introduction to the prospected organization of the trigger and DAQ, offline data processing and data storage systems of the detector. It also gives an insight into the architecture and hardware requirements for the systems involved.

2.11.2 Requirements to the computing infrastructure

The data structure and the expected data size are determined by the $c\tau$ factory experimental program, which includes both studies of the rare decays and studies with the secondary particles created in the main decay modes. The physics program of the experiments requires using a relatively soft hardware trigger, which will lead to a large number of stored events because of the expected high luminosity of the collider.

The expected data structure is typical for a high energy physics experiment. The main levels of the data are as follows: the raw data, which contain information directly received from the frontend electronics; the processed data, which contain high-level information about reconstructed tracks, clusters, particles, etc.; the simulated data, which are similar to the raw data, but generated using the Monte-Carlo simulation. Following the experience of other experiments, several intermediate levels of processed data may be defined, differing in details of the stored information.

The raw event size is estimated as 30–50 kB, which is typical for the detectors operating at e^+e^- colliders at similar energies (B -factories, BESIII, KEDR). The computational complexity of the reconstruction of one event is estimated as 0.15–0.30 Gflops-sec/event, which is significantly less than the values typical of LHC detectors. The computational complexity of simulation of one event is estimated as 2–5 Gflops-sec/event. To ensure data processing, simulation and physical analysis, the total processing power of the data analysis system should be about 600 Tflops (approximately $6 \cdot 10^6$ HEP-SPEC06), with most of these resources required for Monte-Carlo simulation.

Assuming the total number of events of $2 \cdot 10^{12}$, the total amount of raw data, including the backup copy, for the entire duration of the experiment is estimated as 150 PB. The total volume of one copy of the least detailed processed data from the detector, directly used in physical analysis, for the entire duration of the experiment is estimated as 10 Pbyte. Taking into account the opportunity to work with several versions of the processed and simulated data, the total amount of information storage is estimated as 240 PB. Due to the relative ease of the generation of highly-detailed processed data from the raw data, there is no need to organize long-term storage of the former. If the total number of events increases (for example, if more data are collected at the J/ψ energy), the total storage volume should be increased proportionally. The bulk of the increase in this case will accrue to a relatively cheap tape storage.

The amount of data expected on $c\tau$ factory is smaller, but comparable with the data volume of one LHC experiment, whereas the required computational resources are an order of magnitude smaller. Therefore, it would not be reasonable to organize a geographically distributed data processing and data storage system similar to the system used in the LHC experiments. However, it is quite reasonable to create an integrated system in which the storage system is centralized (performing the role of T0 in the WLCG model) and some of the computing resources are distributed. In this case, the remote resources will be used mainly for simulation and physics analysis, and the resources available within a centralized system for data reconstruction. Accordingly, the raw events constituting the bulk of the data will be stored in the central system, and several copies of the processed data, including simulation, will be stored both in the central system and at remote centers.

2.11.3 Brief Overview of TDAQ and Offline Data Processing Systems

The following functional groups of components form the computing environment of the $c\tau$ factory experiment:

1. Trigger and DAQ systems (TDAQ):

- (a) the two-level hardware and software trigger system with a maximum trigger rate of 0.5 MHz for an average event size of approximately 30-50 kB, thus capable of generating a stream of output data with a rate of up to 120-200 Gbps,
 - (b) the event building system,
 - (c) a storage buffer used for exporting data to the offline data processing systems.
2. Detector monitoring and control systems:
 - (a) the detector information system,
 - (b) the detector slow control system,
 - (c) the detector safety and access control systems,
 - (d) engineering infrastructure and environment conditions monitoring systems,
 - (e) dedicated control rooms for the continuous operation of the detector, its TDAQ systems and their computing infrastructure.
 3. The detector offline data processing farm and its multilevel heterogeneous data storage system.

The data flow diagram between these functional groups is shown in Fig. 2.38.

The detailed diagram of the data flow originating from the detector and going through its TDAQ, offline data processing and storage system is shown in Fig. 2.39, which also displays the proposed capacities of the storage systems involved and the throughput values of network links interconnecting them. These values were derived by minimizing the price/performance ratio for the whole detector computing system with respect to the financial estimations discussed in Section 2.11.5.1.

It is essential that the proposed configuration of the TDAQ and offline farm makes it possible to capture the full flux of data generated by the first level trigger and store it for the long term analysis if needed. Section 2.11.4.1 presents the architecture of the computing systems discussed here in more detail.

2.11.4 Architecture of the Data Processing and Storage Systems

2.11.4.1 Main Components

The generic layout of the key components of the TDAQ and the data processing and storage systems of the detector experiment listed above is shown in Fig. 2.40. Below is given a short description of the elements of the networking and computing infrastructure that play an important role in data taking, storing and processing.

1. **[FrontEnd1,2]** Modules of the front-end electronics installed within the volume of the detector located 17 m below the ground level in the dedicated detector building.
2. **[ReadOut1,2]** The electronics equipment installed in the dedicated racks in the vicinity of the detector and mechanically attached to it:
 - (a) power supplies of the front-end electronics,
 - (b) equipment for readout from the detector subsystems,
 - (c) Low Level Trigger (LLT) of the detector,

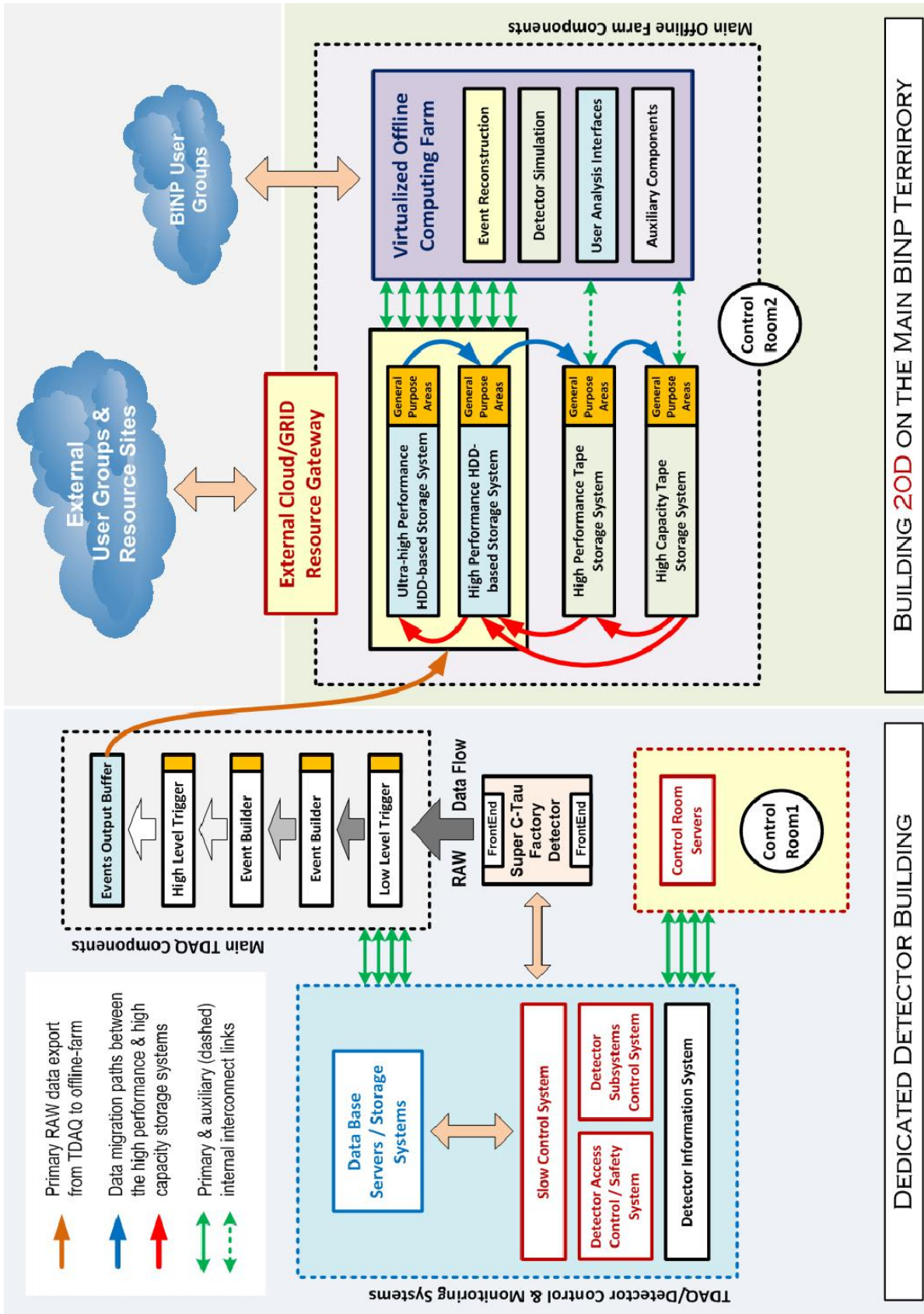


Figure 2.38. Generic data flow diagram for the TDAQ and offline data processing systems of the detector.

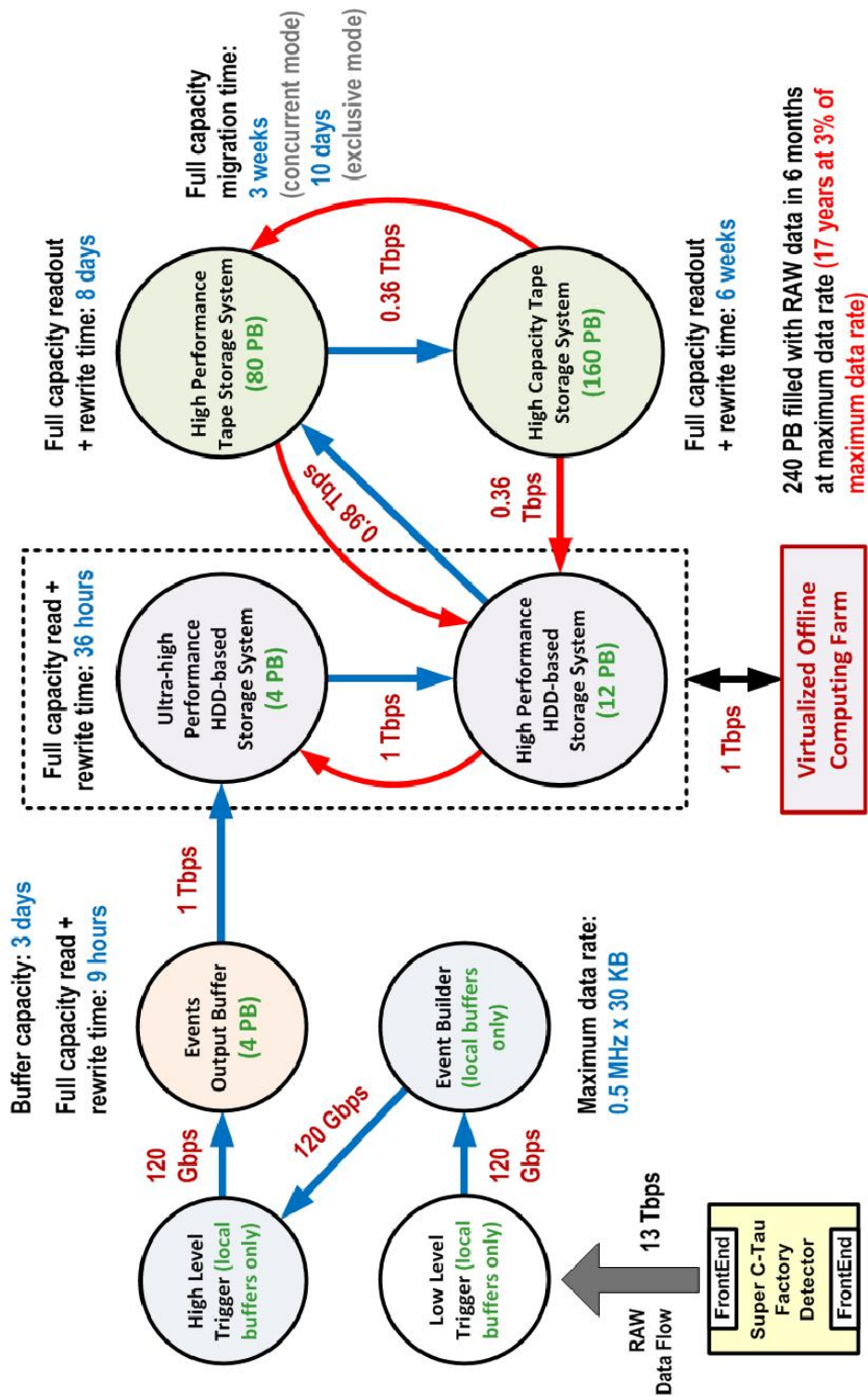


Figure 2.39. Detailed diagram of the data flow originating from the detector and going through its TDAQ, offline data processing and storage systems. Capacities of the storage systems involved and the expected data rates between them in a simultaneous read/write mode are displayed as well.

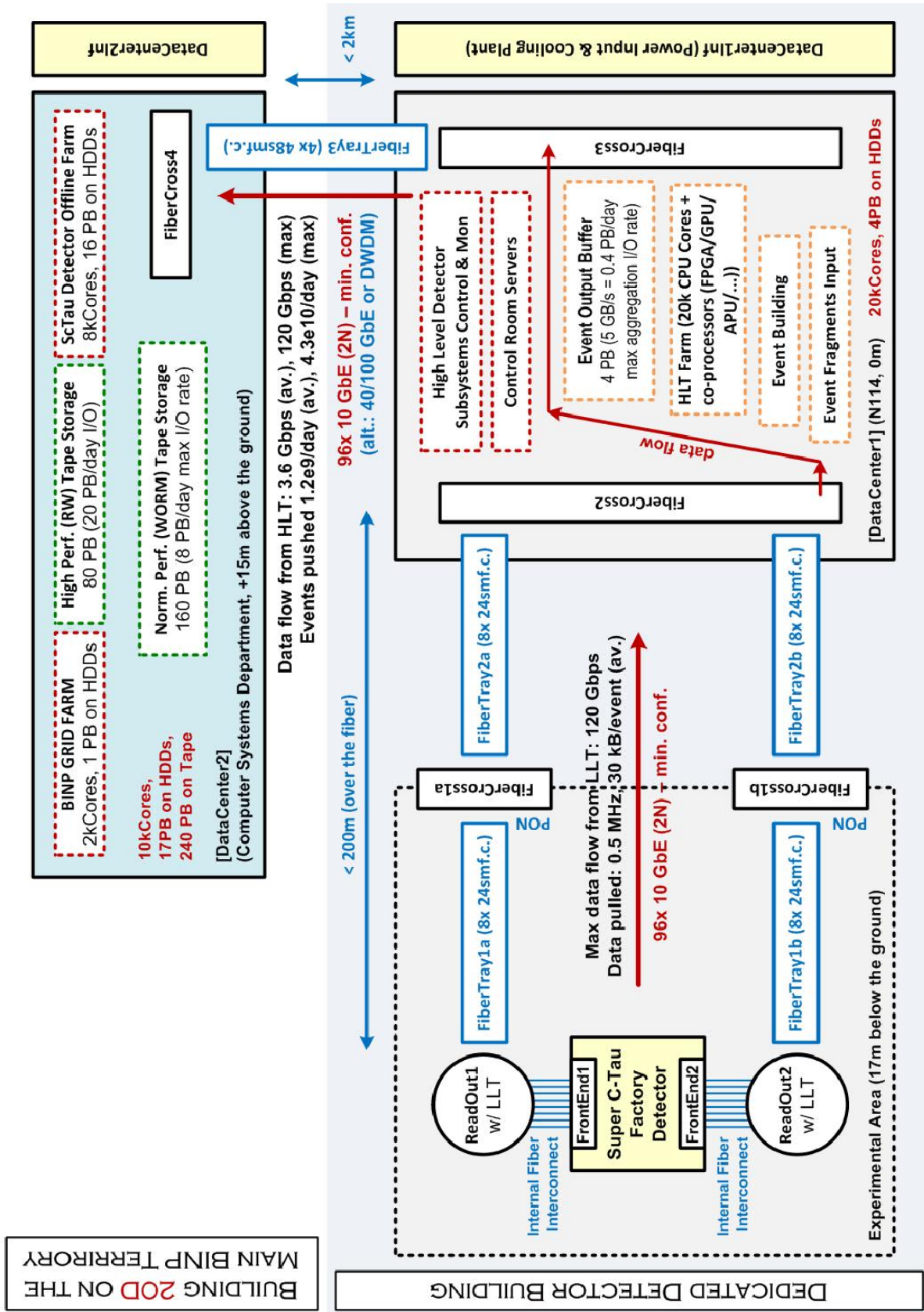


Figure 2.40. Generic layout of the key components of the TDAQ, data processing and storage systems of the experiment, located both in the dedicated detector building and the existing computing facility on the main BINP territory.

- (d) aggregation systems for experimental event fragments and output buffers for transferring the data aggregated to the Event Builder installed in the **[DataCenter1]** facility for further processing.
3. **[FiberTray1(a,b)]** Optical-fibers communication line connecting passive optical crossing **[FiberCross1(a,b)]**, placed on the ground level near the detector cavern with the **[ReadOut1,2]** modules, consisting of three parts:
 - (a) the fixed vertical section going down to the detector cavern in dedicated cable trays (providing mechanical protection and tension control for fibers) attached to one of the walls of the cavern;
 - (b) the horizontal movable and retractable section, which is capable of automatically adjusting itself to the position of the detector in the experimental cavern, supporting the fibers on their path from the wall of the detector cavern to **[ReadOut1,2]** modules;
 - (c) the fixed section provided with radiation resistant fibers (discussed below in Section 2.11.4.2)), which goes in the multiple paths from **[ReadOut1,2]** to **[FrontEnd1,2]** modules installed within the detector volume.

The optical line consists of sixteen 24-core multichamber optical fiber cables (192 pairs of SMF 9/125 optical fibers in total) subdivided into two equal sets of cables running over the physically independent paths within the detector cavern (at least 10 m separation along the path is required).

4. **[FiberTray2(a,b)]** Optical-fibers communication line connecting the passive optical crossings of **[FiberCross1(a,b)]** and **[FiberCross2]**, respectively (the total length is approximately 200 m over the fiber).

The optical crossing consists of 8 optical patch panels supporting 24 pairs of fibers each distributed among four racks within the **[DataCenter1]** facility.

5. **[DataCenter1]** Computing facility located in Area 114 of the dedicated detector building and hosting the following components:
 - (a) passive optical crossing **[FiberCross2]**,
 - (b) Event Fragment Input (EFI) and Event Builder (EB) subsystems,
 - (c) High Level Trigger (HLT) of the detector experiment,
 - (d) buffer storage systems used for exporting data between **[DataCenter1,2]** facilities,
 - (e) passive optical crossing **[FiberCross3]** of the **[FiberTray3]** optical communication line linking the **[DataCenter1,2]** facilities,
 - (f) servers supporting the detector control systems,
 - (g) servers supporting the environmental monitoring and detector safety systems,
 - (h) servers supporting the main control room **[ControlRoom1]**,
 - (i) terminal servers providing external access to the **[DataCenter1]** facility.

Location of the **[DataCenter1]** facility and its engineering infrastructure within the dedicated detector building is shown in Fig. 2.41. The detailed equipment installation plan for the **[DataCenter1]** facility is given in Fig. 2.42. A list of basic specifications for the **[DataCenter1]** facility is given in Table 2.8.

6. **[DataCenter1Inf]** Engineering infrastructure of the **[DataCenter1]** computing facility deployed in Areas 113, 113a, 115, 115a, and 116 of the dedicated detector building and its vicinity:
 - (a) inlets of 10 kV power cables,
 - (b) dedicated transformed plant,
 - (c) group of chiller modules serving the external cooling circuit of the **[DataCenter1]** facility,
 - (d) external cargo bays for Areas 113 and 115 of the detector building.
7. **[ControlRoom1]** Main detector control room constructed in Area 112 of the detector building, which holds control over
 - (a) the detector subsystems and their engineering infrastructure,
 - (b) the entire **[DataCenter1]** computing facility including its safety and access control systems.
8. **[FiberTray3]** Optical-fibers communication line with a length not exceeding 2 km over the fiber linking the **[DataCenter1,2]** computing facilities. The optical line consists of four 48-core multichamber shielded optical fiber cables (192 pairs of SMF 9/125 optical fibers in total).
9. **[DataCenter2]** Computing facility built within the existing BINP centralized IT facility, hosting the following components:
 - (a) passive optical crossing **[FiberCross4]** of the **[FiberTray3]** optical communication line linking the **[DataCenter1,2]** facilities,
 - (b) BINP general purpose internal networking core,
 - (c) offline data processing farm of the experiment,
 - (d) long term robotic tape storage system (several groups of tape robots),
 - (e) central database servers of the experiment,
 - (f) central backup system serving both **[DataCenter1,2]** facilities,
 - (g) terminal servers providing external access to the **[DataCenter1]** facility.

The prospected layout of the **[DataCenter2]** facility, assuming the major upgrade of its engineering infrastructure and deployment of all the equipment related to the detector experiment, is shown in Fig. 2.43. The list of basic specifications for the **[DataCenter2]** facility is given in Table 2.8.

10. **[DataCenter2Inf]** The engineering infrastructure of the **[DataCenter2]** computing facility deployed in the vicinity of its main IT area.
11. **[ControlRoom2]** The dedicated control room of the **[DataCenter2]** computing facility holding control of the IT equipment deployed within the **[DataCenter2]** facility and its engineering infrastructure, including safety and access control systems.

Possible extensions of the basic organizational scheme of the network and computing infrastructure of the experiment summarized here are discussed in Section 2.11.4.3.

2.11.4.2 Fiber-optics Communication Lines Deployed in the Vicinity of the Detector

As it was mentioned earlier in Section 2.11.4.1, the fiber-optics communication lines deployed in the vicinity of the detector, especially some subsections of **[FiberTray1]**, must be provided with means of radiation protection in order to keep the lifetime of fibers at a reasonable level and minimize the rate of permanent fiber failures during the detector lifetime.

The radiation protection of the fiber-optics communication lines is proposed to be implemented in one of the following ways:

1. full detector simulation to identify spots with high radiation loads within the detector volume, which are to be avoided while tracing the paths of optical cables,
2. shielding the bunches of optical cables by means of custom design cable trays (for the cables deployed outside the detector volume),
3. use of radiation resistant optical fibers shielded with special covers such as described in [85]–[89] in places where two previous solutions cannot be applied.

The optimal solution for the radiation resistant fiber-optics lines deployed within the detector is expected to be found while building and evaluating the prototypes of the **[FiberTray1]** communication line that are proposed in Section 2.11.5.2.

2.11.4.3 External Connectivity of **[DataCenter1,2]** Facilities and Discussion of the Possible Involvement of the Remote Computing Centers

All the network equipment providing the external connectivity for BINP and the detector in particular will be hosted at the **[DataCenter2]** computing facility, which will be an external network gateway for the entire computing infrastructure of the experiment.

Even at the early stages of the commissioning of the experiment and its networking and computing infrastructure, there will be connectivity to Supercomputer Network of Novosibirsk Scientific Center (NSC/SCN) [90] via the existing dedicated 10 Gbps optical network. In the longer term, the high-speed access via dedicated link will be provided to the resources of geographically remote supercomputer centers, as well as resources of international scientific networks, in particular, Geant3 (GN3) [91], international GRID-systems, in particular WLCG [92] through the high-speed virtual network LHCONE [93], and individual commercial cloud platforms, for example, Amazon EC2 [94].

The remote data centers can be integrated into the $c\tau$ factory computing infrastructure in the form of either a specialized distributed computing system or a virtual organization in one of the already existing distributed systems. In addition, it will be possible to use the resources of the commercial cloud platforms for short periods of peak loads. The main tasks for the external data centers are the Monte-Carlo simulation and physical analysis of the processed data. These tasks require significant computational resources, but a relatively small amount of data transferred. A dedicated external connectivity of the order of 10–40 Gbit/s will be enough to ensure the operation of the external centers.

If the capacity of the external network links allows, the data storage system can be extended to store a copy of raw data on the geographically remote sites, thus reducing the risks of data loss due to a catastrophic event on one of the site.

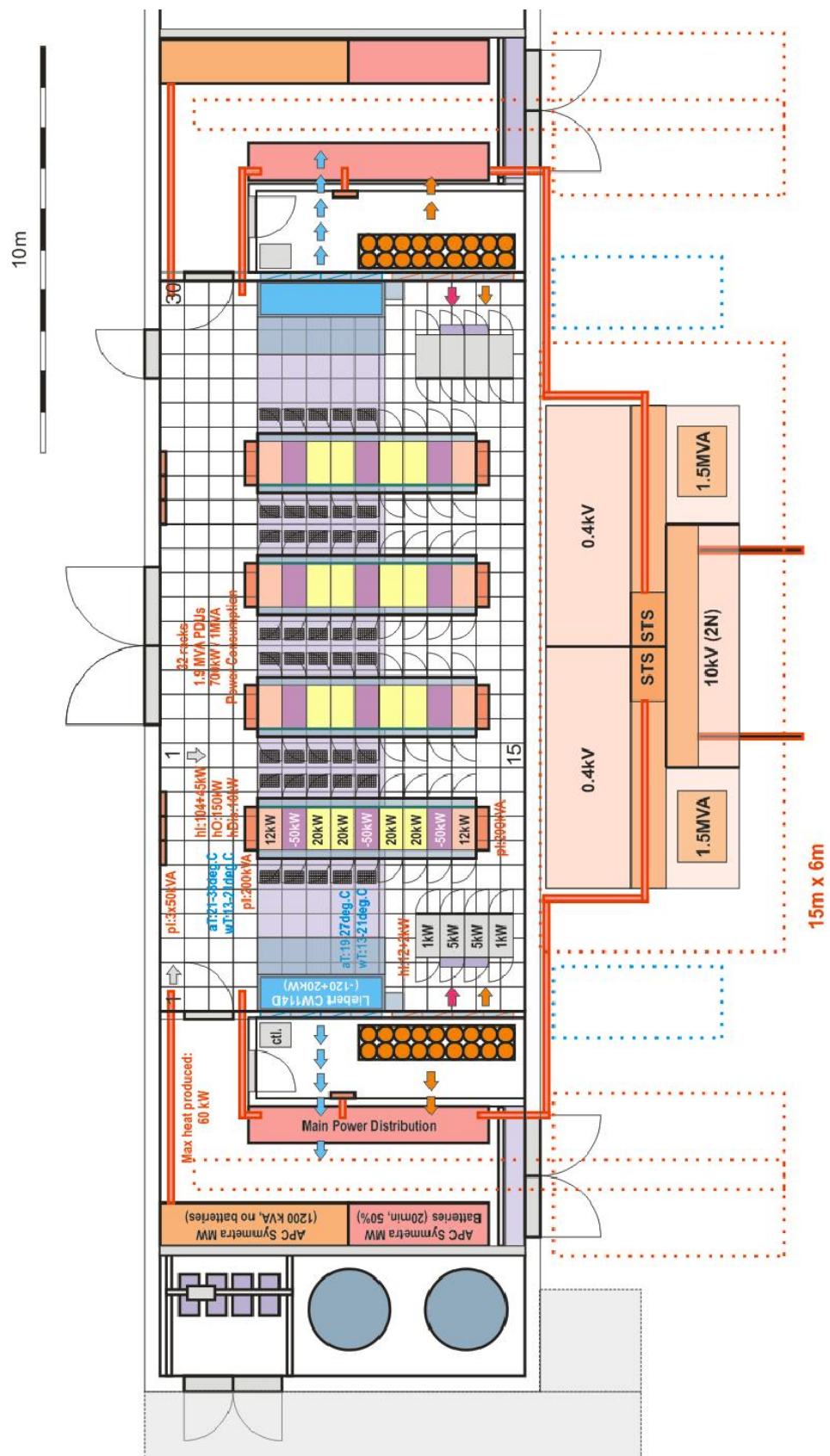


Figure 2.42. Closer look on the possible hardware installation layout of the [DataCenter1] facility (cooling and electrical power capacities indicated).

BINP IT FACILITY MAP

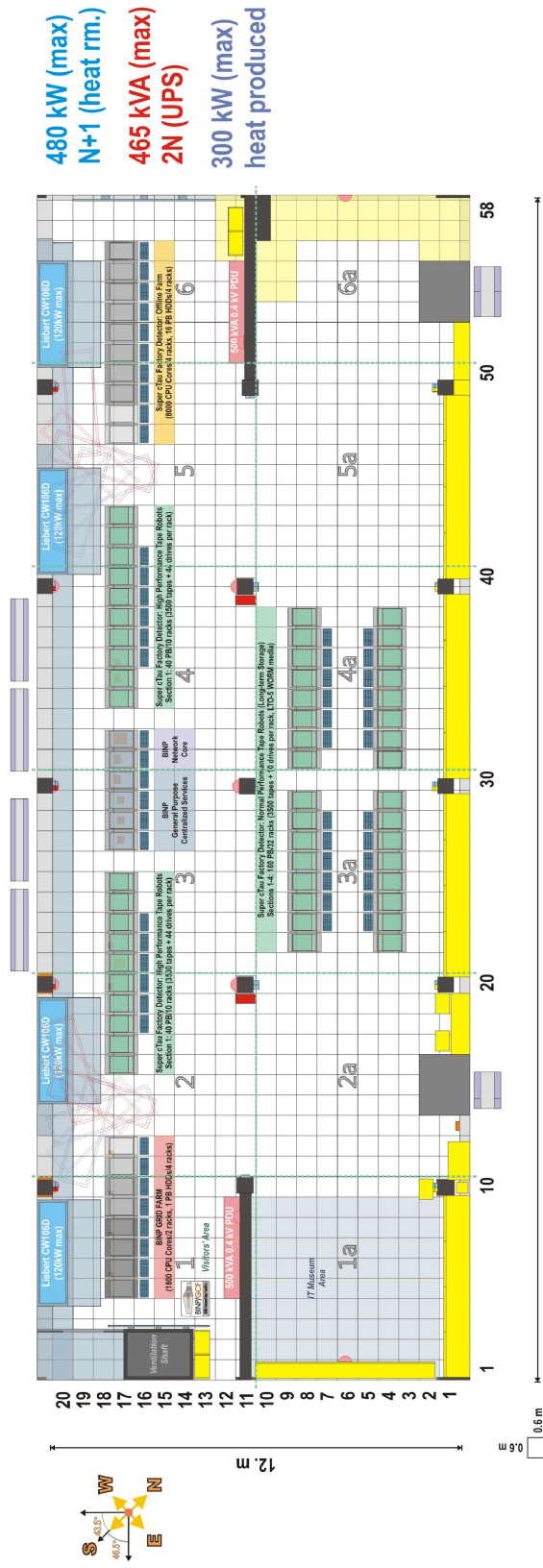
Alexander S. Zaytsev <A.S.Zaytsev@inp.nsk.su>

False Floor Plate Counters
 Full size plates (0.36m²): 973
 Half size plates (0.18m²): 65
 1/4 size plates (0.10m²): 24
 1/8 size plates (0.06m²): 37

- Legacy Free Standing Servers
- Legacy Open Frame Rack
- Legacy Compartment
- APC Open Frame Rack (43U)
- HP ESL-E Tape Library (42U)
- Floor Plates To Be Replaced

Area Estimates

Total usable area: 366.2m² (of 440m² within the outline)
 Legacy hardware zone area: 85.4m² (23%)



- Solid Wall
- Edge False Floor Plate
- Complete False Floor Plate
- Uncovered Solid Floor Sector
- Incomplete False Floor Plate
- Wall Mounted Temperature and Humidity Sensors (Series 1, 2 & 3)
- Fire Fighting Device (CO₂)
- Free Standing UPS/UPS Battery
- Power Distribution Compartment
- Free Standing Network Printer
- Camera
- Ramp
- Doors
- Window
- Parking Zones
- Table
- Open Frame Storage Compartment
- Custom Storage Compartments
- Closed Storage Compartment
- Legacy Hardware Recuperation Area
- Legacy Water Cooled Air Conditioner (7kW)
- Legacy Water Cooled Air Conditioner (7kW, Spare)
- Downflow Water Cooled Air Conditioner
- False Floor Integrated Air Distribution Outlets
- Water Cooling and Recycling Areas

Figure 2.43. Possible layout of the [DataCenter2] facility, assuming the major upgrade of its engineering infrastructure and deployment of all the equipment related to the detector.

Table 2.8. List of basic specifications for the **[DataCenter1,2]** computing facilities.

Feature	[DataCenter1]	[DataCenter2]
Total area (IT area), m ²	300 (160)	360 (220)
False floor load carrying capacity, ton/m ²	≤ 2	≤ 2
Number of racks (total rackmount capacity, 1U)	32 (1344)	76 (2432)
Maximum heat dissipation within a single rack, kW	20	12
Maximum heat dissipation within the IT area, kW	600	300
Maximum cooling capacity of the internal cooling circuit of the data center, kW (redundancy schema implemented)	800 (N+1)	480 (N+1)
Maximum cooling capacity of the external cooling circuit of the data center, kW (redundancy schema implemented)	1500 (N+1)	600 (N+1)
Time of running on the chilled water stored in the redundant water tanks of the internal cooling circuit of the data center, min	15	Unavailable
Maximum electrical power supported by the external power lines, kVA (redundancy scheme implemented)	1500 (2N)	500 (2N)
Maximum load supported by the centralized UPS system, kVA (redundancy scheme implemented)	1200 (2N)	465 (2N)
Centralized UPS capacity for 100% / 50% / 10% of nominal power consumption by the IT equipment, min	20 / 40 / 150	
Data center external connectivity, Gbps (redundancy scheme implemented for the external uplinks)	Unavailable	40 (2(2N))
Capacity of the internal communication lines between the [DataCenter1,2] facilities, Gbps (redundancy scheme implemented for the internal links)	960 (2N)	
Monitoring and maintenance services by the local personnel	365 × 24 × 7	

2.11.4.4 The software and the execution environment

The standard execution environment designed to support all types of software related to events reconstruction, detector simulation, monitoring and control of the detector subsystems and other tasks is proposed to be virtualized, in order to gain the following advantages provided by the hardware virtualization technology:

1. high reliability and rapid recovery of the virtualized services,
2. low level isolation of different types of services from each other,
3. reproducibility with freezing of the configuration execution environment over periods of time such as the entire lifetime of detector experiment,
4. natural way of supporting heterogeneous computing systems, including cloud computing enabled environments.

Scientific Linux [95] or CentOS [109] are proposed as a standard OS for the detector experiment, while XEN [96] or KVM [97] (both are non-commercial products) would be the most preferable choice for the standard virtualization platform to be deployed over the offline farm computing resources.

To ensure collaborative teamwork when developing the detector software, it is planned to use a version control system, with the support of automatic testing systems and error tracking systems.

Gaudi [110] or frameworks based on Gaudi or similar products are planned to be used as the framework for developing software for reconstruction and simulation of experimental detector events, as well as for software high-level (software) trigger (HLT).

The full detector simulation will be implemented on the basis of the GEANT4 [111] package with the framework used for data reconstruction.

Since the remote centers can be a part of the computing infrastructure of SCTF, special attention will be paid to the issue of the global integration of the information and computing resources into a single system for the effective storage and processing of the experimental data and the organization of simulation experiments. It is supposed to use the approaches and solutions developed within the framework of the LHC experiments, in particular, the information system ATLAS Grid Information System (AGIS) [113, 114], used by the ATLAS collaboration. This information system provides:

- description of the computer infrastructure, computing power and storage resources;
- description of the computer model of the experiment, topology and communication between the various components of the software of the data processing system;
- the integration of the configuration parameters and settings of high-level services and distributed network services;
- a single program interface for applications and services of the distributed processing system;
- a single information portal for management, with verification of information integrity, validation of user input, tracking of the history of data changes, etc.

Following the successful operation of AGIS, a more universal CRIC system is currently being developed — Computer resources information catalog [115, 116]. This system can be used as a base platform for building the information component of a distributed computing system for experiments at SCTF. It is planned to use other elements of the computer infrastructure of distributed computing of the ATLAS experiment, such as the central data management system (DDM, ATLAS Distributed Data Management), the system for distributed analysis and task execution (PanDA, ATLAS Production and Distributed Analysis workload management system), services for monitoring, access control and accounting of consumed resources, services for support of different versions of data processing software and others.

2.11.5 Roadmap for Building the Offline Computing and Storage Systems

2.11.5.1 Hardware Commissioning Plan

As it was mentioned earlier in Section 2.11.3, the maximum trigger rate of the first level trigger (LLT) of the detector is equal to 0.5 MHz, while the average experimental event size is estimated to be around 30 kB. Thus the maximum output data rate of the detector TDAQ system is estimated to be 15 GBps = 120 Gbps (which is equivalent of 1.24 PB/day = 470 PB/year), so the maximum amount of data which could be generated by the TDAQ system over the 5 years of constant operation (assuming 100% efficiency) is equal to 2.4 EB. The TDAQ and offline data processing systems of the detector are designed in such a way that the whole flux of data generated by the LLT could be saved on the storage systems of the offline farm for the long-term analysis. However, such a large input data stream is expected only when operating at the J/ψ energy. The average data flow is an order of magnitude smaller; the total amount of input data corresponding to the physical program of the experiments is estimated at 150 PB.

If the period of running at maximum luminosity with the CTF experiment is going to be 2024–2029, then the optimal period for hardware deployment for the offline farm is to be 2021–2023, and for the HDD and 2024–2027 for the tape based storage systems (as the data are accumulated). Therefore the detailed specifications for the hardware components needed for implementing the networking and computing system of the detector is to be prepared first in 2020 and then reevaluated in 2023.

To make the cost estimate, let us make the following assumptions for the time period of 2021–2027.

1. The optimal ratio of the total computing powers aggregated within the HLT trigger farm to the capacity of the HDD based storage system (the high performance and high capacity HDD based storage systems combined) available within the online and offline data processing farms is equal to 25 TFlops/PB and fixed over the whole period.
2. The ratio of the capacities of the high performance tape storage system to the capacity of all the HDD based storage systems within the detector TDAQ and offline data processing farm is equal to 4.0 and fixed.
3. The ratio of the cost per unit of storage system capacity for high performance tape storage system to the cost per unit of HDD based storage systems is equal to 0.45 and fixed.

The following stages of the deployment and operation of the computing infrastructure over the lifetime of the detector experiment are expected (table 2.9):

Table 2.9. The expected computing infrastructure at different stages.

Time period	before 2021	2021–2023	2024–2027
Computing power, Tflops	20	344	600
Disk capacity, PB	1	13	20
Tape capacity, PB	0.1	12	80
External connectivity, Gbit/s	1	10	10–40
Local connectivity, Gbit/s	10	10–20	10–40

1. prototyping, testing and approval of the concepts implied by the design of the system plus engineering infrastructure deployment for the IT centers involved (2017–2021),
2. main deployment period of the IT and networking equipment (2021–2023),
3. production and scheduled maintenance period, devoted mainly to the experimental data taking, processing and archiving for future analysis (2024–2032).

The total cost of the computing system and its engineering infrastructure consisting of

- computing nodes with 0.6 PFlops of combined performance (to be deployed in 2019–2024),
- the high performance HDD based storage system for the offline data processing farm and TDAQ with a total capacity of 20 PB (to be deployed in 2019–2024 as well),
- the high performance tape storage with a total capacity of 80 PB (to be deployed in 2021–2027),

is estimated to be approximately 50 MEuro and its combined power consumption in the final configuration to be about 1 MW.

Once the high performance tape storage system is filled up to 70–80% of its capacity, the deployment of the second stage of the high capacity tape storage system will be done, which will increase the tape storage capacity available for the experiment by 160 PB. The cost estimation for the second stage is not included in the above amount.

The proposed configuration will make it possible to store and analyse approximately $3 \cdot 10^{12}$ experimental events over the 5 years and to handle for the prolonged periods of time the maximum data rate allowed by TDAQ.

2.11.5.2 Building the Prototypes for the Key Components of Data Processing and Storage Systems

Validation of the solutions proposed above for various components of the networking and computing infrastructure of the detector experiment is to be done via building and testing the prototypes for each and every critical part of the infrastructure.

A list of the components which can be evaluated by building the prototypes is given below.

1. The HDD/SSD-based high performance storage systems:
 - (a) fault-tolerant data storage systems based on redundant groups of RAID arrays,

- (b) distributed and parallel file systems (Lustre [98], PVFS2 [99], Hadoop [100], CEPH [107] etc.),
 - (c) multilevel I/O buffers for the storage system head nodes based on high performance SSD devices [81], [82].
2. The robotic tape libraries and tape media: studying the existing solutions for scalable modular robotic tape libraries [83]–[84].
 3. The high performance computing modules based on general purpose CPUs [76]–[78].
 4. The hybrid computing architectures making use of GPU/FPGA based solutions [70]–[75], [79], [80]:
 - (a) finding ways to maximize the performance of EB and HLT subsystems (TDAQ),
 - (b) studying the feasibility of increasing the performance of event reconstruction/simulation jobs running on the offline data processing farm.
 5. The advanced networks:
 - (a) 40/100 Gigabit Ethernet and IPoIB technologies,
 - (b) Fiber Channel and FCoE technologies,
 - (c) DWDM technology.
 6. The radiation resistant optical fiber communication lines (Chapter 2.11.4.2).
 7. The environmental control systems for industrial and IT applications and the industrial process control systems:
 - (a) groups of compact localized sensors similar to the solutions in [102],
 - (b) distributed optical fiber based sensor systems with the readout performed from one of the endpoints, similar to the ones described in [103],
 - (c) hybrid optical fiber based sensor systems supporting both distributed and localized information gathering along the path of the fiber, similar to those described in [104], [105].

Bibliography

- [1] W. Lepeltier, “Review on TPC’s,” J. Phys.: Conf. Ser. 65 012001 (2007).
- [2] W. Erni, I. Keshelashvili, B. Krusche *et al.*, “Physics Performance Report for PANDA,” <http://arxiv.org/abs/0903.3905v1> (2009).
- [3] F. Sauli, Nucl. Instr. and Meth. A **386**, 531 (1997).
- [4] M. Dixit *et al.*, “Micromegas TPC studies at high magnetic fields using the charge dispersion signal,” Nucl. Instr. and Meth., A **581**, 254 (2007).
- [5] Klaus Dehmelt for LP TPC Collaboration, “A large prototype of a time projection chamber for a linear collider detector,” Nucl. Instr. and Meth. A, in press, 2010.
- [6] B. Aubert *et al.* [BaBar Collaboration], Nucl. Instr. and Meth. A **479**, 1 (2002).
- [7] C.O. Vuosalo, A.V. Telnov, K.T. Flood, BaBar Analysis Document #1853, 2010.
- [8] A. Abashian *et al.*, Nucl. Instr. and Meth. A **491**, 69 (2002).
- [9] N. Akopov *et al.*, Nucl. Instr. and Meth. A **479**, 511 (2002) [arXiv:physics/0104033].
- [10] [LHC-b Collaboration], CERN-LHCC-2000-037, LHCb TDR 3, 7 September 2000.
- [11] M. Buenerd [AMS RICH Collaboration], Nucl. Instr. and Meth. A **502**, 158 (2003) [arXiv:astro-ph/0211645].
- [12] T. Iijima *et al.*, Nucl. Instr. and Meth. A **548**, 383 (2005),
S. Korpar *et al.*, Nucl. Instr. and Meth. A **553**, 64 (2005),
P. Krizan, S. Korpar, T. Iijima, Nucl. Instr. and Meth. A **565**, 457 (2006).
- [13] A.Yu. Barnyakov *et al.*, “Focusing aerogel RICH (FARICH),” Nucl. Instr. and Meth. A **553**, 70 (2005).
- [14] A.Yu. Barnyakov *et al.*, Nucl. Instr. and Meth. A **595**, 100 (2008).
- [15] M. Ablikim *et al.*, Nucl. Instrum. Meth. A **614** (2010) 345–399.
- [16] C.O. Vuosalo, A.V. Telnov, K.T. Flood, BABAR Analysis Document #1853, 2010.
- [17] A. Abashian *et al.*, Nucl. Instrum. Meth. A **491** (2002) 69.
- [18] N. Akopov *et al.*, Nucl. Instrum. Meth. A **479** (2002) 511 [arXiv:physics/0104033].
- [19] [LHC-B Collaboration], CERN-LHCC-2000-037, LHCb TDR 3, 7 September 2000.

- [20] M. Buenerd [AMS RICH Collaboration], Nucl. Instrum. Meth. A **502** (2003) 158 [arXiv:astro-ph/0211645].
- [21] S. Nishida *et al.*, Nucl. Instr. and Meth. A **766** (2014) 28–31
- [22] T. Iijima *et al.*, Nucl. Instrum. Meth. A **548** (2005) 383-390,
S. Korpar *et al.*, Nucl. Instrum. Meth. A **553** (2005) 64-69,
P. Krizan, S. Korpar, T. Iijima, Nucl. Instrum. Meth. A **565** (2006) 457-462.
- [23] A.Yu. Barnyakov *et al.*, Nucl. Instrum. Meth. A **553** (2005) 70-75.
- [24] A.Yu. Barnyakov *et al.*, Nucl. Instrum. Meth. A **595** (2008) 100-103.
- [25] G. Bondarenko *et al.*, Nucl. Instrum. Meth. A **442** (2000) 187.
Z. Sadygov *et al.*, Nucl. Instr. and Meth. A **504** (2003) 301.
- [26] T.Frach *et al.*, 2009 IEEE Nuclear Science Symposium Conference Record, **N28-5**
- [27] M. Parenzoni *et al.*, Sensors 2016, 16, 745 (2016), doi:10.3390/s16050745, www.mdpi.com/journal/sensors
- [28] S. Mandai *et al.*, ESSCIRC (ESSCIRC), 2012 Proceedings of the, 2012, pp. 89–92.
- [29] DATASHEET, https://www.hamamatsu.com/resources/pdf/ssd/s13361-3050_series_kapd1054e.pdf
- [30] A. Ferri *et al.*, Nucl. Instr. and Meth. A **824** (2016) 196-197.
- [31] DATASHEET, <http://sensl.com/downloads/ds/DS-MicroCseries.pdf>
<http://sensl.com/downloads/ds/DS-MicroJseries.pdf>
- [32] A.N. Otte *et al.*, Nucl. Instr. and Meth. A **846** (2017) 106-125
- [33] C. Xu *et al.*, 2013 IEEE Nuclear Science Symposium and Medical Imaging Conference (2013 NSS/MIC), Seoul, 2013, pp. 1-7. doi: 10.1109/NSSMIC.2013.6829585
- [34] D. Durini *et al.*, Nucl. Instr. and Meth. A **835** (2016) 99-109
- [35] M.Yu. Barnyakov *et al.*, Nucl. Instr. and Meth. A **824** (2016) 83-84
- [36] A.Yu. Barnyakov *et al.*, Nucl. Instr. and Meth. A **572** (2007) 404-407
A.Yu. Barnyakov *et al.*, Nucl. Instr. and Meth. A **598** (2009) 160-162
A.Yu. Barnyakov *et al.*, Nucl. Instr. and Meth. A **845** (2017) 588-590
- [37] F. Anghinolfi *et al.*, Nucl. Instrum. Meth. A **533** (2004) 183.
R. Gao *et al.*, 2015 **JINST** **10** C02028.
- [38] <http://omega.in2p3.fr/index.php/products.html>
- [39] P. Fischer *et al.*, IEEE TRANSACTIONS ON NUCLEAR SCIENCE, VOL. 56, NO. 3, JUNE 2009
I. Sacco *et al.*, 2013 **JINST** **8** C12013.
I. Sacco *et al.*, Nucl. Instrum. Meth. A **824** (2016) 233-236

- [40] A. Argentieri *et al.*, Nucl. Instrum. and Meth. A **652** (2011) 516.
- [41] J. Bario *et al.*, 2015 **JINST** **10** P12001.
P.S. Marrocchesi *et al.*, Nucl. Instr. and Meth. A **845** (2017) 447-451
- [42] M.D. Rolo *et al.*, 2013 **JINST** **8** C02050
- [43] T.M. Conneely *et al.*, 2015 **JINST** **10** C05003
- [44] J. Benitez *et al.*, Nucl. Instrum. Meth. A **595** (2008) 104.
- [45] B. Dey *et al.*, Nucl. Instr. and Meth. A **775** (2015) 112-131.
- [46] G.N. Abramov *et al.*, 2014 **JINST** **9** C08022.
G.N. Abramov *et al.*, 2016 **JINST** **11** P03004.
- [47] A.Yu. Barnyakov *et al.*, Nucl. Instr. Meth. A **766** 235 (2014)
- [48] A.Yu. Barnyakov *et al.*, Nucl. Instr. and Meth. A **732** (2013) 352-356.
- [49] A. Abashian *et al.* Nucl. Instr. Meth. A **479** 117 (2002).
- [50] B. Aubert *et al.*, Nucl. Instr. Meth. A **479** 1 (2002).
- [51] H. Ikeda *et al.*, *Nucl. Inst. Meth.* **A 441** (2000) 401.
- [52] D.M. Beylin *et al.*, *Nucl. Inst. Meth.* **A541** (2005) 501.
- [53] T. Abe *et al.*, Belle II technical design report, KEK report 2010-1, Tsukuba, Japan (2010).
- [54] B. Shwartz, *Nucl. Inst. Meth.* **A598** (2009) 220.
- [55] C.L.Melcher and Schweitzer, *IEEE Trans on Nucl. Sci.* **39** (1992) 502,
P.R. Menge *et al.*, *Nucl. Inst. and Meth.* **A579**, 6 (2007),
BrilliantCe Scintillators Performance Summary, Scintillation Products Technical Note, Saint-Gobain Crystals, (2009),
S. Kawamura *et al.*, *Nucl. Inst. and Meth.* **A583**, 356 (2007),
Ren-Yuan Zhu, *J. of Phys.: Conf. Ser.*, **587**, 012055 (2015).
- [56] H. Aihara *et al.*, PoS (PhotoDet2015) (2015) 052;
H. Aihara *et al.*, PoS (ICHEP2016) (2016) 703.
- [57] <http://www.luminnotech.com/>
- [58] CMS Collaboration, *JINST*, **8** (2013) P09009.
- [59] A. Kuzmin, *Nucl. Inst. Meth.* **A623** (2010) 252.
- [60] I. Bedny *et al.*, *Nucl. Inst. Meth.* **A598** (2009) 273.
- [61] A. Boyarintsev, *et al.*, *JINST* **11** (2016) P03013.
- [62] A. Kuzmin, Proceedings of the "Calorimetry for High Energy Frontiers - CHEF 2013", (2013) 83.

- [63] G. Bondarenko, B. Dolgoshein, V. Golovin, A. Ilyin, R. Klanner, E. Popova, Proc. of the 5th Int. Conf. on Advanced Technology and Particle Physics, Nucl. Phys. B — Proc.Suppl. **61** (1998) 3 pp. 347.
G. Bondarenko *et al.*, Nucl. Instr. and Meth. A **442**, 187 (2000).
Z. Sadygov *et al.*, Nucl. Instr. and Meth. A **504**, 301 (2003).
- [64] J. Benitez *et al.*, Nucl. Instr. and Meth. A **595**, 104 (2008).
- [65] A. Abashian *et al.* [Belle Collaboration], Nucl. Instr. and Meth. A **479**, 117 (2002).
- [66] Y. Yusa, Nucl. Instr. and Meth. A **598**, 183 (2009).
- [67] V. Smakhtin *et al.*, Nucl. Instr. and Meth. A **598**, 196 (2009).
- [68] MINIOS collaboration, TDR on scintillator, ch.5, http://www-numi.fnal.gov/minwork/info/tdr/mintdr_5.pdf
- [69] V.M. Aulchenko *et al.*, Nucl. Instr. and Meth. A **265**, 137 (1988).
- [70] NVidia Fermi Architecture: http://www.nvidia.ru/object/fermi_architecture_ru.html
- [71] Xilinx 7th series FPGA Products: <http://www.xilinx.com/technology/roadmap/7-series-fpgas.htm>
- [72] Convey Hybrid Computing Platform:
<http://www.conveycomputer.com/products.html>
- [73] Convey HC-1 Family Products:
http://www.conveycomputer.com/Resources/Convey_HC1_Family.pdf
- [74] Nallatech PCI Express Cards: <http://www.nallatech.com/pci-express-cards.html>
- [75] AMD Fusion Family of APUs: <http://sites.amd.com/us/fusion/APU/Pages/fusion.aspx>
- [76] Intel Product Roadmap: <http://download.intel.com/products/roadmap/roadmap.pdf>
- [77] List of Intel Microprocessors: http://en.wikipedia.org/wiki/List_of_Intel_microprocessors
- [78] List of AMD Microprocessors: http://en.wikipedia.org/wiki/List_of_AMD_microprocessors
- [79] SKIF-4 Supercomputer Platform: <http://skif.pereslavl.ru/psi-info/rcms-skif/index.en.html>
- [80] SKIF-4 Architecture: <http://skif.pereslavl.ru/psi-info/rcms-skif/skif-ppt.rus/2009/2009-04-01-pavt2009.ppt>
- [81] FusionIO ioDRIVE DUO Products: <http://www.fusionio.com/products/iodriveduo/>
- [82] FusionIO ioXTREME Products: <http://www.fusionio.com/products/ioxtreme/>
- [83] HP StorageWorks ESL E-series Products:
<http://h10010.www1.hp.com/wwpc/ru/ru/sm/WF25a/12169-304612-304631-304631-304631-392031.html>

- [84] Fujitsu Scalar 10K Series Modular Tape Libraries:
http://ts.fujitsu.com/products/storage/tape/scalar/scalar_10k.html
https://globalsp.ts.fujitsu.com/dmsp/docs/ds_scalar10k.pdf
- [85] <http://www.optolink.ru/ru/catalog/p5/>
- [86] http://www.optolink.ru/pdf/fiber_ru.pdf
- [87] <http://www.optolink.ru/pdf/RSF.pdf>
- [88] <http://fotonexpress.ru/pdf/st/004-010.pdf>
- [89] <http://fotonexpress.ru/pdf/st/011-019.pdf>
- [90] A. Zaytsev et al., “Building a High Performance Computing Infrastructure for Novosibirsk Scientific Center” (contribution presented at CHEP2010 conference: 18-22/10/2010, Taipei, Taiwan): <http://indico2.twgrid.org/MaKaC/materialDisplay.py?contribId=29&sessionId=110&materialId=slides&confId=3>
- [91] Geant3 Network (GN3): <http://www.geant.net>
- [92] WLCG Project: <http://cern.ch/lcg>
- [93] LHC Open Network Environment (LHCONE L3VPN),
<https://twiki.cern.ch/twiki/bin/view/LHCONE/LhcOneVRF>
- [94] Amazon Elastic Compute Cloud (EC2): <http://amazon.com/ec2/>
- [95] <https://www.scientificlinux.org>
- [96] <http://www.xen.org>
- [97] <http://www.linux-kvm.org>
- [98] <http://www.lustre.org>
- [99] <http://www.pvfs.org>
- [100] <http://hadoop.apache.org>
- [101] gLite Middleware: <http://cern.ch/glite>
- [102] APC NetBotz Sensors: <http://www.apc.com/products/family/index.cfm?id=400>
- [103] “Optical Fibre based Distributed Sensor for Temperature Measurement”
<http://www.igcar.ernet.in/benchmark/Tech/19-tech.pdf>
- [104] F. Rodríguez-Barrios et al., “Distributed Brillouin Fiber Sensor Assisted by First-Order Raman Amplification”:
http://infoscience.epfl.ch/record/150155/files/JLT_28_2162_2010_1st
- [105] L. Zou et al., “Distributed fiber Brillouin strain and temperature sensor with centimeter spatial resolution by coherent probe-pump technique”:
http://net04.isis.umanitoba.ca/activeshm/ReferencePage/Reference/Bao/spie5855_zou_a.pdf

- [106] S. Kolos et al., "Online Remote Monitoring Facilities for the ATLAS Experiment" (contribution presented at CHEP2010 conference: 18-22/10/2010, Taipei, Taiwan): <http://indico2.twgrid.org/MaKaC/materialDisplay.py?contribId=174&sessionId=51&materialId=slides&confId=3>
- [107] <http://ceph.com/>
- [108] <https://cernvm.cern.ch/portal/filesystem>
- [109] <https://www.centos.org/>
- [110] <http://proj-gaudi.web.cern.ch/proj-gaudi/>
- [111] <http://geant4.cern.ch/>
- [112] <http://wlcg-public.web.cern.ch/tier-centres>
- [113] Alexey Anisenkov et al (2015) "AGIS: Evolution of Distributed Computing information system for ATLAS". Proceedings of the CHEP 2015 conference J. Phys.: Conf. Ser. 664 062001, <http://iopscience.iop.org/article/10.1088/1742-6596/664/6/062001>
- [114] Alexey Anisenkov et al (2016) "AGIS: Integration of new technologies used in ATLAS Distributed Computing". Proceedings of the CHEP 2016 conference J. Phys.: Conf. Ser. (being published).
- [115] Maria Alandes, Julia Andreeva, Alexey Anisenkov et al (2016) "Consolidating WLCG topology and configuration in the Computing Resource Information Catalogue". Proceedings of the CHEP 2016 conference J. Phys.: Conf. Ser. (being published). <http://information-technology.web.cern.ch/CHEP/consolidating-wlcg-topology-and-configuration-computing-resource-information-catalogue>
- [116] Alessandro Di Girolamo, Alexey Anisenkov et al, "The Computing Resource Information Catalog". HEPiX Spring 2017 Workshop. <https://indico.cern.ch/event/595396/contributions/2532542/>